AFWAL-TR-86-3003
Volume II

ADA170327

ASSESSMENT OF DAMAGE TOLERANCE REQUIREMENTS AND ANALYSES - TASK I REPORT

Volume II - Analytical Methods

A. KUO
D. YASGUR
M. LEVY

Fairchild Industries
Fairchild Republic Company
Farmingdale, N.Y. 11735

MARCH 1986

Final Technical Report for Period September 1982 - June 1984

20050815038

Approved for public release; distribution is unlimited

FLIGHT DYNAMICS LABORATORY
AIR FORCE WRIGHT AERONAUTICAL LABORATORIES
AIR FORCE SYSTEMS COMMAND
WRIGHT-PATTERSON AIR FORCE BASE, OHIO 45433-6553

NOTICE

When Government drawings, specifications, or other data are used for any purpose other than in connection with a definitely related Government procurement operation, the United States Government thereby incurs no responsibility nor any obligation whatsoever; and the fact that the government may have formulated, furnished, or in any way supplied the said drawings, specifications, or other data, is not to be regarded by implication or otherwise as in any manner licensing the holder or any other person or corporation, or conveying any rights or permission to manufacture use, or sell any patented invention that may in any way be related thereto.

This report has been reviewed by the Office of Public Affairs (ASD/PA) and is releasable to the National Technical Information Service (NTIS). At NTIS, it will be available to the general public, including foreign nations.

This technical report has been reviewed and is approved for publication.

Christopher J. Mazur

Lt Christopher J. Mazur, Project Engineer
Fatigue, Fracture & Reliability Group
Structural Integrity Branch

Frank D. Adams

FRANK D. ADAMS, Chief
Structural Integrity Branch
Structures and Dynamics Division

FOR THE COMMANDER

R J Hegstrom

ROGER J. HEGSTROM, Colonel, USAF
Chief, Structures and Dynamics Division

"If your address has changed, if you wish to be removed from our mailing list, or if the addressee is no longer employed by your organization please notify AFWAL/FIBE, *W-PAFB, OH 45433 to help us maintain a current mailing list".*

Copies of this report should not be returned unless return is required by security considerations, contractual obligations, or notice on a specific document.

UNCLASSIFIED
SECURITY CLASSIFICATION OF THIS PAGE

REPORT DOCUMENTATION PAGE

1a. REPORT SECURITY CLASSIFICATION Unclassified	1b. RESTRICTIVE MARKINGS
2a. SECURITY CLASSIFICATION AUTHORITY 2b. DECLASSIFICATION / DOWNGRADING SCHEDULE	3. DISTRIBUTION / AVAILABILITY OF REPORT Approved for public release; distribution is unlimited.
4. PERFORMING ORGANIZATION REPORT NUMBER(S)	5. MONITORING ORGANIZATION REPORT NUMBER(S) AFWAL-TR-86-3003, Vol. II
6a. NAME OF PERFORMING ORGANIZATION Fairchild Industries Fairchild Republic Co. 6b. OFFICE SYMBOL (If applicable)	7a. NAME OF MONITORING ORGANIZATION Air Force Flight Dynamics Laboratory (AFWAL/FIBEC)
6c. ADDRESS (City, State, and ZIP Code) Farmingdale, N.Y. 11735	7b. ADDRESS (City, State, and ZIP Code) Wright-Patterson Air Force Base Ohio, 45433-6553
8a. NAME OF FUNDING / SPONSORING ORGANIZATION AFWAL 8b. OFFICE SYMBOL (If applicable) FIBEC	9. PROCUREMENT INSTRUMENT IDENTIFICATION NUMBER F33615-82-C-3215
8c. ADDRESS (City, State, and ZIP Code) Wright-Patterson Air Force Base Dayton, Ohio 45433	10. SOURCE OF FUNDING NUMBERS PROGRAM ELEMENT NO. 62201F; PROJECT NO. 2401; TASK NO. 01; WORK UNIT ACCESSION NO. 61

11. TITLE (Include Security Classification)
Assessment of Damage Tolerance Requirements and Analyses
Volume II - Analytical Methods

12. PERSONAL AUTHOR(S)
A. Kuo, D. Yasgur and M. Levy

13a. TYPE OF REPORT	13b. TIME COVERED	14. DATE OF REPORT (Year, Month, Day)	15. PAGE COUNT
Final	FROM Sept.82 TO June 84	1986 March 31	147

16. SUPPLEMENTARY NOTATION

17. COSATI CODES			18. SUBJECT TERMS (Continue on reverse if necessary and identify by block number)
FIELD	GROUP	SUB-GROUP	Damage Tolerance, Structural Life Prediction, Fatigue Crack Growth, Fatigue Crack Initiation, Stress Intensity Factor, Stress Concentration Facotr, Stress Severity Factor, Strain Energy Density.
13	13		
13	05		

19. ABSTRACT (Continue on reverse if necessary and identify by block number)

The stress intensity factor and stress severity factor for typical airframe structures have been formulated using the compounded solution method. Two-dimensional and three-dimensional finite element analyses were performed to validate or obtain some of the factors. Two damage tolerance analysis methods have been developed based upon the stress intensity factor and stress severity factor. The first method is based on crack growth only. The second method is based on the combined crack growth and initiation. The strain energy density is proposed as the governing parameter of fatigue crack initiation.

20. DISTRIBUTION / AVAILABILITY OF ABSTRACT ☒ UNCLASSIFIED/UNLIMITED ☐ SAME AS RPT. ☐ DTIC USERS	21. ABSTRACT SECURITY CLASSIFICATION UNCLASSIFIED
22a. NAME OF RESPONSIBLE INDIVIDUAL Lt. Christopher Mazur	22b. TELEPHONE (Include Area Code) (513)225-6104 22c. OFFICE SYMBOL FIBEC

DD FORM 1473, 84 MAR 83 APR edition may be used until exhausted. All other editions are obsolete.

SECURITY CLASSIFICATION OF THIS PAGE
UNCLASSIFIED

FOREWORD

This report is prepared by Fairchild Industries, Fairchild Republic Company for the United States Air Force under a research and development program entitled "Assessment of Damage Tolerance Requirements and Analyses," Contract No. 33615-82-C-3215. This program is being administered by the Air Force Flight Dynamics Laboratory, Air Force Wright Aeronautical Laboratories, Air Force Systems Command, Wright-Patterson Air Force Base, Ohio. Mr James L. Rudd (AFWAL/FIBEC) was the Air Force project engineer through December 1985. Subsequently, Mr Rudd was replaced by Lt Christopher Mazur.

This Final report presents the results of Task I-Volume II, Analytical Methods. The work was performed under the supervision of S. Saul - Senior Section Chief of Stress and W. Guman - Director of Research and Development. A. Kuo was the Program Manager and Principal Investigator through March 1985. Subsequently, Mr Kuo was replaced by Meir Levy for the completion of the program. D. Yasgur contributed to the finite element analyses reported herein. M. Serchia - Word Processing and R. Ingenito - Graphics contributed to the typing and art work for preparing this report.

TABLE OF CONTENTS

Section	Title	Page
1.0	INTRODUCTION	1
1.1	Background of the Program	1
1.2	Objective of the Program	2
1.3	Scope of the Program	2
1.4	Task I	4
2.0	DAMAGE TOLERANCE ANALYSIS METHODS	5
2.1	Crack Growth Method	5
2.2	Combined Crack Initiation and Growth Method	7
2.2.1	Stress/Strain Characterization	7
2.2.2	Material Size Effect	9
2.2.3	Governing Parameter for Crack Initiation	10
2.2.4	Required Basic Data	11
2.2.5	Damage Accumulation	13
2.2.6	Load Interaction Effect	14
2.2.7	Crack Initiation Analysis	16
3.0	STRESS INTENSITY FACTORS	17
3.1	Ancillary Solutions	17
3.1.1	A Through Crack Emanating From A Fastener Hole	18
3.1.2	Two Unequal Through Cracks Emanating From A Fastner Hole	19
3.1.3	Two Symmetric Corner Cracks Emanating From A Fastener Hole	23
3.1.4	A Corner Crack Emanating From A Fastener Hole	25
3.1.5	Two Asymmetric Corner Cracks Emanating From A Fastener Hole	26
3.1.6	A Corner And A Through Crack Emanating From A Fastener Hole	28
3.1.7	A Through Crack Emanating From An Internal Notch	30
3.1.8	A Corner Crack Emanating From An Internal Notch	32
3.1.9	Two Through Cracks Emanating From An Internal Notch	33
3.1.10	Two Corner Cracks Emanating From An Internal Notch	35
3.1.11	A Through And A Corner Crack Emanating From An Internal Notch	36
3.1.12	A Through Crack Emanating From An Edge Notch	37

TABLE OF CONTENTS (CONT'D)

Section	Title	Page
3.1.13	A Corner Crack Emanating From A Plate Edge	40
3.1.14	A Corner Crack Emanating From An Edge Notch	41
3.1.15	The Finite Width Correction	42
3.1.16	A Crack Approaching A Hole	46
3.1.17	The Finite Width Effect For An Edge Crack	48
3.1.18	An Edge Crack In A Semi-infinite Plate	49
3.1.19	The Effect Of A Counter-sink	50
3.1.20	The Stiffening Effect Of A Central Stringer	53
3.1.21	The Stiffening Effect Due To Non-similar Material	54
3.2	Stress Intensity Factors for Typical Airframe Structures	55
3.2.1	Skins of Stringer-reinforced Specimens	55
3.2.2	Tee-Stringer	55
3.2.3	Angle-Stringer	69
3.2.4	Skins and Doublers in Lap-Joints	80
3.3	Fastener Load Distributions in Cracked Lap-Joints	85
3.3.1	General Approach	85
3.3.2	Single-Shear Lap-Joint Specimen	88
3.3.3	Double-Shear Lap-Joint Specimen	100
4.0	STRESS CONCENTRATION FACTORS	110
4.1	The k_{tg} and k_{tb} for Pertinent Configurations	110
4.1.1	A Circular Hole	110
4.1.2	A Circular Hole With A Crack	112
4.1.3	Two Holes Connected By A Slot	114
4.1.4	A Crack Emanating From An Internal Notch	116
4.1.5	An Edge Notch	117
4.1.6	Fastener Tilting and Deflection	117
4.2	The Finite Element Analysis of A Loaded Hole	119
4.2.1	A Single Hole	119
4.2.2	Two Holes Connected By A Slot	124

TABLE OF CONTENTS (CONT'D)

Section	Title	Page
5.0	DAMGRO COMPUTER PROGRAM	125
6.0	CONCLUSIONS	130
	REFERENCES	131

LIST OF FIGURES

Figure	Title	Page
1	Willenborg et al Model	15
2	A Crack Emanating From A Fastener Hole - Remote Stress	18
3	A Crack Emanating From A Fastener Hole - Uniform Pressure	18
4	Two Cracks Emanating From A Fastener Hole - Remote Stress	20
5	Two Cracks Emanating From A Fastener Hole - Uniform Pressure	20
6	Two Symmetric Corner Cracks Emanating From A Fastener Hole - Remote Stress	23
7	Two Symmetric Corner Cracks Emanating From A Fastener Hole - Uniform Pressure	24
8	Illustration of Similarity for Figure 6	24
9	A Corner Crack Emanating From A Fastener Hole - Remote Stress	25
10	A Corner Crack Emanating From A Fastener Hole - Uniform Pressure	25
11	Two Asymmetric Corner Cracks Emanating From A Fastener Hole - Remote Stress	26
12	Illustration of Similarity for Figure 11	26
13	Two Asymmetric Corner Cracks Emanating From A Fastener Hole - Uniform Pressure	27
14	A Corner And A Through Crack Emanating From A Fastener Hole - Remote Stress	28
15	A Corner And A Through Crack Emanating From A Fastener Hole - Uniform Pressurel	29
16	A Through Crack Emanating From An Internal Notch - Notch Stress	30
17	A Through Crack Emanating From An Ellptical Hole - Remote Stress	31
18	A Corner Crack Emanating From An Internal Notch - Remote Stress	32
19	Illustration of Similarity for Figure 18	32
20	Two Through Cracks Emanating From An Internal Notch - Remote Stress	33
21	Two Symmetric Cracks Emanating From An Elliptical Hole - Remote Stress (Ref. 20)	34

LIST OF FIGURES (CONT'D)

Figure	Title	Page
22	Two Corner Cracks Emanating From An Internal Notch - Remote Stress	35
23	Illustration of Similarity for Figure 22	35
24	A Through And A Corner Crack Emanating From An Internal Notch - Remote Stress	36
25	A Through Crack Emanating From An Edge Notch - Remote Stress	37
26	A Through Crack Emanating From An Edge Elliptical Notch - Remote Stress (Ref. 20)	38
27	A Through Crack Emanating From An Edge Notch - Uniform Pressure	39
28	Illustration of Similarity for Figure 27	39
29	A Corner Crack Emanating From A Plate Edge - Remote Stress	40
30a	A Corner Crack Emanating From An Edge Notch - Remote Stress	41
30b	A Corner Crack Emanating From An Edge Notch - Uniform Pressure	41
31a	An Eccentric Crack In A finite Plate - Remote Stress	42
31b	A Crack In A Finite Plate - Uniform Pressure	45
32	A Crack Approaching A hole	46
33	An Edge Crack In A Finite Plate - Remote Stress	48
34	An Edge Crack In A Finite Plate - Fastener Load	48
35a	A Crack In A Semi-infinite Plate - Remote Stress	49
35b	A Crack In A Semi-infinite Plate - Fastener Load	49
36	Comparison Of k_{tg} In A Straight Hole And In A 21% Counter-sunk Hole	51
37	Comparison Of k_{tg} In A Straight Hole And In A 32% Counter-sunk Hole	51
38	A Cracked Sheet With A Central Stringer	53
39	The Stiffening Effect Due To Non-similar Material	54
40	Central Tee-Stringer Continuous Ski Specimen	56

LIST OF FIGURES (CONT'D)

Figure	Title	Page
41	Central Angle-Stringer Continuous Skin Specimen	56
42	Central Tee-Stringer Split Skin Specimen	56
43	Edge-Stringer Continuous Skin Specimen	56
44	Single-shear Lap-joint Specimen	56
45	Double-shear Lap-joint Specimen	56
46	Cracking Sequence and Associated SIF for the Inside Initial Crack in the Skin of Figure 40 - Without Crack Initiation	57
47	Cracking Sequence and Associated SIF for the Inside Initial Crack in the Skin of Figure k40 - with Crack Initiation	57
48	Cracking Sequence and Associated SIF for the Outside Initial Crack in the Skin of Figure 40 - Without Crack Initiation	58
49	Cracking Sequence and Associated SIF for the Outside Initial Crack in the Skin of Figure k40 - With Crack Initiation	58
50	Cracking Sequence and Associated SIF for the Skin of Figure 41 - Without Crack Initiation	59
51	Cracking Sequence and Associated SIF for the Skin of Figure 41 - With Crack Initiation	59
52	Cracking Sequence and Associated SIF for the Inside Initial Crack in the Skin of Figure 42 - Without Crack Initiation	60
53	Cracking Sequence and Associated SIF for the Inside Initial Crack in the Skin of Figure 42 - With Crack Initiation	60
54	Cracking Sequence and Associated SIF for the Outside Initial Crack in the Skin of Figure 42 - Without Crack Initiation	61
55	Cracking Sequence and Associated SIF for the Outside Initial Crack in the Skin of Figure 42 - With Crack Initiation	61
56	Cracking Sequence and Associated SIF for the Inside Initial Crack in the Skin of Figure 43 - Without Crack Initiation	62
57	Cracking Sequence and Associated SIF for the Inside Initial Crack in the Skin of Figure 43 - With Crack Initiation	62
58	Cracking Sequence and Associated SIF for the Outside Initial Crack in the Skin of Figure 43 - Without Crack Initiation	63

LIST OF FIGURES (CONT'D)

Figure	Title	Page
59	Cracking Sequence and Associated SIF for the Outside Initial Crack in the Skin of Figure 43 - With Crack Initiation	63
60	Cracked Tee-Stringers	64
61	Tee-Stringer Models for Compounded Solution Method	64
62	FEM Model for the Tee-Stringer shown in Figure 60-i	66
63	Cracking Sequence and Associated SIF for the Outside Initial Crack in Tee-Stringer - Without Crack Initiation	70
64	Cracking Sequence and Associated SIF for the Outside Initial Crack in Tee-Stringer - With Crack Initiation	71
65	Cracking Sequence and Associated SIF for the Inside Initial Crack in Tee-Stringer - Without Crack Initiation	72
66	Cracking Sequence and Associated SIF for the Inside Initial Crack in Tee-Stringer - With Crack Initiation	73
67	Cracked Angle-Stringer	74
68	Angle-Stringer Models for Compounded Solution Method	75
69	Cracking Sequence and Associated SIF for the Inside Initial Crack in Angle-Stringer - Without Crack Initiation	76
70	Cracking Sequence and Associated SIF for the Inside Initial Crack in Angle-Stringer - With Crack Initiation	77
71	Cracking Sequence and Associated SIF for the Outside Initial Crack in Angle-Stringer - Without Crack Initiation	78
72	Cracking Sequence and Associated SIF for the Outside Initial Crack in Angle-Stringer - With Crack Initiation	79
73	A Model for Skins and Doublers in Lap-joints - No Friction	81
74	A Model for Skins and Doublers in Lap-joints - With Friction	82
75	Cracking Sequence and Associated SIF for Figure 73	83
76	Cracking Sequence and Associated SIF for Figure 74	84

LIST OF FIGURES (CONT'D)

Figure	Title	Page
77	Relation Between Friction and Applied Torque (Ref. 29)	87
78	Effect of Fastener Torque on Faying Surface Frictional Force (Ref. 3, page 197)	87
79	Single-shear Lap-joint Specimen	90
80	Finite Element Model for Single-shear Lap-joint Specimen	91
81	Detail of the Area Surrounding Row 1 Holes	91
82	Model of the Interface Between Hole and Fastener	91
83	Fastener Load Distribution in Row 1 of Single-shear Lap-joint Specimen -- No Friction	95
84	Fastener Load Distribution in Row 1 of Single-shear Lap-joint Specimen -- With Friction	99
85	Double-shear Lap-joint Specimen	101
86	Finite Element Model for Double-shear Lap-joint Specimen	102
87	Detail of the Area Surrounding Row 2 Holes	102
88	Fastener Load Distribution in Row 2 of Double-shear Lap-joint Specimen -- No Friction	106
89	Fastener Load Distribution in Row 2 of Double-shear Lap-joint Specimen -- With Friction	109
90	Hole in Finite Plate - Remote Stress	111
91	Hole in Finite Plate - Fastener Load	111
92	Cracked Fastener Hole in Finite Plate - Remote Stress	112
93	Cracked Fastener Hole in Finite Plate - Fastener Load	113
94	Illustration of Similarity for Figure 93	113
95	Two Holes Connected By A Slot - Remote Stress	114
96	Two Holes Connected By A Slot - Fastener Loads	115

LIST OF FIGURES (CONT'D)

Figure	Title	Page
97	Illustration of Similarity for Figure 96	115
98	Crack Emanating From An Internal Notch - Remote Stress	116
99	Crack Emanating From An Internal Notch - Fastener Loads	116
100	Illustration of Similarity for Figure 99	116
101	Edge Notch - Remote Stress	117
102	Single-shear and Double-shear Lap-joints	118
103	FEM Models For A Loaded Hole, E/D = 32	121
104	FEM Models For A Loaded Hole, E/D = 2	122
105	A Hole Subjected To Uniform Internal Pressure	123
106	Illustration of Superposition For A Loaded Hole	123
107	Two Holes Connected By A Slot - Fastener Load	124
108	Diagram of Subroutine K1010 Analysis	126
109	Diagram of Subroutine K1020 Analysis	126
110	Diagram of Subroutine K1030 Analysis	126
111	Diagram of Subroutine K1040 Analysis	126
112	Diagram of Subroutine K1050 Analysis	127
113	Diagram of Subroutine K2010 Analysis	127
114	Diagram of Subroutine K2020 Analysis	127
115	Diagram of Subroutine K2040 Analysis	127
116	Diagram of Subroutine K2050 Analysis	128
117	Diagram of Subroutine K2060 Analysis	128
118	Diagram of Subroutine S1010 Analysis	128

LIST OF FIGURES (CONT'D)

Figure	Title	Page
119	Diagram of Subroutine S1020 Analysis	128
120	Diagram of Subroutine S1030 Analysis	129
121	Diagram of Subroutine S1040 Analysis	129
122	Diagram of Subroutine S1050 Analysis	129
123	Diagram of Subroutine S1060 Analysis	129

LIST OF TABLES

Table	Title	Page
1	Comparison between Crack Initiation and Crack Growth Methods (Willenborg Model)	16
2	Comparison of CR_{ho1}	19
3	Comparison of CP_{ho1} and CP_{ho2}	21
4	Comparison of CR_{ho2}	22
5	Comparison of CR_{fwa}	43
6	Comparison of CR_{fwb}	44
7	Comparison of CR_{ahk}	47
8	Normalized SIF of Counter-sunk Hole	52
9	Normalized SIF for Tee-Stringer	65
10	Normalized SIF of Angle-Stringer	74
11	Normalized Fastener Load Distribution of Single-shear Lap-joint Specimen -- No Friction	93
12	Normalized Fastener Load Distribution of Single-shear Lap-joint Specimen -- With Friction	97
13	Normalized Fastener Load Distribution of Double-shear Lap-joint Specimen -- No Friction	103
14	Normalized Fastener Load Distribution of Double-shear Lap-joint Specimen -- With Friction	107
15	Comparison of k_{td}	118
16	FEM Results of k_{tb} for a Single Hole	120
17	FEM Results of k_{tb} for Two Holes Connected By A Slot.	124

1.0 INTRODUCTION

1.1 Background of the Program

The recognition that failures of metallic aircraft structures are primarily caused by cracks emanating from fastener holes and the availability of fracture mechanics methodologies to deal with cracks have led the USAF to adopt the damage tolerance approach, in lieu of the safe-life approach, for ensuring safety of aircraft. The requirements specified by the USAF to achieve a damage tolerant design are given in MIL-A-83444 (Ref.1), which defines initial flaw assumptions, in-service inspection flaw assumptions, inspectability, and which specifies residual strength requirements. However, some of the requirements are based on engineering judgment and limited data; hence they need to be updated, improved upon through analyses, and verified experimentally.

Fatigue crack growth life analysis is essential, in the fulfillment of MIL-A-83444, for qualifying the service life of airframes, establishing inspection intervals, and satisfying residual strength requirements. The effectiveness of the damage tolerance approach will greatly depend on the accuracy of fatigue crack growth life analyses. To perform fatigue crack growth life analyses, assumptions must be made of specific initial primary flaw location, flaw geometry, flaw multiplicity, continuing damage, and cracking sequence for a fracture critical area. Although MIL-A-83444 gives such assumptions, it is often not detailed and specific enough so that analyses can be made for typical structural elements without invoking somewhat arbitrary assumptions. Experience has indicated that varying these assumptions often results in substantial differences in fatigue crack growth lives. In particular, the most critical locations for initial primary damage are not obvious for the complex geometries involved in aircraft structures. Thus, guidelines are needed for identifying the most critical initial primary damage locations.

In the design analysis of airframes, the complexities of numerous structural details, assumption of the initial crack locations and flaw geometries, and possible cracking sequence have necessitated the consideration of time and cost required for the analysis. The compounded solution method (Ref. 2) is well suited for the design and has been commonly used in the aircraft industry. However, a thorough assessment of the accuracy of this relatively simple method is needed for complex aircraft structural configurations and loadings.

Current damage tolerance analysis is based on fracture mechanics which presumes the existence of initial flaws. However, it is often observed that the growth of initial primary damage is arrested at an adjacent boundary or fastener hole. In order to continue the analysis of subsequent cracking behavior, current MIL-A-83444 assumes that the initial continuing damage having specified sizes and shapes exists at specified locations. Such assumptions are necessary because fracture mechanics cannot be used to predict the reinitiation time of an arrested crack; in particular, these assumptions often result in very conservative structural life predictions of chordwise lap-joints. One promising method of predicting the reinitiation time involves the use of baseline fatigue crack initiation data and the concept of stress severity factor. A study of this method was made in Ref. 3; however, improvement and verification of such a crack reinitiation analysis is needed to assess the initial continuing damage assumptions in MIL-A-83444 and the associated analyses.

The previously completed USAF contract F33615-75-C-3093 (Refs. 3, 4, and 5) was directed toward resolving the above problems. The effort of that contract has resulted in recommended improvements to MIL-A-83444 and the associated analyses, and has exposed a deficiency in the crack reinitiation analysis. However, the conclusions were based on a single material and constant amplitude load tests. Therefore, such conclusions must be further verified and substantiated by extensive experimental and analytical studies which use realistic aircraft structural configurations, manufacturing processes, and service stress spectra.

1.2 Objective of the Program

The objectives of this reported upon program are germane to the background as described in the previous section. The objectives are to: (a) assess the validity of and recommend improvements to the current USAF MIL-A-83444, (b) develop guidelines for identifying the most critical initial primary damage locations for typical aircraft structure and, (c) assess and improve the state-of-the-art analytical methods to satisfy the requirements of MIL-A-83444.

1.3 Scope of the Program

To ensure that the program objectives are met, eight major tasks are planned. These tasks are divided into three phases as shown below.

Phase 1:

Task I:	Analytical Methods
Task II:	Basic Tests
Task III:	Analytical Predictions

Phase 2:

Task IV:	Structural Tests
Task V:	Analytical/Experimental Correlations

Phase 3:

Task VI:	Assessment of and Recommended Improvements to MIL-A-83444
Task VII:	Guidelines for Selecting the Most Critical Initial Primary Damage Locations
Task VIII:	Assessment of and Improvement to Damage Tolerance Analyses

The objective of Task I is to formulate approximate stress intensity and stress severity factors based on the compounded solution method. Two damage tolerance analysis methods have been developed based on the stress intensity and stress severity factors. The objective of Task II is to generate basic material property data which are necessary to the life prediction of the structural test specimens in Task IV. The objective of Task III is to predict the lives of all structural test specimens in Task IV, using the analytical methods developed in Task I and the basic material property data generated in Task II.

The objective of Task IV is to conduct damage tolerance tests representing the realistic aircraft structural configurations and service usage stress spectra. The tests involve stringer-reinforced panels and chordwise lap-joints. The stress spectra include a constant amplitude loading, a spectrum which represents attack/fighter/trainer aircraft, and a spectrum which represents bomber/cargo/transport. Two materials are used i.e. 2024-T3XX and 7075-T6XX aluminum alloys. The objective of Task V is to correlate the analytical predictions of Task III with the test data of Task IV.

The objective of Task VI is to assess the validity of the current MIL-A-83444 requirements. Improvements to the MIL-A-83444 shall be recommended as appropriate. The objective of Task VII is to develop guidelines for selecting the most critical initial primary damage locations for typical aircraft structures. The objective of Task VIII is to assess the analytical capability for predicting the damage tolerance lives of typical aircraft structural configurations subjected to representative spectrum loadings. The

assessment will be based on the analytical/experimental correlations of Task V. Utilizing the results of Task V and VI, improvements to the current damage tolerance analysis methods will be made as appropriate.

1.4 Task I

To achieve the objective of assessing and improving the state-of-the-art analytical methods to satisfy the requirements of MIL-A-83444, the major effort of Task I was focused on assessment and improvement of the compounded solution method and crack initiation analysis method. This Volume II report contains the results of Task I efforts.

The ancillary solutions required in the compounded solution method have been improved, integrated, and simplified for expedient usage. The stress intensity and stress severity factors have been formulated for typical airframe structures such as stringer-reinforced panels and chordwise lap-joints to be used in Task IV-Structural Tests. Two-dimensional and three-dimensional finite element analyses have been performed to improve and validate stress intensity and stress severity factor solutions. In order to improve the handling of continuing damage, an analytical method based upon the concepts of stress severity factor and strain energy density have been developed to predict crack initiation.

The analytical methods developed in Task I were incorporated into an automated computer program to predict the damage tolerance life of airframe structures. The computer program was written in FORTRAN computer language. The computer program will be used in Task III to predict structural lives of the specimens developed in Task IV. A user's manual for the computer program will be prepared and submitted to the Air Force Wright Aeronautical Laboratories (AFWAL) in a later stage of the program.

2.0 DAMAGE TOLERANCE ANALYSIS METHODS

Damage tolerance analysis involves structural life and residual strength predictions. According to the current MIL-A-83444, structural life prediction shall be made on the basis of crack growth only. The structural life prediction method based on crack growth only has shown satisfactory accuracy for the majority of airframe structures except chordwise lap-joints. The comparison of experimental and analytical results in the previously completed contract (Refs. 3, 4, and 5) have shown that life predictions of chordwise lap-joints are too conservative. It was experimentally observed (Ref. 3) that when the primary damage grows into an adjacent hole, a considerable amount of time is required to initiate a crack in the opposite side of an adjacent hole at which the primary damage terminates. Such observations have necessitated an alternative method for treating continuing damage, for lap-joints in particular. Therefore, a combined crack growth and initiation method for damage tolerance analysis has been developed in this investigation to improve life predictions of lap-joints.

In this contract, a computer program was developed which provides the options for performing damage tolerance analyses either based on crack growth alone or based on the combined crack growth and initiation. The theoretical background of the computer programs are described in the following sections of this report.

2.1 Crack Growth Method

The crack growth method is based entirely on the principles of fracture mechanics which have been well established and need not be reiterated herein. The recently completed USAF contract F33615-77-C-3121 (Ref. 6) has reported the details of the crack growth method. In the crack growth method, the following elements need to be included in the analysis. The way of handling these elements is briefly described.

- stress intensity factors
- da/dN equation
- load interaction effects
- crack growth/initial flaw geometry model
- damage accumulation scheme

Within the framework of fracture mechanics, the stress intensity factor, K, has been used as the primary characterization parameter for crack growth life prediction. Thus, the accuracy of the stress intensity factor solution for the complex airframe structures will

have direct impact on life prediction. Experience indicates that a $\pm 10\%$ variation in the stress intensity factor will result in very substantial variation in the predicted structural life. Therefore, the stress intensity factor solutions must be as accurate as possible within the prevailing constraints. A detailed description of the stress intensity factor solutions is given in Section 3 of this report.

The Walker equation (Ref. 6) as shown in Equation (1) is adopted to fit the experimental da/dN (constant amplitude fatigue crack growth rate) data. The constants, c,m, and n, in Equation (1) are to be determined from experimental data through a curve-fitting procedure. The R and K_{max} in Equation (1) are stress ratio and maximum stress intensity factor,

$$\frac{da}{dN} = c\,[(1-R)^m K_{max}]^n \tag{1}$$

respectively. Two da/dN equations are required; one equation fits the experimental data with positive stress ratios, and the other equation fits the experimental data with negative stress ratios. The da/dN is set to zero for K_{max} being less than $K_{threshold}$ which is the minimum value of the stress intensity factor for a crack to grow under fatigue loading. The effect of stress ratio on da/dN is not considered when the positive stress ratio is higher than a positive cut-off value or when the negative stress ratio is smaller than a negative cut-off value.

The load interaction effects being considered are (i) retardation due to tensile overload, (ii) acceleration due to compressive load in the tension-compression load cycle, and (iii) reduced retardation effect due to a compressive load spike which follows overload. The generalized Willenborg et al-Gallagher-Chang et al model (Ref. 6, 7, 8) is adopted to treat load interaction effects. The mathematical expressions of the model are given in Ref. 6.

Both of the part-through and corner cracks change their shape (aspect ratio) under fatigue loading. The stress intensity factor in the depth-direction is different from that in the surface-direction. Crack growth in both depth- and surface-directions are analyzed individually using the stress intensity factors appropriate to each direction. Such an approach is being identified in Ref. 6 as the two-dimensional crack growth model. The

portion of crack growth life for a crack to grow through the plate thickness will increase with plate thickness. Thus, a two-dimensional model will improve the life prediction of those airframe parts which are made of thick plates or forgings.

The damage accumulation scheme being adopted is the linear approximation method (Ref. 6) which is considered to be a reasonable compromise between prediction accuracy and computational efficiency. A description of the linear approximation method is given in Ref 6.

2.2 Combined Crack Initiation and Growth Method

In the combined crack growth and initiation method for life prediction, the crack growth is analyzed in a way similar to those described in Section 2.1. The only difference is that the simultaneous growth of two unequal-length cracks emanating from the same fastener hole or internal notch is accounted for. The various aspects which need to be considered in the crack initiation analysis is given in the following sections.

2.2.1 Stress/Strain Characterization

Fatigue crack initiation is a rather localized behavior; it is determined mainly by the local concentrated stress/strain. The concept of stress severity factor proposed in Ref. 9 appears to be a suitable parameter for characterizing the elastic stress concentration at a fastener hole subjected to both fastener load and remote (by-pass) load. The stress severity factor is defined in the following equations,

$$k_t = \frac{1}{\sigma_o}\left[\underbrace{\frac{(1-C)\,P}{Wt}\,k_{tg}}_{\text{by-pass load}} + \underbrace{\frac{CP}{2\,Rt}\,k_{tb}\,k_{td}}_{\text{fastener load}}\right] \tag{2}$$

$$k = \alpha\,\beta\,\gamma\,k_t \tag{3}$$

where: k_t = elastic stress concentration factor for a fastener hole

k = stress severity factor

σ_o = P/wt = effective reference stress

α = coefficient to account for hole condition

β = coefficient to account for fastener system

γ = coefficient to account for faying surface condition

P = applied total load

c = fraction of load transferred through fastener

R = hole radius

W = plate width

t = plate thickness

k_{tb} = elastic stress concentration factor for fastener load assuming rigid fastener and no fastener tilting

k_{td} = elastic stress concentration factor to account for fastener tilting and fastener deflection

k_{tg} = elastic stress concentration factor for remote load

Many observations in the past have repeatedly indicated that the local concentration of plastic strain at a notch root causes fatigue crack initiation of notched members. Such observations became the basis for the common practice in fatigue analysis where only stress/strain at the very edge of the notch root was considered. In order to obtain a true stress/strain characterization at the notch root, the well-known Neuber's rule (Ref. 10) is employed in conjunction with the stress severity factor. Neuber's rule can be expressed in the following equation,

$$k_t^2 = k_\sigma k_\epsilon \tag{4}$$

where k_t is the elastic stress concentration factor as defined in Equation (2); the k_σ and k_ϵ are the true stress and strain concentration factors, respectively. The k_σ and k_ϵ are defined as

$$k_\sigma = \frac{\sigma}{\sigma_o} \tag{5}$$

$$k_\epsilon = \frac{\epsilon}{\epsilon_o} \tag{6}$$

where σ and ϵ are the maximum true peak stress and strain at the notch root, respectively; and σ_o and ϵ_o are the average gross section stress and strain, respectively. It is noted that Neuber's rule was originally written on the basis of net section stress/strain. It is assumed in this investigation that Neuber's rule is also applicable for gross section stress/strain.

$$k_t^2 = \frac{\sigma}{\sigma_o} \frac{\epsilon}{\epsilon_o} \tag{7}$$

For the cases where the average gross section strain is within the elastic limit, such as in aircraft structures, Equation (7) can be rewritten as,

$$\frac{(k_t \sigma_o)^2}{E} = \sigma \epsilon \tag{8}$$

Since k_t and E are fixed for a given geometry and material, Equation (8) indicates that the relation between true peak stress and true peak strain corresponding to a given gross section stress is a hyperbolic curve. This outcome of Neuber's rule has been experimentally demonstrated in Ref. 11 using the experimental data of Ref. 12.

The right hand side (R.H.S.) of Equation (8) is the product of true peak stress and strain at the very edge of the notch root. Therefore, the left hand side (L.H.S.) of Equation (8) can be used to characterize the true peak stress/strain at the very edge of the notch root. The L.H.S. of Equation (8) equals two times the strain energy density, S. Hence, S, as defined in Equation (9), is adopted to characterize the true peak stress/strain in this investigation.

$$S = \frac{1}{2}\sigma\epsilon = \frac{1}{2}\frac{(\sigma_o k_t)^2}{E} \tag{9}$$

Brussat et al (Ref. 3) have proposed to use the peak elastic stress, $k_t \sigma_o$, for characterizing the stress/strain at the notch root vicinity. A major undesirability of Brussat et al's approach is that the elastic peak stress often exceeds the ultimate strength of the materials. The strain energy density approach proposed in this investigation will circumvent the disadvantage encountered in the peak elastic stress approach.

2.2.2 Material Size Effect

An important fatigue phenomenon which needs to be considered to achieve accurate crack initiation time is the "material size effect". It is a well established fact that the fatigue notch factor, k_N, is lower than the theoretical elastic stress concentration factor, k_t. This fact implies that the real stress experienced by the material at the notch root is lower than that calculated by the theoretical elastic stress concentration factor. In other words, the high peak elastic notch stress is not realized at the notch root. This "material size effect" was observed even in the cases where peak notch stress was well within the elastic limit so that plastic deformation could not be used as the basis of explanation. The "material size effect" has been ascribed to the fact that engineering metals have a granular structure, whereas the theory of elasticity for metals assumes the material to be a homogeneous and isotropic continuum. Thus, this notch fatigue phenomenon is termed "material size effect" to distinguish it from other size effects such as "metallurgical size effect" and "statistical size effect". The omission of this effect in fatigue crack initiation analysis will result in conservative estimates of structural life. Therefore, it is necessary to consider "material size effect" to achieve realistic structural

life predictions. The recognition of such a necessity is evidenced by the inclusion of the Neuber's "material size effect" correction to k_t in the specification of metal fatigue data as contained in MIL-HDBK-5D.

The elastic stress concentration factor k_t appearing in Equation (9) is subjected to the "material size effect" correction. The common approach to treat "material size effect" is due to Neuber (Ref.13). Neuber recognized the granular structure of metal and argued that when there is a very high stress gradient, the usual assumptions of isotropy and homogeneity are invalid within a localized area. He proposed a block-model in which conventional theory of elasticity for metals is applicable down to region of a limiting size (of linear dimension ρ'). Thus, a material is composed of material "building blocks" instead of crystal grains and a high stress gradient across this material "building block" is not permitted. Based on this argument, Neuber proposed the following "effective stress concentration factor" to account for "material size effect",

$$k_N = 1 + \frac{k_t - 1}{1 + \sqrt{\frac{\rho'}{\rho}}} \tag{10}$$

where ρ is the notch root radius; the ρ' is Neuber's material constant which is available for aluminum and steel from Refs. 14 and 15, respectively.

According to Equation (10), k_N is always smaller than k_t; and for the same k_t, k_N decreases with decreasing ρ . Such a relationship conforms with the empirical observation that the smaller the notch root radius, the more the experimental fatigue notch factor falls below the theoretical elastic stress concentration factor.

2.2.3 Governing Parameter for Crack Initiation

Based upon Equations (2), (9), and (10), the strain energy density, S, is redefined (Cf. Equation (9)) in Equation (11) as the governing parameter for crack initiation.

$$S = \frac{1}{2} \frac{(k\,\sigma_o)^2}{E} \tag{11}$$

where

$$\mathbf{k = stress\ severity\ factor} = \alpha\,\beta\,\gamma\,k_N \tag{12}$$

The procedure for computing the governing parameter, S, of fatigue crack initiation at notch root is given below:

Step 1: Calculate effective reference stress, σ_0 , taking into account all friction forces.

Step 2: Calculate k_t due to hole geometry, fastener load, and remote load.

Step 3: Calculate k_N according to Equation (10).

Step 4: Calculate stress severity factor, k, according to Equation (12). The empirical constants, α , β , γ are determined from basic test which will be described in the next section.

Step 5: Calculate strain energy density, S, according to Equation (11).

2.2.4 Required Basic Data

Experimental tests are required to provide basic fatigue crack initiation data for the analysis. The coupon test specimens should be representative of the geometries encountered with typical aircraft structures such as a plate containing a circular hole and a plate containing two holes which are connected by a slot. The specimen geometry should be simple enough to permit accurate stress analysis and precise control of excitation parameters used in testing, yet it should yield the kind of data suitable to the determination of coefficients, α , β , and γ in Equation (12). The stress levels used in the testing will be representative of the stress spectrum under consideration. Parameters considered in the tests are fastener/hole interference or clearance, clamp-up, load transfer, and sealant.

The test crack initiation life, N, will be plotted against strain energy density, S, using a log-log scale. The data can be represented by a best-fit equation in the following form,

$$S_{max} = S_f N^m \tag{13}$$

where S_{max} is the maximum strain energy density and S_f can be interpreted as material constant corresponding to N = 1.

In order to determine α , β , and γ , results from specimens with interference, clamp-up, and sealant, respectively will be plotted to obtain three lines. These three lines are expected to be approximately parallel to the basic line obtained from specimens without interference, clamp-up, or sealant. The α , β , and γ will be determined so as to bring the three lines into coincidence with the basic line.

The basic test is to be conducted for only one strain energy density ratio, i.e., R = S_{min}/S_{max}= 0.0. The advantage of using R = 0.0 is to be explained later. It should be

noted that the strain energy density ratio equals the square of the stress ratio according to the definition of strain energy density (Equation 11). The basic crack initiation data for R = 0.0 is sufficient for the analysis, because crack initiation life for other strain energy density ratios in a stress spectrum can be estimated in a manner similar to the well-known Goodman Diagram which is widely used in MIL-HDBK-5D to present constant amplitude S/N fatigue data. A linear approximation is adopted to construct a constant life diagram (Goodman Diagram) as shown in Equation (14).

$$S_a = A\left(1 - \frac{S_m}{S_f}\right) \tag{14}$$

S_a and S_m are strain energy density amplitude and mean strain energy density, respectively, and the constant A in Equation (14) can be determined from Equation (13) which is valid only for R = 0.0. After some mathematical manipulation of Equations (13) and (14), the equation for constant life curves is given as.

$$S_a = \frac{\left(\frac{1-R}{2}\right) S_f N^m}{1 - \left(\frac{1+R}{2}\right) N^m} \left(1 - \frac{S_m}{S_f}\right) \tag{15}$$

It should be noted that the R in Equation (15) is not an independent variable, but is the strain energy density ratio used in the basic test. In the fatigue crack initiation analysis, S_a and S_m are known for a given stress cycle. The unknown is the life, N. Solving Equation (15) for N in terms of S_a and S_m results in the following expression.

$$N^m = \frac{S_a}{\left(\frac{1+R}{2}\right) S_a - \left(\frac{1-R}{2}\right) S_m + \left(\frac{1-R}{2}\right) S_f} \tag{16}$$

When R = 0.0, Equation (16) can be greatly simplified as follows.

$$N^m = \frac{2 S_a}{S_a - S_m + S_f} \tag{17}$$

$$N = \left[\frac{(1-R) S_{max}}{S_f - R S_{max}}\right]^{\frac{1}{m}} \tag{18}$$

Obviously, Equation (17) is much simpler than Equation (16). It should also be noted that Equation (18) is as simple as any da/dN equation. Thus, computation time can be greatly reduced the selection of R = 0.0 for basic test. The simple expression of Equation (18) will be used to deal with the positive stress ratios. For the negative stress ratios, the stress ratios are set to zero.

2.2.5 Damage Accumulation

Equation (18) gives the crack initiation life as a function of constant strain energy density. However, the strain energy density is a variable for a component subjected to a stress spectrum, because it is determined by the stress severity factor, which changes with crack length and effective reference stress, σ_0. Thus, to predict fatigue crack initiation under spectrum loading, cumulative damage computations must be performed. The Palmgren-Miner approach of linear cumulative damage is being employed.

The damage rate, dD/dN = 1/N, can be obtained from Equation (18) which is derived from basic test data. According to the Palmgren-Miner approach, the cumulative damage is,

$$\int_0^{n_L} \left(\frac{dD}{dn}\right) dn = \sum_{i=1}^{L} \frac{\Delta n_i}{N_i} = D_f \tag{19}$$

When cumulative damage equals a predetermined value of D_f, a fracture mechanics crack is assumed to be initiated. A 0.05 inch corner circular flaw is considered as an initial fracture mechanics crack. The back-tracking method will be used to determine D_f for each of the two stress spectra selected for the structural tests of Task IV. Let t_i be the crack initiation life determined from the backtracking method and T^i be the total life for a specimen subjected to stress σ_i. Then, compute $d_i = t_i/T_i$. It should be noted that total fatigue life consists of crack initiation life and crack growth life; the lower the stress level is, the longer the crack initiation life will be. Thus, the value of d_i will increase with decreasing stress level. Since the set of stress levels $\sigma_1, \sigma_2, \ldots \sigma_n$ to be used in the basic test were intentionally selected to be representative of the kind of stress

layers in a spectrum, a weight factor, W_i, will be assigned to each σ_i according to the number of occurrences of σ_i in a specific spectrum. The W_i will be selected in a manner such that,

$$\sum_{i=1}^{L} W_i = 1 \tag{20}$$

The value of D_f will be determined by the following formula,

$$D_f = \sum_{i=1}^{L} W_i d_i \tag{21}$$

Thus, D_f will not be a universally fixed value since it depends on the stress spectrum and fatigue crack initiation properties of materials.

2.2.6 Load Interaction Effect

Load interaction will affect not only crack growth life but also crack initiation life. Thus, it needs to be considered in the analysis to achieve a realistic prediction of crack initiation time. There have been a number of theoretical models to treat load interaction effects in crack growth analysis, but no such models exist for crack initiation. The Willenborg model, which represents one of the state-of-the-art retardation models in crack growth analysis, was employed in Ref. 3 to treat the beneficial effect due to overload in the crack initiation analysis. The Willenborg model will also be employed in this investigation.

The Willenborg model utilizes the concept of effective stress at the crack tip. The two essential elements in the Willenborg model are: (i) what is the effective stress? and (ii) when will retardation effect cease? Figure 1 illustrates the Willenborg model. The effective stresses are given as

$$\begin{aligned} \text{effective } \sigma_{max} &= \sigma_{max} - (\sigma' - \sigma_{max}) = 2\sigma_{max} - \sigma' \\ \text{effective } \sigma_{min} &= \sigma_{min} - (\sigma' - \sigma_{max}) = (\sigma_{max} + \sigma_{min}) - \sigma' \end{aligned} \tag{22}$$

where σ' is the stress level required to effect a plastic zone r_p such that $a + r_p = a_p$. Retardation effect will cease when the current stress level results in a plastic zone r_p such that $a + r_p \geq a_p$.

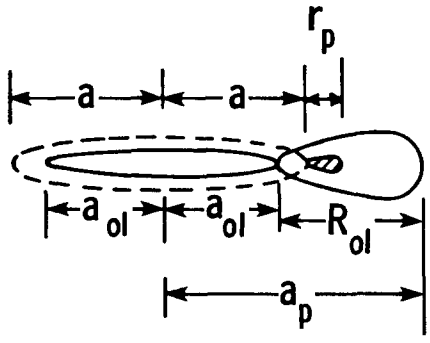

Figure 1. Willenborg Model

In applying the Willenborg model to fatigue crack initiation, let D_{ol} be the damage due to overload stress σ_{ol}. The D_{ol} can be calculated as $D_{ol} = 1/N_{ol}$, where N_{ol} is obtained from Equation (18). Let $d_i = 1/n_i$ be the damage induced by the stress σ_i after overload, where n_i can be calculated from Equation (18) if the effective stress is known. Then, calculate the cumulative damage up to the current stress cycle, Σd_i. If Σd_i is greater than or equal to D_{ol}, then the overload effect ceases. To calculate σ', the difference in damage $D_i - \Sigma d_i$ is first calculated, then calculate the number of cycles corresponding to $D_{ol} - \Sigma d_i$ as $n' = 1/(D_{ol} - \Sigma d_i)$, finally, the stress level corresponding to n' is calculated from Equation (18). The effective stress to be used for calculating d_i subsequent to overload can be calculated in the same way as shown in Equation (22).

The above approach is suggested in order to keep as parallel a relationship as possible to its counterparts in crack growth analysis, but differences do exist. Table 1 shows the one-to-one comparison of the Willenborg model applied to crack growth and crack initiation, respectively.

TABLE I. COMPARISON OF WILLENBORG MODEL
COMPARISON BETWEEN CRACK INITIATION AND CRACK GROWTH
METHODS (WILLENBORG MODEL)

	Crack Growth	Crack Initiation
Damage Index At Overload	$a_p = a_{ol} + R_{oL}$	D_{oL}
Overload Effect Ceases	$a + r_p \geq a_p$	$\Sigma d_i \geq D_{oL}$
σ'	The stress that results in r_p such that $a + r_p = a_p$	The stress that results in n' such that $(1/n' + \Sigma d_i) = D_{oL}$
Effective Stresses	$\sigma_{max} = 2\sigma_{max} - \sigma'$ $\sigma_{min} = (\sigma_{max} + \sigma_{min}) - \sigma'$	$\sigma_{max} = 2\sigma_{max} - \sigma'$ $\sigma_{min} = (\sigma_{max} + \sigma_{min}) - \sigma'$

2.2.7 Crack Initiation Analysis

The approach employed to perform crack initiation analysis is summarized as following:

- Use the strain energy density, $S = 0.5\ (k\sigma_o)^2/E$, as the governing parameter in crack initiation analysis.
- Positive and negative stress ratios in a flight-by-flight spectrum are treated with the Goodman Diagram and the basic fatigue crack initiation data.
- The Palmgren - Miner rule is used for damage accumulation computation. The damage index, D_f, is determined using the weight factor method.
- The Willenborg model is used to treat the load interaction effect.

3.0 STRESS INTENSITY FACTORS

An analytically closed form solution of the stress intensity factor for an actual airframe part is presently too difficult to achieve within practical considerations. The common approach currently being used by the aircraft industry is the compounded solution method (Ref. 2) wherein the stress intensity factor is obtained by superimposing a set of appropriate ancillary solutions to account for the effects of various structural boundaries. Ancillary solutions are usually associated with simple configurations. The method can be expressed in the following equations:

$$K = K^R \cdot CR_1 \cdot CR_2 \cdots\cdots CR_n \tag{23a}$$

$$K^R \equiv \sigma \sqrt{\pi a} \tag{23b}$$

where σ and "a" are the remote stress and crack length, respectively. The CR_1, CR_2, $\cdots CR_n$ are the correction factors associated with the ancillary solutions. The ancillary solutions are to be discussed in Section 3.1. According to Equations (23a) and (23b), the accuracy of the stress intensity factor obtained with the compounded solution method will depend on the type and accuracy of the ancillary solutions being used for modeling. Where a high degree of accuracy is required, the finite element method (FEM) is usually used.

The compounded solution method is used in this program to formulate stress intensity factors for complex airframe structures. However, the deficiencies of the compounded solution method were improved, whenever appropriate, using the finite element method.

3.1 Ancillary Solutions

To apply the compounded solution method, the load and geometry of a fracture critical area in an airframe are decomposed into simple geometries subjected to remote uniform stress and/or fastener load. The stress intensity factor solution for the simple geometry is called an ancillary solution. Two kinds of ancillary solutions are given for each configuration. One is due to remote uniform stress as shown in Equations (23a) and (23b), the other is due to uniform internal pressure, as shown in Equations (23c) and (23d), which are intended to simulate fastener loads.

$$K = K^P \cdot CP_1 \cdot CP_2 \cdots\cdots CP_n \tag{23c}$$

$$K^P \equiv p \sqrt{\pi a} \tag{23d}$$

"p" and "a" are the uniform pressure on an entire hole and the crack length respectively. The CP_1, CP_2,.....CP_n are the correction factors associated with the ancillary solutions. Note that the definition of Equation (23c) is different from the conventional one. The definition was used in Tweed and Rooke's (Ref. 18) ancillary solution for a pressurized hole.

3.1.1 A Through Crack Emanating From A Fastener Hole

The stress intensity factor, SIF, of a through-crack emanating from a circular hole (Figure 2) was firstly solved by Bowie (Ref. 16). Bowie's solution was improved by Tweed and Rooke (Ref. 17). The numerical results due to Tweed and Rooke were curve-fitted into an expression by Brussat et al (Ref. 3) as shown below.

$$CR_{ho1} = \frac{K}{\sigma\sqrt{\pi a}} = \exp\left[1.2133 - 2.205\left(\frac{a}{a+R}\right) + 0.6451\left(\frac{a}{a+R}\right)^2\right] \tag{24}$$

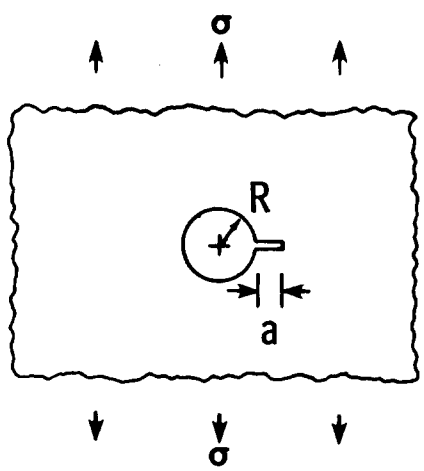

Figure 2. A Crack Emanating from a Fastener Hole - Remote Stress

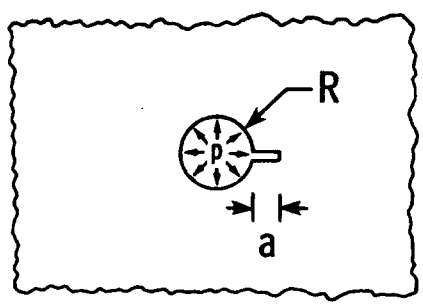

Figure 3. A Crack Emanating from A Fastener Hole - Uniform Pressure

The SIF of a through-crack emanating from a circular hole, which is subjected to uniform internal pressure as shown in Figure 3, was solved by Tweed and Rooke (Ref. 18). In this investigation, The Tweed and Rooke's numerical values were curve-fitted into the following expression.

$$CP_{ho1} = \frac{K}{p\sqrt{\pi a}} = \exp\left[0.11926 - 2.22644\left(\frac{a}{a+R}\right) + 2.69981\left(\frac{a}{a+R}\right)^2 - 12.54211\left(\frac{a}{a+R}\right)^3 + 19.76043\left(\frac{a}{a+R}\right)^4 - 12.66919\left(\frac{a}{a+R}\right)^5\right] \tag{25}$$

Table 2 shows a comparison of Equation (25) with Tweed and Rooke's numerical results. The deviation of Equation (25) from Tweed and Rooke's results is within 0.6%.

3.1.2 Two Unequal Through Cracks Emanating From A Fastener Hole

Tweed and Rooke (Ref. 18) have solved the problem of two unequal through cracks emanating from a fastener hole for the cases of remote stress and uniform internal pressure as shown in Figures 4 and 5. For the case of remote stress, Tweed and Rooke's numerical results are curve-fitted into Equations (26) and (27). Table 3 shows a comparison of Equations (26) and (27) with Tweed and Rooke's numerical results. The deviation of Equation (26) and (27) from Tweed and Rooke's results is within 2%. Equation (28) was given by Tweed and Rooke (Ref. 18).

$$CR_{ho2} = \frac{K}{\sigma\sqrt{\pi a_1}} = CR_{ho1} \cdot F_1 \qquad \text{for} \quad \frac{a_1}{R} \leq 5 \text{ and } \frac{a_2}{R} \leq 5 \tag{26a}$$

$$F_1 = RKO + RK1\left(\frac{a_1}{R}\right) + RK2\left(\frac{a_1}{R}\right)^2 \tag{26b}$$

$$RKO = 0.993522 + 0.157907\left(\frac{a_2}{R}\right) - 0.00579398\left(\frac{a_2}{R}\right)^2 \tag{26c}$$

$$RK1 = 0.00457513 - 0.032251927\left(\frac{a_2}{R}\right) + 0.00517178\left(\frac{a_2}{R}\right)^2 - 0.000408155\left(\frac{a_2}{R}\right)^3 \tag{26d}$$

$$RK2 = -0.00031020177 + 0.001974207\left(\frac{a_2}{R}\right) - 0.0005974349\left(\frac{a_2}{R}\right)^2 + 0.00005767606\left(\frac{a_2}{R}\right)^3 \tag{26e}$$

$$CR_{ho2} = \frac{K}{\sigma\sqrt{\pi a_1}} = \exp\left[1.21009 - 2.1114\left(\frac{a_1}{a_1+R}\right) + 0.92466\left(\frac{a_1}{a_1+R}\right)^2\right] \qquad \text{for } a_1 = a_2 \tag{27}$$

$$CR_{ho2} = \frac{K}{\sigma\sqrt{\pi a_1}} = CR_{ho1} \cdot \sqrt{\frac{\frac{a_1}{R} + \frac{a_2}{R} + 2}{2 + \frac{a_1}{R}}} \qquad \text{for } \frac{a_1}{R} \geq 5 \quad \text{or} \quad \frac{a_2}{R} \geq 5 \tag{28}$$

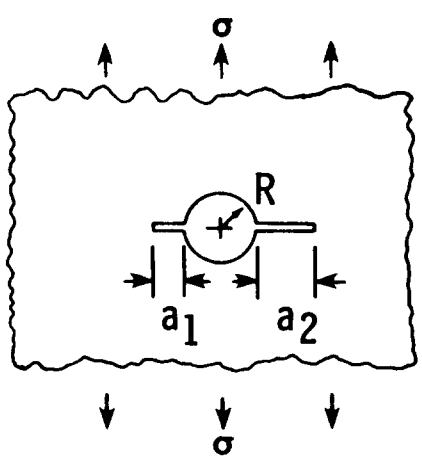

Figure 4. Two Cracks Emanating From A Fastener Hole - Remote Stress

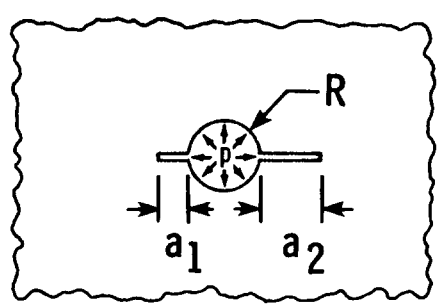

Figure 5. Two Cracks Emanating From A Fastener Hole - Uniform Pressure

For the case of uniform internal pressure as shown in Figure 5, Tweed and Rooke's numerical results are curve-fitted into Equations (29a) through (29i). Table 2 shows a comparison of Equations (29a) through (29i) with Tweed and Rooke's numerical results. The deviation from Tweed and Rooke's result is within 0.6%. Equation (29i) was given by Tweed and Rooke (Ref. 18).

$$CP_{ho2} = \frac{K}{p\sqrt{\pi a_1}} = CP_{ho1} \cdot F_2 \qquad \text{for } \frac{a_1}{R} < 5 \quad \text{and} \quad \frac{a_2}{R} < 5 \tag{29a}$$

$$F_2 = RK0 + RK1\left(\frac{a_1}{R}\right) + RK2\left(\frac{a_1}{R}\right)^2 + RK3\left(\frac{a_1}{R}\right)^3 \tag{29b}$$

$$RK0 = 0.97484 + 0.19014\left(\frac{a_2}{R}\right) - 0.04186\left(\frac{a_2}{R}\right)^2 + 0.0036359\left(\frac{a_2}{R}\right)^3 \tag{29c}$$

$$RK1 = -0.0068344 + 0.021689\left(\frac{a_2}{R}\right) + 0.0047001\left(\frac{a_2}{R}\right)^2 - 0.0010094\left(\frac{a_2}{R}\right)^3 \tag{29d}$$

$$RK2 = 0.002338 - 0.00029425\left(\frac{a_2}{R}\right) - 0.0026977\left(\frac{a_2}{R}\right)^2 + 0.00049749\left(\frac{a_2}{R}\right)^3 \tag{29e}$$

$$RK3 = -0.00022626 - 0.00024296\left(\frac{a_2}{R}\right) + 0.00038673\left(\frac{a_2}{R}\right)^2 - 0.000067379\left(\frac{a_2}{R}\right)^3 \tag{29f}$$

$$CP_{ho2} = \frac{K}{p\sqrt{\pi a_1}} = \exp\left[0.1174204 - 2.154486\left(\frac{a_1}{a_1+R}\right) + 2.2570372\left(\frac{a_1}{a_1+R}\right)^2 - 9.760309\left(\frac{a_1}{a_1+R}\right)^3 + 14.54895\left(\frac{a_1}{a_1+R}\right)^4 - 9.070292\left(\frac{a_1}{a_1+R}\right)^5\right] \tag{29g}$$

$$\text{for } a_1 = a_2 \quad \text{and} \quad \frac{a_1}{R} < 5$$

$$CP_{ho2} = \frac{K}{p\sqrt{\pi a_1}} = \frac{2}{\pi\sqrt{\frac{a_1}{R}\left(\frac{a_1}{R}+1\right)}} \qquad \text{for } a_1 = a_2 \quad \text{and} \quad \frac{a_1}{R} > 5 \tag{29h}$$

$$CP_{ho2} = \frac{K}{p\sqrt{\pi a_1}} = CP_{ho1} \cdot \sqrt{\frac{\left(1+\frac{a_2}{R}\right)\left(2+\frac{a_1}{R}\right)}{\left(2+\frac{a_2}{R_1}+\frac{a_1}{R}\right)}} \qquad \text{for } \frac{a_1}{R} > 5 \quad \text{or} \quad \frac{a_2}{R} > 5 \tag{29i}$$

TABLE 2. COMPARISON OF CP_{ho1} and CP_{ho2}

$A_2/R =$	0.0			0.5			1.0			2.0			5.0		
$A_1/R =$	Tweed & Rooke	This Study	% Dev	Tweed & Rooke	This Study	% Dev	Tweed & Rooke	This Study	% Dev	Tweed & Rooke	This Study	% Dev	Tweed & Rooke	This Study	% Dev
0.01	1.099	1.102	0.307	1.165	1.169	0.302	1.241	1.246	0.378	1.347	1.352	0.335	1.485	1.492	0.439
0.02	1.078	1.080	0.144	1.143	1.144	0.117	1.218	1.220	0.156	1.321	1.324	0.192	1.457	1.461	0.250
0.05	1.020	1.018	-0.170	1.081	1.079	-0.151	1.152	1.151	-1.117	1.250	1.248	-0.128	1.378	1.378	-0.020
0.10	0.935	0.933	-0.177	0.991	0.989	-0.167	1.056	1.055	-0.125	1.146	1.144	-0.150	1.264	1.263	-0.094
0.15	0.863	0.863	-0.046	0.915	0.914	-0.070	0.975	0.975	-0.026	1.058	1.058	-0.042	1.168	1.167	-0.077
0.2	0.800	0.802	0.188	0.849	0.850	0.070	0.905	0.906	0.078	0.982	0.983	0.066	1.085	1.084	-0.052
0.3	0.697	0.700	0.383	0.740	0.743	0.370	0.790	0.792	0.284	0.858	0.861	0.343	0.950	0.952	0.238
0.5	0.551	0.551	0.041	0.586	0.586	-0.028	0.626	0.626	0.028	0.682	0.683	0.156	0.759	0.760	0.141
0.7	0.452	0.451	-0.321	0.481	0.479	-0.324	0.515	0.513	-0.301	0.564	0.562	-0.346	0.630	0.629	-0.138
1.0	0.352	0.351	-0.353	0.375	0.374	-0.265	0.403	0.402	-0.343	0.443	0.442	-0.293	0.500	0.499	-0.253
1.5	0.251	0.252	0.434	0.269	0.270	0.289	0.290	0.291	0.289	0.321	0.322	0.308	0.368	0.369	0.178
2.0	0.192	0.193	0.389	0.206	0.207	0.515	0.223	0.224	0.438	0.248	0.249	0.526	0.288	0.289	0.408
4.0	0.090	0.090	-0.518	0.098	0.097	-0.528	0.107	0.106	-0.522	0.121	0.120	-0.567	0.146	0.145	-0.498
6.0	0.055	0.055	0.121	0.060	0.060	0.132	0.066	0.066	0.123	0.076	0.076	0.137	0.093	0.093	0.124

TABLE 3. COMPARISON OF CR_{ho2}

$A_2/R=$	0.5			1.0			2.0			5.0		
$A_1/R=$	Tweed & Rooke	This Study	% Dev	Tweed & Rooke	This Study	% Dev	Tweed & Rooke	This Study	Tweed % Dev	& Rooke	This Study	% Dev
0.01	3.490	3.526	1.020	3.749	3.771	0.581	4.216	4.233	0.398	5.324	5.391	1.251
0.02	3.418	3.451	0.973	3.672	3.691	0.515	4.130	4.142	0.304	5.216	5.275	1.129
0.05	3.220	3.247	0.855	3.460	3.472	0.346	3.893	3.895	0.059	4.920	4.958	0.769
0.10	2.941	2.962	0.711	3.161	3.165	0.125	3.558	3.548	-0.265	4.501	4.513	0.269
0.15	2.711	2.729	0.655	2.915	2.914	-0.223	3.282	3.265	-0.505	4.156	4.150	0.146
0.20	2.520	2.536	0.619	2.710	2.707	-0.124	3.052	3.031	-0.697	3.866	3.849	-0.446
0.30	2.221	2.236	0.664	2.388	2.384	-0.162	2.690	2.666	-0.888	3.410	3.380	-0.863
0.50	1.832	1.848	0.852	1.968	1.966	-0.088	2.213	2.193	-0.899	2.803	2.872	-1.097
0.70	1.595	1.611	1.001	1.710	1.711	-0.059	1.918	1.903	-0.759	2.423	2.398	-1.013
1.00	1.378	1.393	1.095	1.471	1.475	0.289	1.643	1.635	-0.501	2.061	2.050	-0.537
1.50	1.182	1.194	1.060	1.254	1.259	0.398	1.388	1.386	-0.137	1.719	1.723	0.261
2.00	1.075	1.085	1.894	1.134	1.138	0.348	1.244	1.245	-0.063	1.522	1.534	0.794
3.00	0.962	0.967	0.510	1.005	1.006	0.086	1.087	1.086	-0.056	1.300	1.313	1.040
5.00	0.866	0.865	-0.002	0.895	0.888	-0.776	0.950	0.936	-1.473	1.098	1.083	-1.341

3.1.3 Two Symmetric Corner Cracks Emanating From A Fastener Hole

Newman and Raju (Ref. 19) have solved the problem shown in Figure 6 using the three-dimensional finite element method. Their solution is rewritten in the following expression:

$$CR_{cor2} = \frac{K}{\sigma\sqrt{\pi c}} = \sqrt{\frac{a}{c}\,\frac{1}{Q}}\; F_{ch}\left(\frac{a}{c}, \frac{a}{t}, \phi\right) \tag{30}$$

where Q and F_{ch} are available in closed form expressions given in Ref. 19.

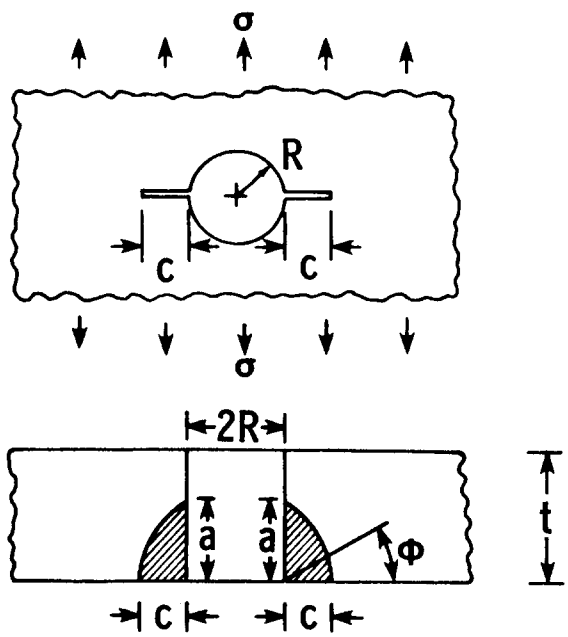

Figure 6. Two Symmetric Corner Cracks Emanating From A Fastener Hole - Remote Stress

For the case of uniform pressure as shown in Figure 7, the SIF is obtained in this investigation using the similarity principle shown in Figure 8 where no finite width effect exists.

$$\frac{K_A}{K_B} = \frac{K_C}{K_D} \tag{31}$$

$$K_A = \left(\frac{K_C}{K_D}\right) K_B \tag{32}$$

According to Equation (32), the correction factor for two symmetric cracks emanating from a circular hole under uniform internal pressure is given in the following expression:

$$CP_{cor2} = \frac{K}{p\sqrt{\pi c}} = \left(\frac{CR_{cor2}}{CR_{ho2}}\right) CP_{ho2} \tag{33}$$

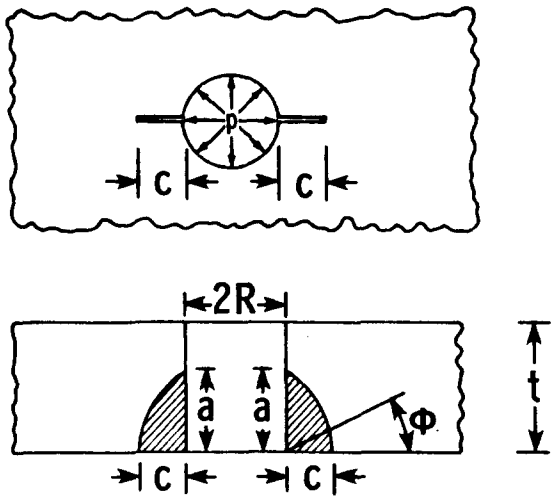

Figure 7. Two Symmetric Corner Cracks Emanating From A Fastener Hole - Uniform Pressure

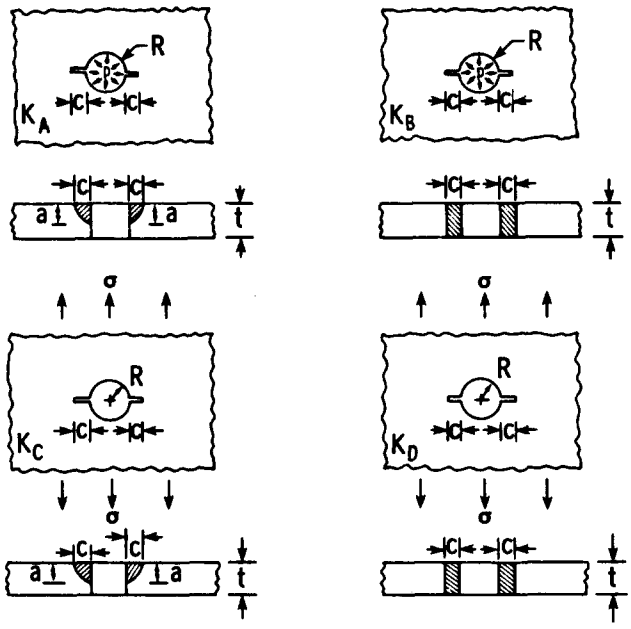

Figure 8. Illustration of Similarity for Figure 7

3.1.4 A Corner Crack Emanating From A Fastener Hole

Newman and Raju (Ref. 19) have solved the problem of a corner crack emanating from a fastener hole under remote stress, as shown in Figure 9, using the three-dimensional finite element method. Their solution is rewritten in the following expression. The square-root term in Equation (34) is Shah's conversion factor (Ref. 30) to convert the solution for two symmetric corner cracks to the solution for one corner crack.

$$CR_{cor1} = \frac{K}{\sigma\sqrt{\pi c}} = CR_{cor2}\sqrt{\frac{8\,Rt + \pi ac}{8\,Rt + 2\pi ac}} \tag{34}$$

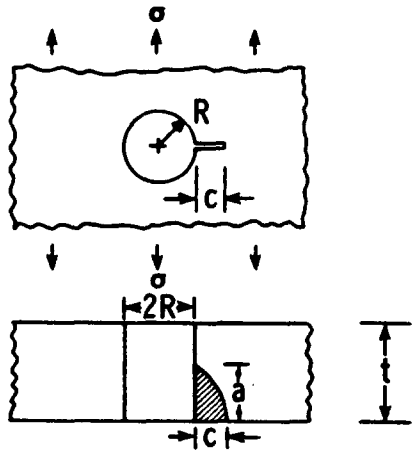

Figure 9. A Corner Crack Emanating From A Fastener Hole - Remote Stress

For the case of uniform internal pressure shown in Figure 10, the SIF was obtained in this investigation using the similarity principle shown in Figure 8 where the two symmetric cracks were replaced by a corner crack. The correction factor for Figure 10 is given below.

$$CP_{cor1} = \frac{K}{p\sqrt{\pi c}} = \frac{CR_{cor1}}{CR_{ho1}} \cdot CP_{ho1} \tag{35}$$

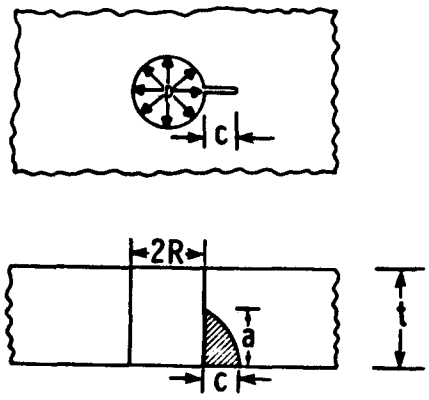

Figure 10. A Corner Crack Emanating From A Fastener Hole - Uniform Pressure

3.1.5 Two Asymmetric Corner Cracks Emanating From A Fastener Hole

The SIF of two asymmetric corner cracks emanating from a fastener hole under remote stress, shown in Figure 11, was estimated in this investigation using the similarity principle shown in Figure 12. The SIF of crack No. 1 in Figure 11 can be obtained in the following manner.

$$\frac{K_A}{K_C} = \frac{K_B}{K_D} \tag{36}$$

$$K_A = \left(\frac{K_C}{K_D}\right) K_B \tag{37}$$

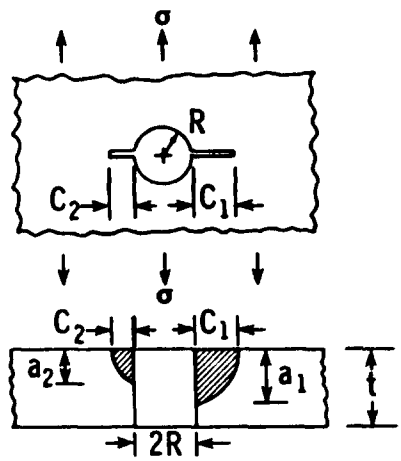

Figure 11. Two Asymmetric Corner Cracks Emanating From A Fastener Hole - Remote Stress

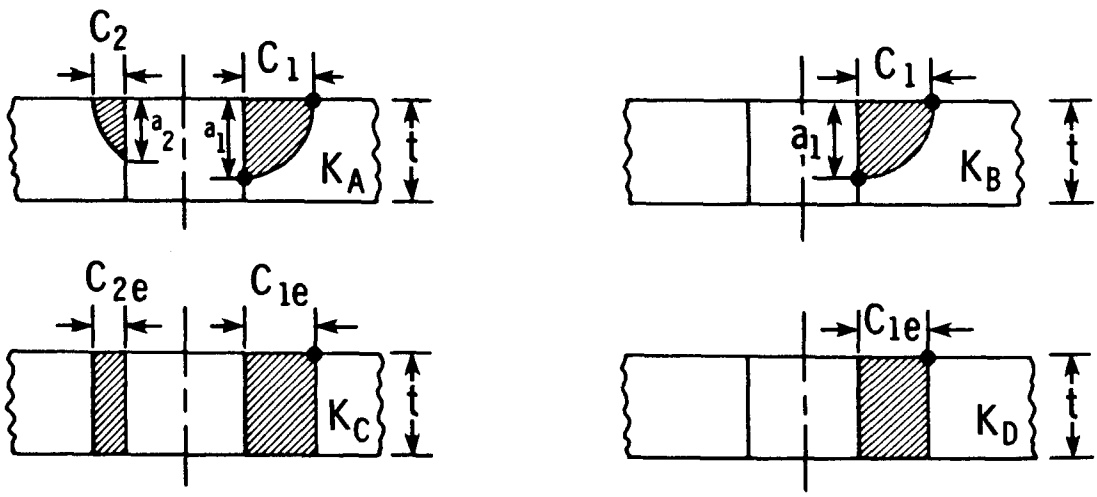

Figure 12. Illustration of Similarity for Figure 11

$$CR_{acor2} = \frac{K}{\sigma\sqrt{\pi c_1}} = \left(\frac{CR_{cor1}}{CR_{ho1}}\right) CR_{ho2} \tag{38}$$

where CR_{cor1} shall be evaluated with a_1 and C_1 as independent variables for crack No. 1. Similarly, the SIF of crack No. 2 in Figure 11 can be estimated with Equation (38); however, CR_{cor1} shall be evaluated with a_2 and C_2 as independent variables. In the calculation of CR_{ho1} and CR_{ho2}, the effective crack lengths as defined in Equations (39a) and (39b) shall be used.

$$c_{1e} = \sqrt{\frac{a_1}{t}}\ c_1 \tag{39a}$$

$$c_{2e} = \sqrt{\frac{a_2}{t}}\ c_2 \tag{39b}$$

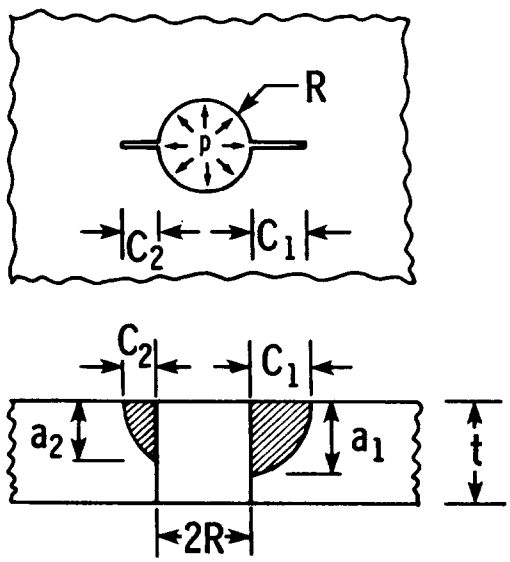

Figure 13. Two Asymmetric Corner Cracks Emanating From A Fastener Hole - Uniform Pressure

For the case of fastener load as shown in Figure 13, the same similarity principle shown in Figure 12 is used to estimate SIF of crack No. 1.

$$CP_{acor2} = \frac{K}{p\sqrt{\pi c_1}} = \left(\frac{CP_{cor1}}{CP_{ho1}}\right) CP_{ho2} \tag{40}$$

where CP_{cor1} shall be evaluated with a_1 and C_1 as independent variables. Similarly, the SIF of crack No. 2 in Figure 13 can be estimated with Equation (40); however, CP_{cor1} shall be evaluated with a_2 and C_2 as independent variables. In the calculation of CP_{ho1} and CP_{ho2}, the effective crack lengths as defined in Equations (39a) and (39b) shall be used.

3.1.6 A Corner And A Through Crack Emananting From A Fastener Hole

The SIF of a corner and a through crack emanating from a fastener hole under remote stress (Figure 14) can be estimated using the same procedure shown in Figure 12. The SIF of the corner crack is given in Equation (41). The CR_{cor1} shall be evaluated using C_2 and a_2 as independent variables. The CR_{ho1} and CR_{ho2} shall be evaluated using C_1 and C_{2e} as independent variables. The C_{2e} is the effective crack length for the corner crack and is defined in Equations (39b).

$$CR_{coth} = \frac{K}{\sigma\sqrt{\pi c_2}} = \left(\frac{CR_{cor1}}{CR_{ho1}}\right) CR_{ho2} \tag{41}$$

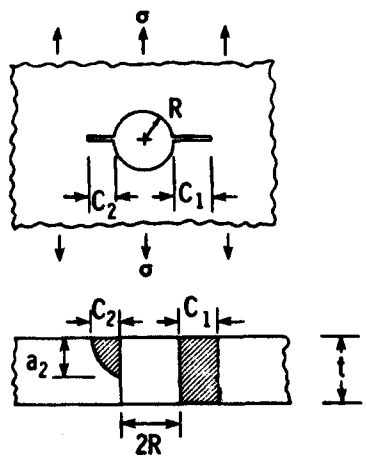

Figure 14. A Corner and A Through Crack Emanating From A Fastener Hole - Remote Stress

The SIF for the through crack is given below.

$$CR_{coth} = \frac{K}{\sigma\sqrt{\pi c_1}} = CR_{ho2} \tag{42}$$

where CR_{ho2} shall be evaluated with C_1 and C_{2e} as independent variables. The C_{2e} is the effective crack length for the corner crack and is defined in Equation (39b).

Similarly, the SIF due to uniform internal pressure (Figure 15) is estimated in Equation (43) for the corner crack. The CP_{cor1} shall be evaluated using C_2 and a_2 as independent variables. The CP_{ho1} and CP_{ho2} shall be evaluated using C_1 and C_{2e} as independent variables. The C_{2e} is defined in Equation (39b).

$$CP_{coth} = \frac{K}{p\sqrt{\pi c_2}} = \left(\frac{CP_{cor1}}{CP_{ho1}}\right) CP_{ho2} \tag{43}$$

The SIF for the through crack, shown in Figure 15, is given as,

$$CP_{coth} = \frac{K}{p\sqrt{\pi c_1}} = CP_{ho2} \tag{44}$$

where CP_{ho2} shall be evaluated with C_1 and C_{2e}.

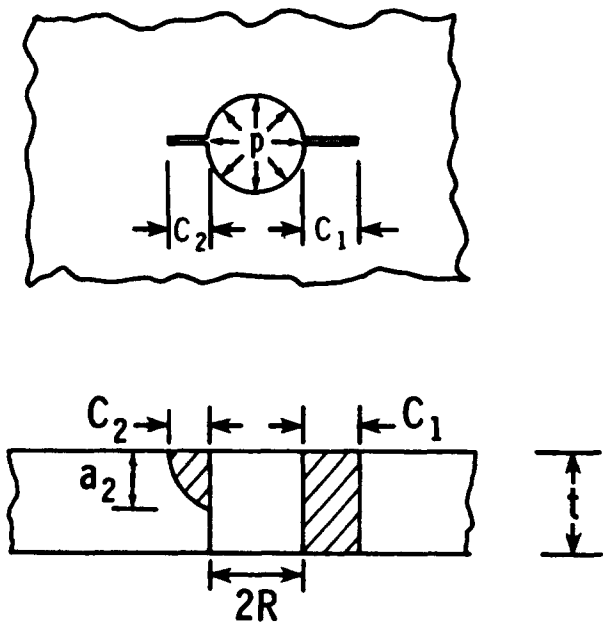

Figure 15. A Corner And A Through Crack Emanating From A Fastener Hole - Uniform Pressure

3.1.7 A Through Crack Emanating From An Internal Notch

The configuration of a through crack emanating from an internal notch under remote stress, shown in Figure 16, can be modeled as the configuration shown in Figure 17 (Ref. 20) which shows the SIF's are approximately the same when a/(a + b) is not smaller than 0.11 and c/b is not larger than 1.0. When c/b equals 1.0, the ellipse becomes a circle. Therefore, Equation (24) for a circle is applicable to Figure 16 for a/(a+b) being equal to or larger than 0.11; and the correction factor for Figure 16 is given as,

$$CR_{2ho1} = \frac{K}{\sigma\sqrt{\pi a}} = CR_{ho1}, \qquad \frac{a}{a+b} \geqslant 0.11 \tag{45}$$

where CR_{ho1} shall be evaluated by replacing "R" in Equation (24) with "b" in Figure 16. For the case of a/(a + b) being smaller than 0.11, Schijve's solution (Ref. 21), as given below, is applicable.

$$CR_{2ho1} = \frac{K}{\sigma\sqrt{\pi a}} = k_{tg} \cdot F \tag{46}$$

$$F = 1.1215 - 3.21\left(\frac{a}{R}\right) + 5.16\left(\frac{a}{R}\right)^{1.5} - 3.73\left(\frac{a}{R}\right)^{2} + 1.14\left(\frac{a}{R}\right)^{2.5} \tag{47}$$

where k_{tg} is given later in Equation (105). According to Schijve (Ref. 21), Equation (47) is applicable for $a/R \leq 1$. Normally, the "b" in Figure 16 equals to about 5R. Therefore, the condition $a/(a + b) < .11$ results in $a/R < 0.62$; and Equation (47) is applicable for $a/(a + b) < 0.11$.

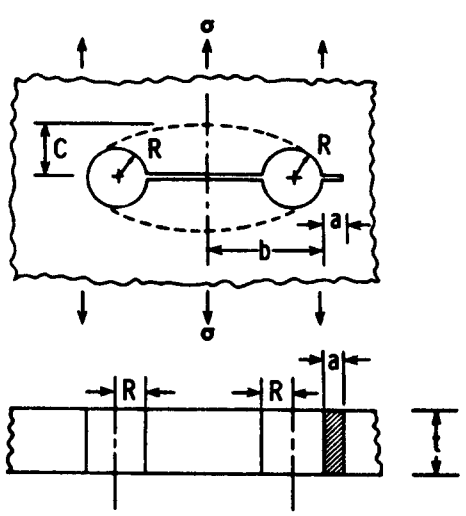

Figure 16. A Through Crack Emanating From An Internal Notch - Remote Stress

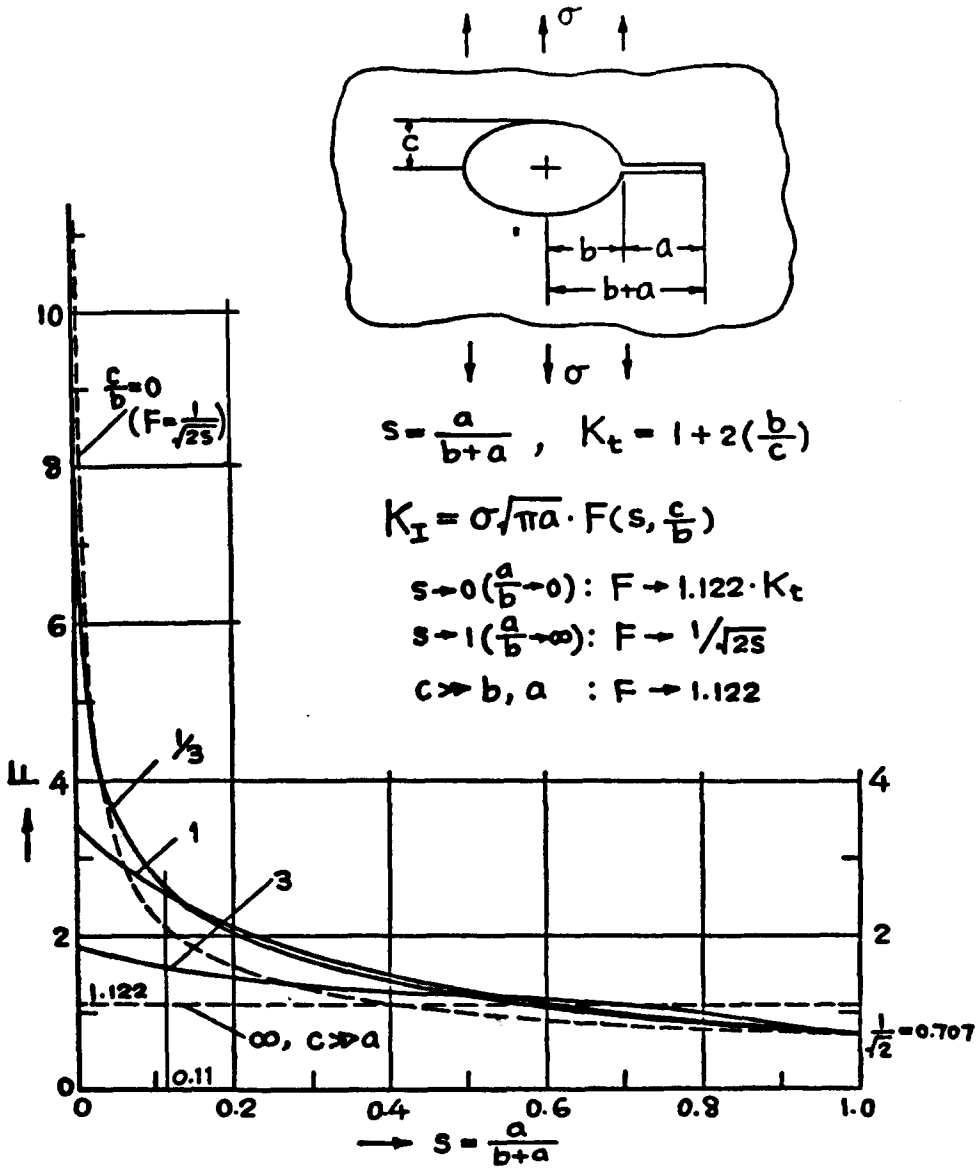

Figure 17. A Through Crack Emanating From An Elliptical Hole - Remote Stress (Ref. 20)

3.1.8 A Corner Crack Emanating From An Internal Notch

The SIF of a corner crack emanating from an internal notch, as shown in Figure 18, can be estimated using the similarity principle shown in Figure 19. The relationship among the configurations shown in Figure 19 is given in Equations (36) and (37). The SIF for the corner crack shown in Figure 18 is given in Equation (48).

$$CR_{2cor1} = \frac{K}{\sigma\sqrt{\pi c}} = \left(\frac{CR_{2ho1}}{CR_{ho1}}\right) \cdot CR_{cor1} \tag{48}$$

where CR_{2ho1} is evaluated with Equations (46) and (47) for $c/(c + b) < 0.11$, and CR_{2ho1} is evaluated with Equation (45) for $c/(c + b) \geq 0.11$.

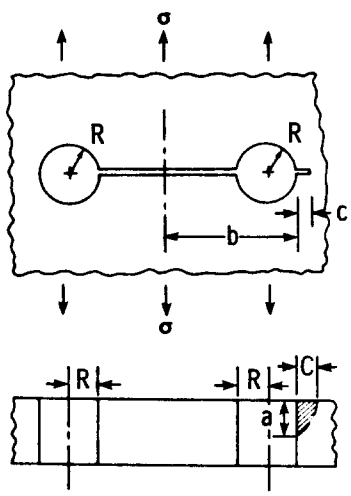

Figure 18. A Corner Crack Emanating From An Internal Notch - Remote Stress

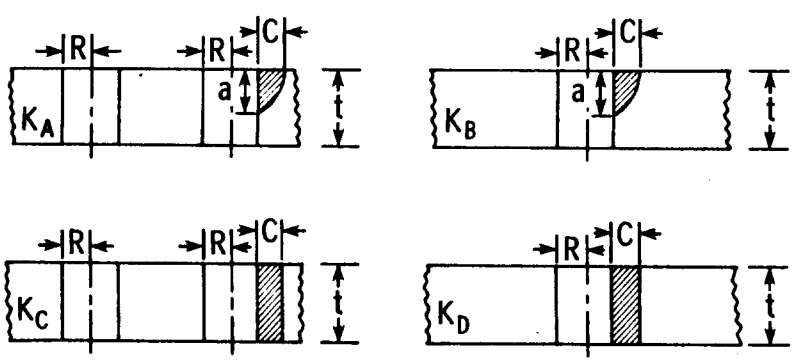

Figure 19. Illustration of Similarity for Figure 18.

3.1.9 Two Through Cracks Emanating From An Internal Notch

The problem of two through cracks emanating from an internal notch under remote stress, shown in Figure 20, can be modeled in the manner shown in Figure 21, which shows that the SIF's are approximately the same when $a/(a+b) \geq 0.18$ and $c/b \leq 1.0$. When c/b equals 1.0, the ellipse becomes a circle. Therefore, Equation (26) for a circle is applicable to Figure 20 for $a/(a+b) \geq 0.18$. For crack No. 1,

$$CR_{2ho2} = \frac{K}{\sigma\sqrt{\pi a_1}} = CR_{2ho1} \cdot F_3 \quad \text{for } \frac{a_1}{b} < 5 \quad \text{and} \quad \frac{a_2}{b} < 5 \tag{49}$$

$$CR_{2ho1} = \exp\left[1.2133 - 2.205\left(\frac{a_1}{a_1+b}\right) - 0.6451\left(\frac{a_1}{a_1+b}\right)^2\right] \tag{50}$$

$$F_3 = RK0 + RK1\left(\frac{a_1}{b}\right) + RK2\left(\frac{a_1}{b}\right)^2 \tag{51}$$

$$\left.\begin{aligned} RK0 &= 0.993522 + 0.157907\left(\frac{a_2}{b}\right) - 0.00579398\left(\frac{a_2}{b}\right)^2 \\ RK1 &= 0.00457513 - 0.032251927\left(\frac{a_2}{b}\right) + 0.00517178\left(\frac{a_2}{b}\right)^2 - 0.000408155\left(\frac{a_2}{b}\right)^3 \\ RK2 &= -0.00031020177 + 0.001974207\left(\frac{a_2}{b}\right) - 0.0005974349\left(\frac{a_2}{b}\right)^2 + 0.00005767606\left(\frac{a_2}{b}\right)^3 \end{aligned}\right\} \tag{52}$$

$$CR_{2ho2} = \frac{K}{\sigma\sqrt{\pi a_1}} = \exp\left[1.21009 - 2.1114\left(\frac{a_1}{a_1+b}\right) + 0.92466\left(\frac{a_1}{a_1+b}\right)^2\right] \quad \text{for } a_1 = a_2 \tag{53}$$

$$CR_{2ho2} = \frac{K}{\sigma\sqrt{\pi a_1}} = CR_{2ho1} \cdot \sqrt{\frac{a_1 + 2b + a_2}{2b + a_1}} \quad \text{for } \frac{a_1}{b} > 5 \text{ or } \frac{a_2}{b} > 5 \tag{54}$$

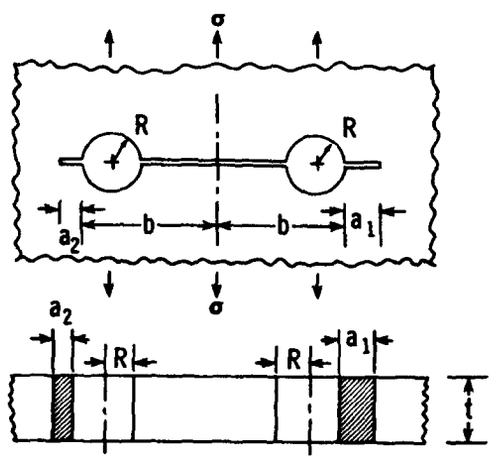

Figure 20. Two Through Cracks Emanating From An Internal Notch - Remote Stress

For the case $a/(a + b) < 0.18$, Schijve's expression (Ref. 21) is applicable.

$$CR_{2ho2} = \frac{K}{\sigma \sqrt{\pi a_1}} = k_{tg} \cdot F \tag{55}$$

$$F = 1.1215 - 3.21 \left(\frac{a_1}{R}\right) + 5.16 \left(\frac{a_1}{R}\right)^{1.5} - 3.73 \left(\frac{a_1}{R}\right)^{2} + 1.14 \left(\frac{a_1}{R}\right)^{2.5} \tag{56}$$

The k_{tg} in Equation (55) can be calculated from Equation (101). For crack No. 2, a_1 and a_2 in Equations (49) through (56) shall be interchanged.

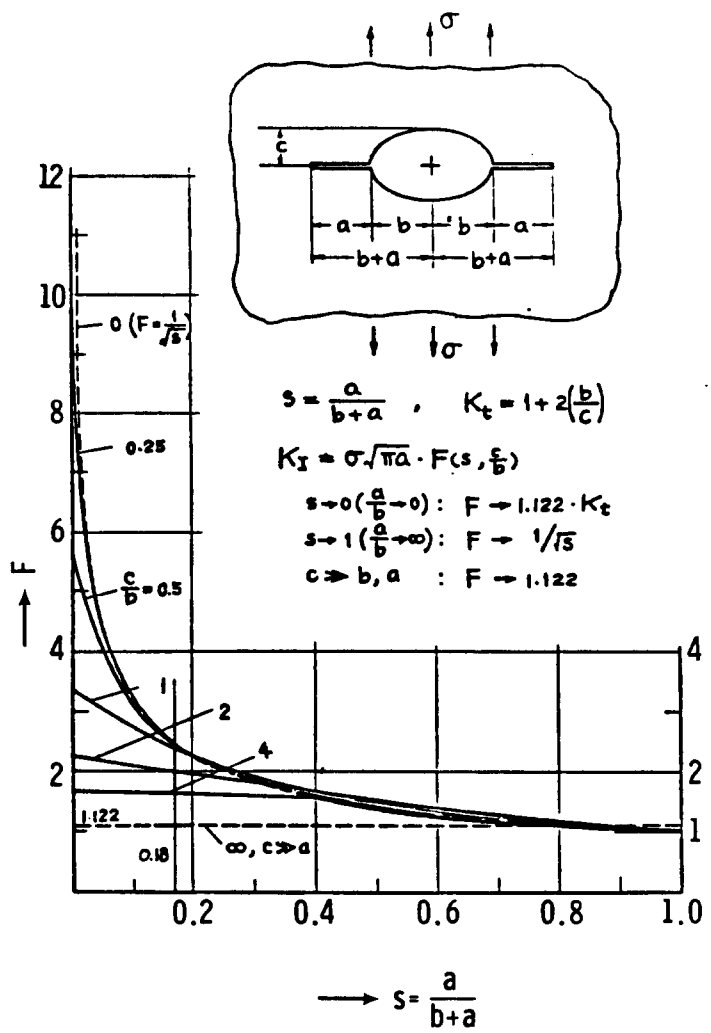

Figure 21. Two Symmetric Cracks Emanating From A Elliptical Hole - Remote Stress (Ref. 20)

3.1.10 Two Corner Cracks Emanating From An Internal Notch

The SIF for the configuration shown in Figure 22 can be obtained using the similarity principle illustrated in Figure 23. The relationship of the configurations shown in Figure 23 is given in Equations (36) and (37). The correction factor for Crack No. 1 in Figure 22 is given in Equation (57).

$$CR_{2cor2} = \frac{K}{\sigma\sqrt{\pi c_1}} = \left(\frac{CR_{2ho2}}{CR_{2ho1}}\right) \cdot CR_{2cor1} = \left(\frac{CR_{2ho2}}{CR_{ho1}}\right) CR_{cor1} \qquad (57)$$

where CR_{2cor1} shall be evaluated with a_1 and C_1 as independent variables. Similarly, the SIF for crack No. 2 can be estimated with Equation (57), where CR_{2cor1} should be evaluated with a_2 and C_2 as independent variables. The CR_{2ho1} and CR_{2ho2} shall be evaluated using effective crack lengths C_{1e} and C_{2e} as defined in Equations (39a) and (39b).

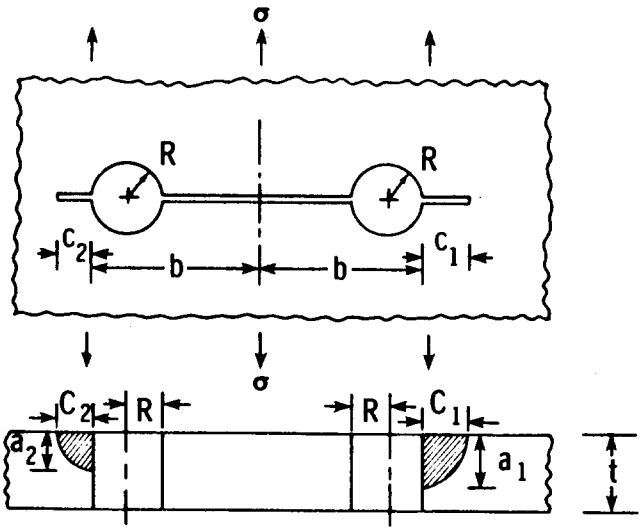

Figure 22. Two Corner Cracks Emanating From An Internal Notch - Remote Stress

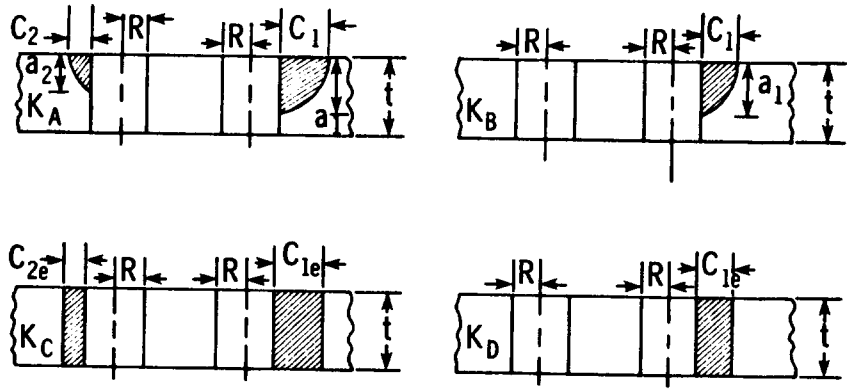

Figure 23. Illustration of Similarity for Figure 22

3.1.11 A Through And A Corner Crack Emanating From An Internal Notch

The SIF of the configuration shown in Figure 24 can be estimated using the similarity shown in Figure 23. The correction factor for the corner crack is given in Equation (58). The CR_{2cor1} shall be evaluated using C_2 and a_2 as independent variables. The CR_{2ho2} and CR_{2ho1} shall be evaluated using C_1 and C_{2e} as independent variables. The effective crack length C_{2e} is defined in Equation (39b).

$$CR_{2coth} = \frac{K}{\sigma\sqrt{\pi c_2}} = \left(\frac{CR_{2ho2}}{CR_{2ho1}}\right) \cdot CR_{2cor1} \tag{58}$$

The correction factor for the through crack is given below,

$$CR_{2coth} = \frac{K}{\sigma\sqrt{\pi c_1}} = CR_{2ho2} \tag{59}$$

where CR_{2ho2} shall be evaluated with C_1 and C_{2e} as independent variables. The C_{2e} is the effective crack length for the corner crack and is defined in Equation (39b).

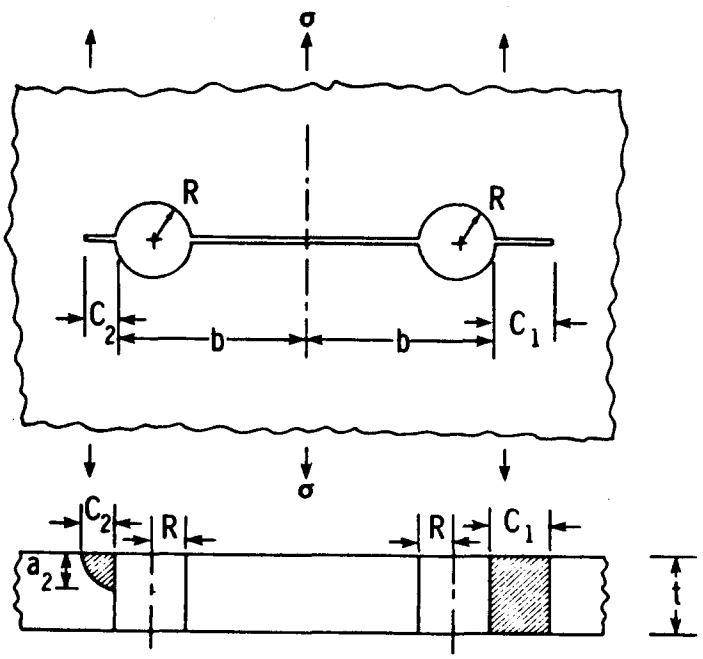

Figure 24. A Through And A Corner Crack Emanating from An Internal Notch - Remote Stress

3.1.12 A Through Crack Emanating From An Edge Notch

The SIF for a through crack emanating from an edge notch under remote stress, shown in Figure 25, can be approximated by the solution given in Figure 26. This shows that the SIF's are approximately the same when $s = a/(a + b) \geq 0.10$ and $c/b \leq 0.5$. For the airframe structures, the c/b is usually less than 0.5.

$$CR_{egt} = \frac{K}{\sigma\sqrt{\pi a}} = \exp\left[1.622013 - 4.256582 \cdot S + 4.748848 \cdot S^2 - 2.002491 \cdot S^2\right] \quad \text{for } S \geq 0.1 \tag{60}$$

When s is less than 0.10, Schijve's formula (Ref. 21) is applicable.

$$CR_{egt} = \frac{K}{\sigma\sqrt{\pi a}} = k_{tg-4} \cdot F \quad \text{for } S < 0.10 \tag{61}$$

where k_{tg-4} and F are available from Equations (108) and (47), respectively. Note that k_{tg-4} for a semi-infinite plate can be calculated by setting "b" (in Figure 101) equal to infinite in equation (108).

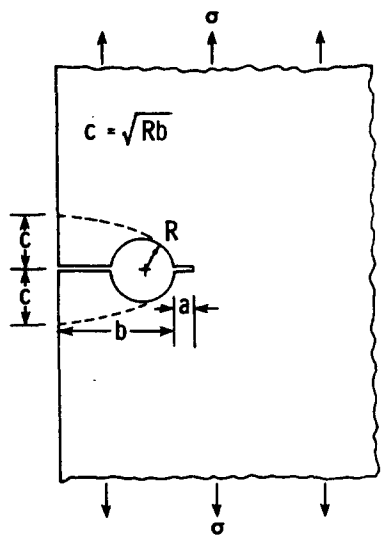

Figure 25. A Through Crack Emanating From An Edge Notch - Remote Stress

For the case of uniform pressure as shown in Figure 27, the SIF can be obtained by the similarity shown in Figure 28.

$$CP_{egt} = \frac{K_A}{p\sqrt{\pi a}} = \left[\left(\frac{K_C}{K_D}\right) K_B\right] \frac{1}{p\sqrt{\pi a}} = \left[\left(\frac{CR_{egt} \cdot \sigma\sqrt{\pi a}}{CR_{sweg} \cdot \sigma\sqrt{\pi A}}\right) CP_{sweg} \frac{P}{\sqrt{\pi A}}\right] \frac{1}{p\sqrt{\pi a}} \tag{62}$$

$$= \left[\left(\frac{CR_{egt}}{CR_{sweg}}\right) CP_{sweg}\right] \frac{2R}{\pi A}$$

where CR_{sweg}, CP_{sweg} and CR_{egt} are available from Equations (72), (73) and (60) or (61), respectively.

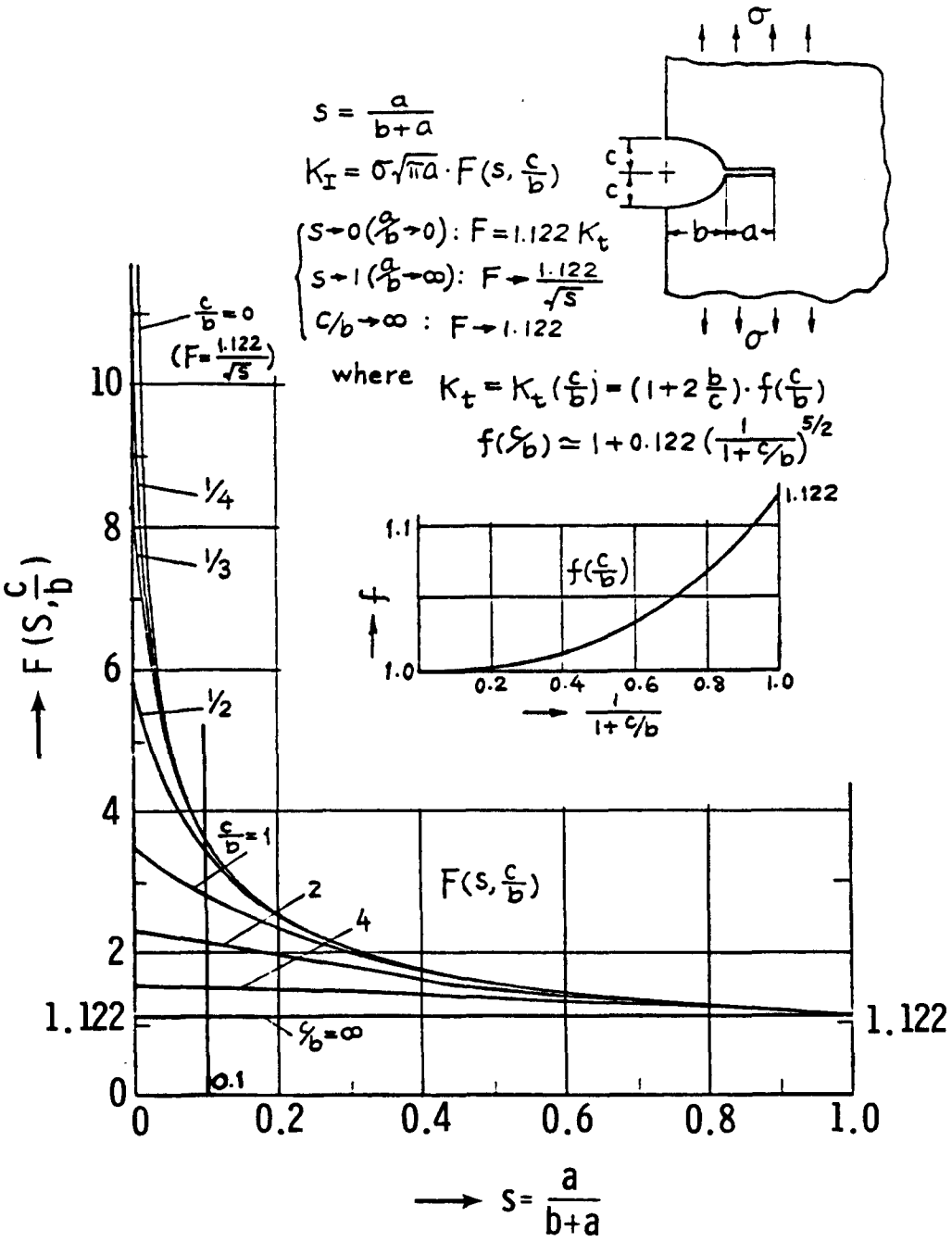

Figure 26. A Through Crack Emanating From An Edge Elliptical Notch - Remote Stress (Ref. 20)

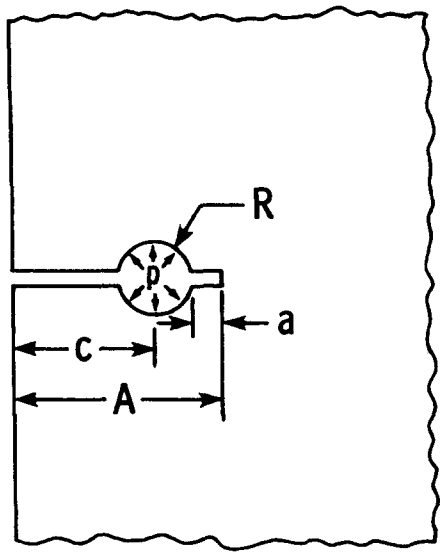

Figure 27. A Through Crack Emanating From An Edge Notch - Uniform Pressure

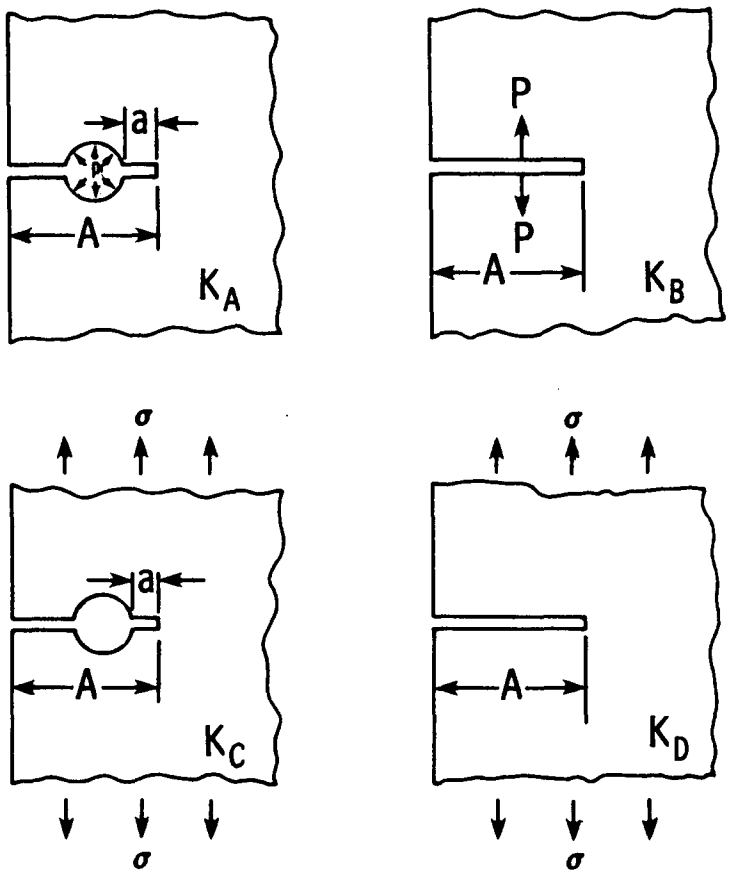

Figure 28. Illustration of Similarity for Figure 27

3.1.13 A Corner Crack Emanating From A Plate Edge

Newman and Raju (Ref. 19) have solved the problem of a corner crack emanating from a plate edge, shown in Figure 29, using the three-dimensional finite element method. Their solution is rewritten in the following expression:

$$CR_{coreg} = \frac{K}{\sigma\sqrt{\pi c}} = \sqrt{\frac{a}{c}\,\frac{1}{Q}}\quad F_c\left(\frac{a}{c}, \frac{a}{t}, \phi\right) \tag{63}$$

where Q and F_c are available in the closed form expression given in Ref. 19.

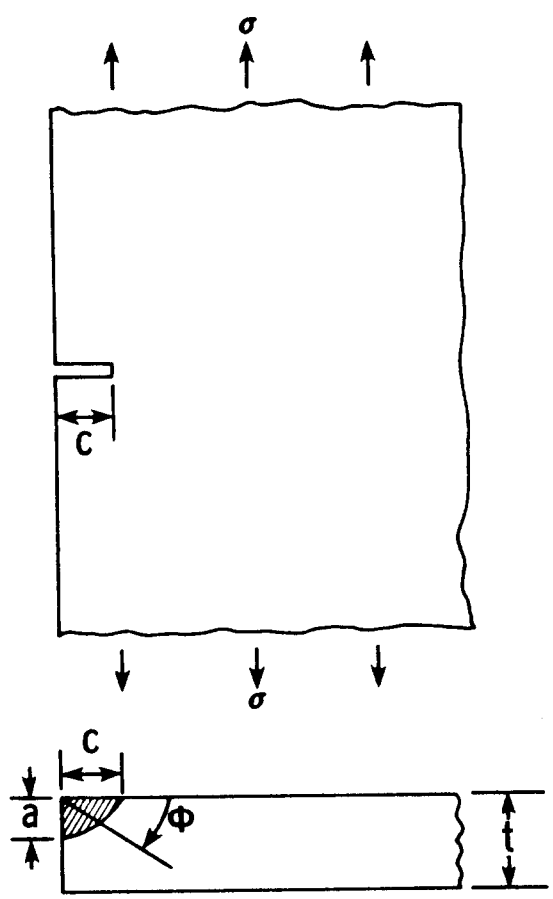

Figure 29. A Corner Crack Emanating From A Plate Edge - Remote Stress

3.1.14 A Corner Crack Emanating From An Edge Notch

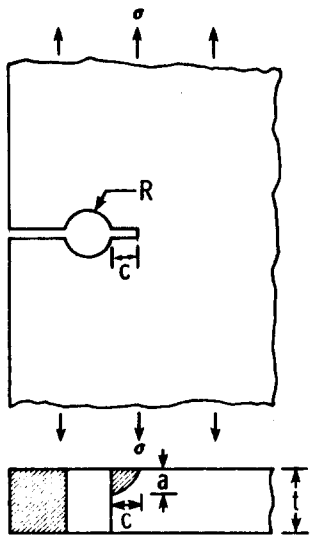

Figure 30-a. A Corner Crack Emanating From An Edge Notch - Remote Stress

The SIF of the configuration shown in Figure 30-a can be obtained by modifying the solution of the corresponding through crack problem shown in Figure 25.

$$CR_{egc} = \frac{K}{\sigma\sqrt{\pi c}} = CR_{egt} \cdot CR_{coreg} \tag{64}$$

For the case of uniform pressure shown in Figure 30-b, the SIF is approximated as,

$$CP_{egc} = \frac{K}{p\sqrt{\pi c}} = CP_{egt} \cdot CR_{coreg} \tag{65}$$

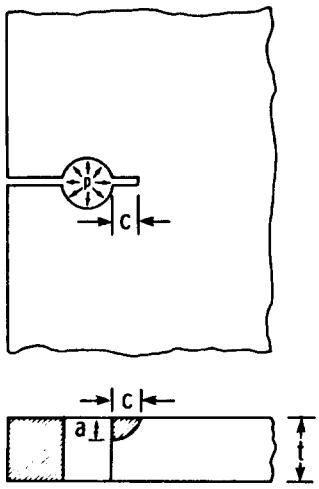

Figure 30-b. A Corner Crack Emanating From An Edge Notch - Uniform Pressure

3.1.15 The Finite Width Correction

Isida (Ref. 22) has solved the problem of finite width effect for the case of remote stress, as shown in Figure 31-a. He gave his results in terms of a 19-term series for various eccentricities of crack locations. His results were curve-fitted into the following simple expressions in this investigation.

$$CR_{fwa} = \sqrt{\operatorname{Sec} \frac{\pi}{6} \left(\frac{2.65a}{b_1} + \frac{0.35a}{b_2} \right)}, \qquad b_1 \leqslant b_2 \tag{66a}$$

$$CR_{fwb} = \sqrt{\operatorname{Sec} \frac{\pi}{6} \left(\frac{1.45a}{b_1} + \frac{1.55a}{b_2} \right)}, \qquad b_1 \leqslant b_2 \tag{66b}$$

A comparison of Equations (66a) and (66b) with Isida's 19-term solution is given in Tables 4 and 5 for $0.5 \leq \lambda$ $(= a/b_1) \leq 0.8$. For $\lambda < 0.5$, the agreement between Isida's data and Equations (66a) and (66b) is better than 2%. Tables 4 and 5 show that some deviations are about 10% for $\lambda = 0.8$, but this would not significantly affect the structural life prediction because the crack will grow at a high rate to reach the free edge.

A prevailing approach to treat crack eccentricity is to take $2b_1$ and $2b_2$ as the effective widths for crack tips A and B, respectively; and the crack is assumed to be in the middle, i.e. ϵ (= e/b) = 0.0. A comparison of this approach with Isida's solution is given in the bottom line of Tables 4 and 5 for $\epsilon = 0.9$. The tables indicate that when the eccentricity is high, this prevailing approach gives very conservative SIFs.

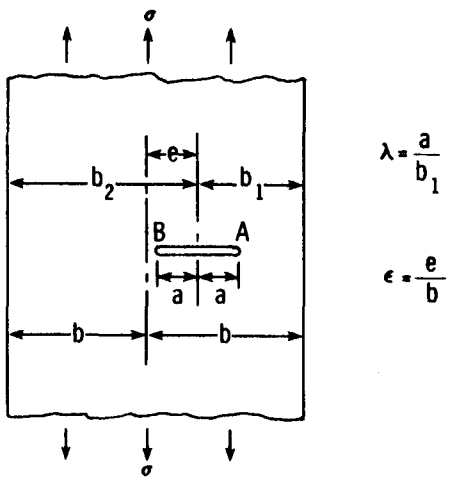

Figure 31-a. An Eccentric Crack In A Finite Plate - Remote Stress

TABLE 4. COMPARISON OF CR_{fwa}

$\lambda =$	0.5			0.6			0.7			0.8		
$\epsilon =$	Isida	This Study	Dev %	Isida	This Study	Dev %	Isida	This Study	Dev %	Isida	This Study	Dev %
0.00	1.1867	1.1892	0.22	1.3033	1.3043	0.08	1.4881	1.4841	-0.26	1.8108	1.7989	-0.65
0.02	1.1837	1.1871	0.28	1.2994	1.3005	0.08	1.4832	1.4769	-0.42	1.8060	1.7832	-1.26
0.04	1.1814	1.1851	0.31	1.2965	1.2968	0.03	1.4799	1.4700	-0.67	1.8039	1.7685	-1.96
0.06	1.1795	1.1831	0.30	1.2943	1.2934	-0.07	1.4777	1.4635	-0.96	1.8034	1.7548	-2.69
0.08	1.1781	1.1813	0.27	1.2927	1.2900	-0.20	1.4764	1.4573	-1.29	1.8041	1.7418	-3.45
0.10	1.1770	1.1795	0.21	1.2915	1.2869	-0.36	1.4757	1.4515	-1.64	1.8054	1.7297	-4.20
0.20	1.1745	1.1717	-0.24	1.2897	1.2730	-1.29	1.4765	1.4262	-3.41	1.8139	1.6781	-7.28
0.30	1.1732	1.1653	-0.67	1.2881	1.2618	-2.04	1.4743	1.4059	-4.64	1.8104	1.6382	-9.51
0.40	1.1695	1.1600	-0.81	1.2812	1.2525	-2.24	1.4614	1.3894	-4.93	1.7841	1.6064	-9.96
0.50	1.1613	1.1555	-0.50	1.2664	1.2447	-1.72	1.4344	1.3756	-4.10	1.7317	1.5804	-8.75
0.60	1.1483	1.1516	0.29	1.2436	1.2380	-0.45	1.3943	1.3640	-2.17	1.6574	1.5589	-5.95
0.70	1.1316	1.1483	1.47	1.2152	1.2323	1.41	1.3460	1.3541	0.60	1.5720	1.5406	-1.99
0.80	1.1136	1.1454	2.85	1.1853	1.2273	3.54	1.2972	1.3454	3.72	1.4893	1.5250	2.40
0.90	1.0984	1.1428	4.03	1.1608	1.2229	5.34	1.2583	1.3379	6.33	1.4260	1.5115	5.99
$\Delta =$	8%			10.6%			18.3%			27%		

$$\Delta = \left[CR_{fwa}\ (\epsilon = 0) - CR_{fwa}\ (\epsilon = 0.9)\right] / CR_{fwa}\ (\epsilon = 0.9)$$

TABLE 5. COMPARISON OF CR_{fwb}

	$\lambda =$ 0.5			0.6			0.7			0.8		
$\epsilon =$	Isida	This Study	Dev %	Isida	This Study	Dev %	Isida	This Study	Dev %	Isida	This Study	Dev %
0.00	1.1867	1.1892	0.22	1.3033	1.3043	0.08	1.4881	1.4841	-0.26	1.8108	1.7989	-0.65
0.02	1.1723	1.1799	0.65	1.2759	1.2876	0.92	1.4342	1.4529	1.31	1.6951	1.7326	2.21
0.04	1.1602	1.1713	0.96	1.2531	1.2724	1.54	1.3910	1.4250	2.44	1.6082	1.6757	4.20
0.06	1.1500	1.1634	1.17	1.2341	1.2584	1.97	1.3562	1.3998	3.22	1.5418	1.6264	5.49
0.08	1.1413	1.1560	1.29	1.2184	1.2456	2.23	1.3280	1.3771	3.70	1.4905	1.5833	6.23
0.10	1.1340	1.1491	1.33	1.2053	1.2337	2.36	1.3051	1.3565	3.94	1.4503	15451	6.54
0.20	1.1126	1.1208	0.74	1.1679	1.1861	1.56	1.2425	1.2766	2.74	1.3484	1.4058	4.25
0.30	1.1058	1.1000	-0.52	1.1565	1.1522	-0.37	1.2249	1.2222	-0.22	1.3236	1.3176	-0.45
0.40	1.1040	1.0842	-1.79	1.1540	1.1269	-2.35	1.2218	1.1831	-3.17	1.3208	1.2571	-4.82
0.50	1.1018	1.0719	-2.71	1.1510	1.1076	-3.77	1.2176	1.1537	-5.25	1.3147	1.2132	-7.72
0.60	1.0961	1.0621	-3.10	1.1424	1.0924	-4.37	1.2047	1.1311	-6.11	1.2942	1.1800	-8.82
0.70	1.0860	1.0540	-2.93	1.1263	1.0802	-4.14	1.1813	1.1132	-5.77	1.2577	1.1543	-8.22
0.80	1.0729	1.0476	-2.35	1.1068	1.0703	-3.30	1.1511	1.0987	-4.55	1.2120	1.1338	-6.45
0.90	1.0603	1.0422	-1.71	1.0876	1.0621	-2.34	1.1227	1.0869	-3.19	1.1702	1.1172	-4.53
$\Delta =$	11.9%			19.8%			29.8%			54.7%		

$$\Delta = \left[CR_{fwb}\ (\epsilon = 0) - CR_{fwb}\ (\epsilon = 0.9)\right] / CR_{fwb}\ (\epsilon = 0.9)$$

For the case of uniform pressure, as shown in Figure 31-b, the finite width correction is obtained by dividing the solution on page 2.32 of Ref. 20 by the solution on page 5.9 of Ref. 20. The correction factor is rewritten in the following expressions

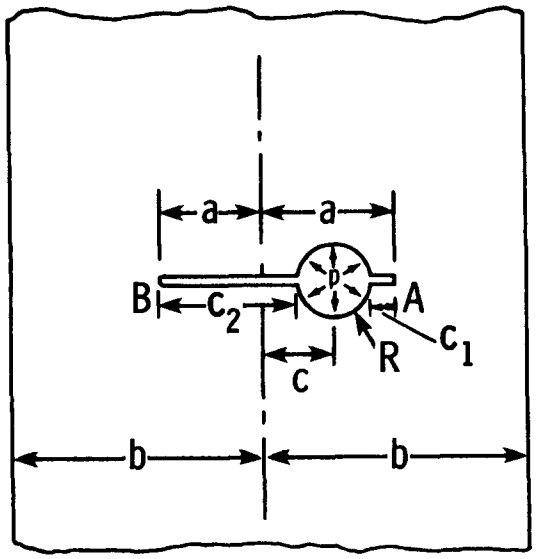

Figure 31-b. A Crack In An Finite Plate - Uniform Pressure

$$\begin{Bmatrix} CP_{fwa} \\ \\ CP_{fwb} \end{Bmatrix} = \begin{Bmatrix} \dfrac{K_a}{p\sqrt{\pi c_1}\cdot CP_{ho2}} \\ \\ \dfrac{K_b}{p\sqrt{\pi c_2}\cdot CP_{ho2}} \end{Bmatrix} = \left[1 + 0.297\sqrt{1-(c/a)^2}\ \left(1 - \cos\frac{\pi a}{2b}\right) \right] \begin{Bmatrix} F_a \\ \\ F_b \end{Bmatrix} \tag{67}$$

$$\begin{Bmatrix} F_a \\ \\ F_b \end{Bmatrix} = \sqrt{\frac{\pi a}{2b}\tan\frac{\pi a}{2b}}\ \frac{1 \begin{Bmatrix} + \\ - \end{Bmatrix} \left(\dfrac{\sin\frac{\pi c}{2b}}{\sin\frac{\pi a}{2b}}\right)}{\sqrt{1-\left(\dfrac{\cos\frac{\pi a}{2b}}{\cos\frac{\pi c}{2b}}\right)^2}}\sqrt{\frac{a \mp c}{a \pm c}} \tag{68}$$

3.1.16 A Crack Approaching A Hole

Isida (Ref. 23) has solved the problem of a crack approaching a hole, as shown in Figure 32. In this investigation, the graph was enlarged to an appropriate size to facilitate reading the numerical values to two digits after the decimal point. Isida's solution was then curve-fitted into the following expression.

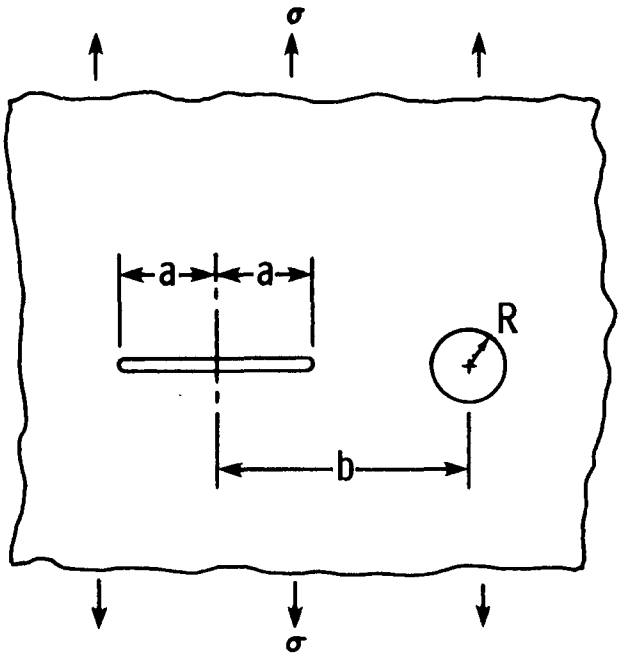

Figure 32. A Crack Approaching A Hole

$$CR_{ah} = \frac{K}{\sigma\sqrt{\pi a}} = F_3 + 2\,(F_4 - F_3)/\pi \tag{69a}$$

$$F_3 = 1 + 0.5\,\mu^2 + 1.5\,\mu^4 \tag{69b}$$

$$F_4 = 1 + 0.5\left(\frac{\mu}{1-\lambda}\right)^2 + 1.5\left(\frac{\mu}{1-\lambda}\right)^4 \tag{69c}$$

where $\mu = R/b$ and $\lambda = a/b$ as shown in Figure 32. A comparison of Equations (69a), (69b) and (69c) with Isida's solution is given in Table 6. The table indicates the deviation is within 5%.

TABLE 6. COMPARISON OF CR_{ah}

μ =	λ = 0.1 Isida	0.1 This Study	0.1 Dev %	0.3 Isida	0.3 This Study	0.3 Dev %	0.5 Isida	0.5 This Study	0.5 Dev %	0.7 Isida	0.7 This Study	0.7 Dev %
0.10	1.003	1.006	0.30	1.007	1.007	0.00	1.016	1.016	0.00	1.053	1.049	-0.38
0.15	1.012	1.014	0.20	1.022	1.021	-0.10	1.042	1.041	-0.09	1.142	1.144	0.17
0.20	1.024	1.026	0.20	1.039	1.040	0.10	1.082	1.083	0.09	1.308	1.338	2.29
0.25	1.042	1.044	0.19	1.068	1.070	0.19	1.147	1.153	0.52	1.644	1.695	3.10
0.30	1.066	1.068	0.19	1.110	1.111	0.09	1.246	1.259	1.04			
0.35	1.096	1.100	0.36	1.164	1.170	0.51	1.395	1.416	1.50			
0.40	1.144	1.143	0.08	1.238	1.249	0.89	1.640	1.638	0.12			
0.45	1.196	1.198	0.17	1.338	1.354	1.20	2.046	1.943	5.03			
0.50	1.265	1.269	0.32	1.480	1.468	-0.81						
0.55	1.348	1.357	0.67	1.658	1.720	3.73						
0.60	1.454	1.466	0.82	1.950	1.885	-3.33						
0.65	1.590	1.600	0.63									
0.70	1.760	1.762	0.11									
0.75	1.960	1.956	-0.20									

3.1.17 The Finite Width Effect For An Edge Crack

The finite width corrections for an edge crack, shown in Figures 33 and 34, are available from Ref. 20 (Pages 2.11 and 2.27). For the case of remote stress, the correction factor is given as,

$$CR_{fweg} = \frac{K}{\sigma\sqrt{\pi a}} = \sqrt{\frac{2b}{\pi a}\tan\frac{\pi a}{2b}}\;\frac{0.752 + 2.02\left(\frac{a}{b}\right) + 0.37\left(1 - \sin\frac{\pi a}{2b}\right)^3}{\cos\frac{\pi a}{2b}} \tag{70}$$

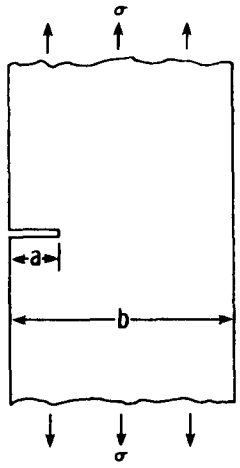

Figure 33. An Edge Crack In A Finite Plate - Remote Stress

For the case of fastener load, the correction factor is given as,

$$CP_{fweg} = \frac{K}{\frac{P}{\sqrt{\pi a}}} = 2\left\{\frac{3.52\cdot\left(1-\frac{c}{a}\right)}{\left(1-\frac{a}{b}\right)^{1.5}} - \frac{4.35 - 5.28\frac{c}{a}}{\left(1-\frac{a}{b}\right)^{0.5}} + \left[\frac{1.30 - 0.3\left(\frac{c}{a}\right)^{1.5}}{\sqrt{1-\left(\frac{c}{a}\right)^2}} + 0.83 - 1.76\frac{c}{a}\right]\left[1-\left(1-\frac{c}{a}\right)\frac{a}{b}\right]\right\} \tag{71}$$

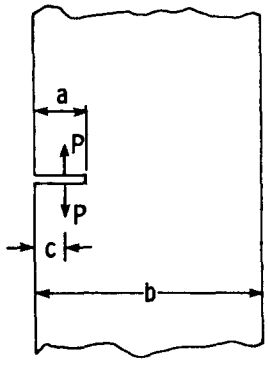

Figure 34. An Edge Crack In A Finite Plate - Fastener Load

3.1.18 An Edge Crack In A Semi-infinite Plate

The SIF for the crack shown in Figures 35-a and 35-b is available from Ref. 20. For the case of remote stress, the correction factor is given as,

$$CR_{sweg} = \frac{K}{\sigma\sqrt{\pi a}} = 1.1215 \tag{72}$$

For the case of fastener load, the correction factor is given as,

$$CP_{sweg} = \frac{K}{\frac{P}{\sqrt{\pi a}}} = \frac{2\left[1.3 - 0.3\left(\frac{c}{a}\right)^{1.5}\right]}{\sqrt{1-\left(\frac{c}{a}\right)^{2}}} \tag{73}$$

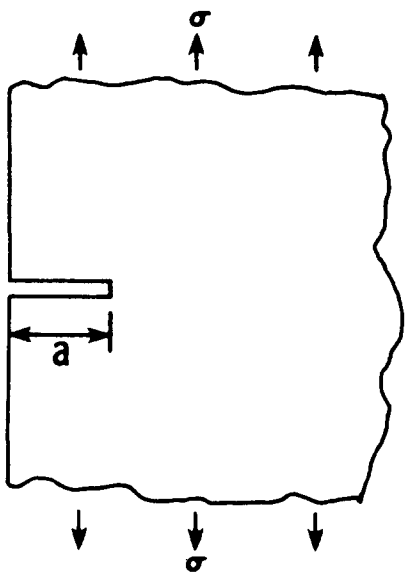

Figure 35-a. A Crack In A Semi-infinite Plate-Remote Stress

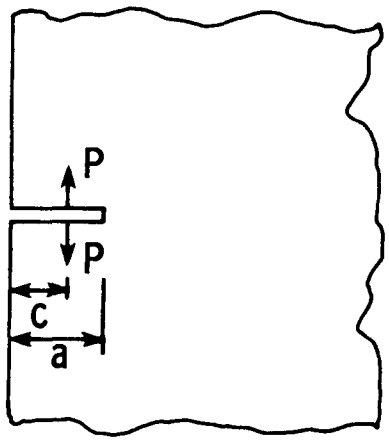

Figure 35-b. A Crack In A Semi-infinite Plate - Fastener Load

3.1.19 The Effect Of A Counter-Sink

The counter-sink will increase the stress concentration factor, k_{tg}, because there is less load-carrying area in a counter-sunk hole. The effect of a counter-sink on the stress concentration of a hole is usually estimated using engineering judgement coupled with simplified model representation. In this investigation, the three-dimensional (3-D) finite element method (FEM) was used to analyze the effect of a counter-sink on k_{tg} and SIF. The HEXA and HEX20 elements, which are 20-node isoparametric brick elements in the MSC/NASTRAN, were adopted for modeling.

Figure 36 shows the 3-D FEM results for a straight hole and a corresponding counter-sunk hole whose depth of counter-sink is 21% of the plate thickness. Only one quarter of the plate is modeled; the model consists of 1047 nodal points. Figure 36-a indicates that the k_{tg} value on the surface is the lowest, (2.806), and the k_{tg} value in the mid-thickness is highest, (3.338). There is a 16% difference in k_{tg} between the surface and the mid-thickness. This is one of the reasons that an embedded crack tends to initiate in the hole wall of relatively thick plate. Figure 36-b indicates that the k_{tg} value on the counter-sunk side surface is only 1.781 whereas the k_{tg} value on the other side of the plate is 2.731. The highest k_{tg} value occurs at z=0.64t which is near the point of intersection between the counter-sink and the drilled hole wall. The largest k_{tg} value in the counter-sunk hole, (3.562) is 7% higher than the largest k_{tg} value in the corresponding straight hole, (3.338).

The 3-D FEM analysis was also made for a straight hole and a corresponding counter-sunk hole whose depth of counter-sink is 32% of the plate thickness. The results are shown in Figure 37. The trend of the data is similar to that shown in Figure 36. However, the largest k_{tg} value for a counter-sunk hole, (3.628) is 8.4% higher than the largest k_{tg} value for a straight hole.

To facilitate the evaluation of the effect of a counter-sink on SIF, the averaged k_{tg} value through the thickness will be used. Based on the 3-D FEM results, the fraction of increase in the average k_{tg} values due to the presence of a counter-sink is approximated by the following equation.

$$G = 0.0021 \cdot csk \tag{74}$$

where CSK is the percentage of counter-sink depth relative to the plate thickness.

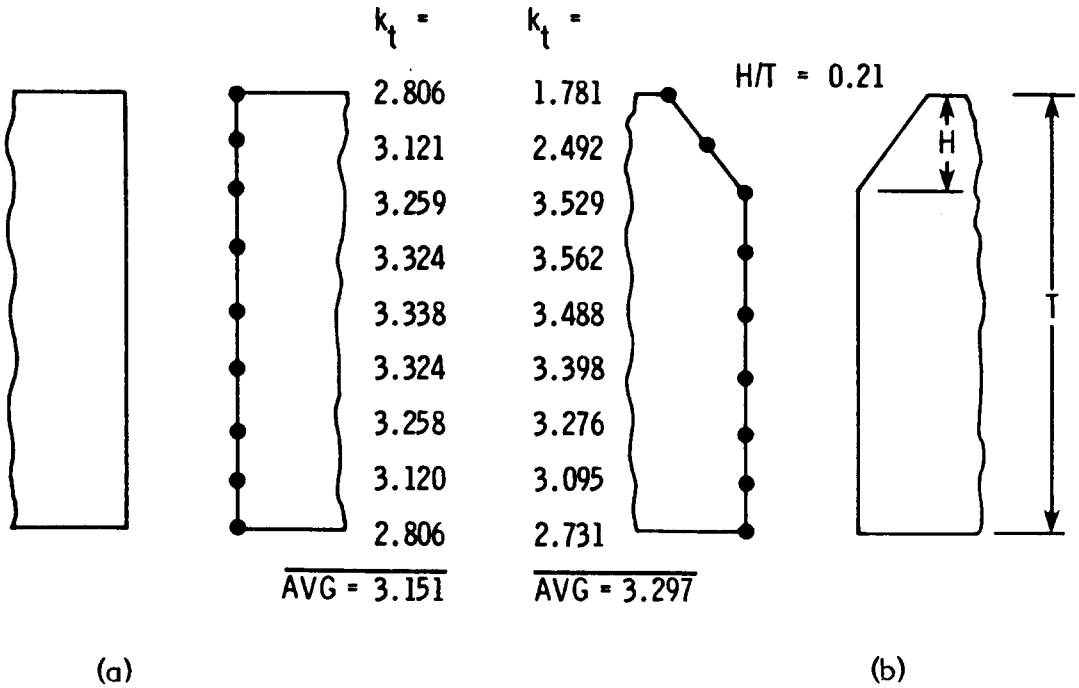

Figure 36. Comparison Of k_{tg} In Straight Hole And In A 21% Counter-sunk Hole

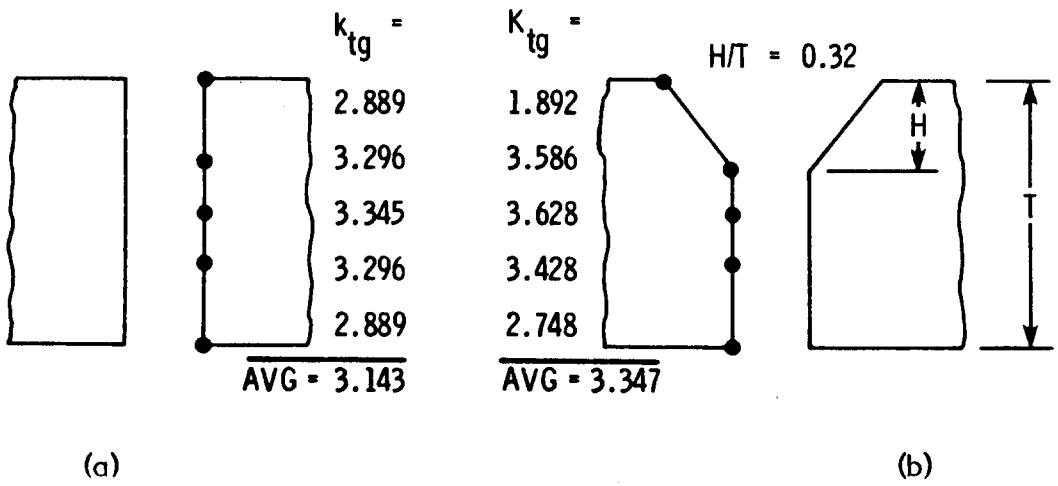

Figure 37. Comparison Of k_{tg} In Straight Hole And In A 32% Counter-sunk Hole

The 3-D FEM was also used to analyze the cracked counter-sunk holes whose depths of counter-sink are 21% and 32% of the plate thickness. The crack length equals about the hole radius. The HEX20 element, which is a true 20-noded isoparametric element in MSC/NASTRAN, was used for the elements immediately surrounding the crack tip. The 1/4 position technique due to Barsoum (Ref. 24) was used to impose the desired strain/stress singularity near a crack tip. The rest of the plate is modeled using the HEXA element which is a modified 20-noded isoparametric element.

The normalized SIF's from FEM analysis are shown in Table 7 for various locations through the plate thickness. The largest SIF occurs at the point of intersection between counter-sink and the drilled hole wall. This location coincides with the location of the largest k_{tg}.

TABLE 7. NORMALIZED SIF OF COUNTER-SUNK HOLE

Z=	21% Counter-sink	Z=	32% Counter-sink
0.3125	0.8758	0.3125	0.9091
0.2790	0.9250	0.2790	0.9467
0.2455	0.9732	0.2455	0.9862
0.2009	0.9696	0.2078	0.9813
0.1562	0.9629	0.1701	0.9754
0.1116	0.9636	0.1366	0.9263
0.0670	0.9614	0.1031	0.8797
0.0335	0.9091		
0.0	0.8564		
RMS	0.9339		0.9443

The normalized SIF for a straight hole having the same crack length is 0.926. The Root-Mean-Square (RMS) of the SIF's for the 21% and 32% counter-sunk holes are only 0.8% and 2% higher than that of a straight hole, respectively. The largest SIF for the 21% and 32% counter-sunk hole are 5.1% and 6.5% higher than the SIF of a straight hole, respectively. The largest k_{tg} for the 21% and 32% counter-sunk holes are 6.7% and 8.5% higher than the largest k_{tg} of a straight hole, respectively. However, the averaged k_{tg} for the 21% and 32% counter-sunk holes are 4.6% and 6.5% higher than the averaged k_{tg} of a straight hole, respectively. It seems that the largest SIF values can be correlated with the averaged k_{tg} value.

Therefore it is proposed to increase the SIF with the same percentage increase of the average k_{tg} due to the presence of a counter-sink. This is incorporated into the following correction factor using Equation (74).

$$CR_{csk} = \frac{K}{\sigma\sqrt{\pi a} \cdot CR_{ho1}} = 1 + 0.0021 \cdot csk, \qquad \text{for } a \leq R \tag{75}$$

Since this FEM analysis is performed for the crack length equal to about one hole radius, Equation (75) would be applicable for $a \leq R$. For $a > R$, the effect of counter-sink can be neglected. It is noted that the effect of a counter-sink on the SIF will be more substantial for small cracks.

3.1.20 The Stiffening Effect Of A Central Stringer

The stiffening effect of a central stringer, shown in Figure 38, was solved by Sanders (Ref. 25). His numerical data points were curve-fitted into the following expression in this investigation. The E and E_{st} are the Young's modulis for the skin and stringer, respectively. The A is cross section area of the stringer. The "t" is the skin thickness.

$$CR_{stf} = \frac{K}{\sigma\sqrt{\pi a}} = 0.63776 + 0.07559\,\lambda - 0.04081\,\lambda^2 + 0.01058\,\lambda^3 \tag{76a}$$

$$\lambda = \frac{2at\,E}{A\,E_{st}} \tag{76b}$$

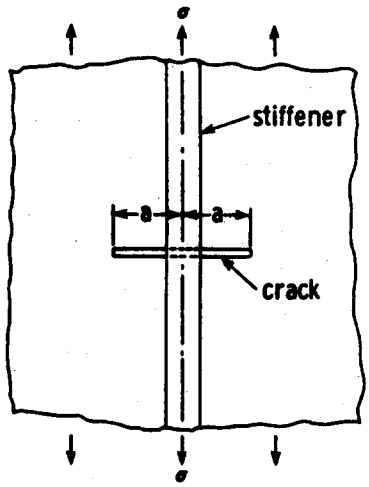

Figure 38. A Cracked Sheet With A Central Stringer

3.1.21 The Stiffening Effect Due To Non-similar Material

Isida (Ref. 23) has solved the stiffening effect for the configuration shown in Figure 39. He presented his results graphically. In this investigation, the graph was enlarged to an appropriate size to facilitate reading the numerical values up to two digits after the decimal point. The numerical values were then curve-fitted into the following expression.

$$CR_{sf} = \frac{K}{\sigma\sqrt{\pi a}} = C1 + C2 \cdot \lambda + C3 \cdot \lambda^2 \tag{77a}$$

$$C1 = 1.00753 - 0.01088\,\beta + 0.00218\,\beta^2 - 0.00013\,\beta^3 \tag{77b}$$

$$C2 = -0.24814 + 0.33864\,\beta - 0.10613\,\beta^2 + 0.01388\,\beta^3 - 0.00062\,\beta^4 \tag{77c}$$

$$C3 = 0.57494 - 0.77771\,\beta + 0.23633\,\beta^2 - 0.03146\,\beta^3 + 0.00145\,\beta^4 \tag{77d}$$

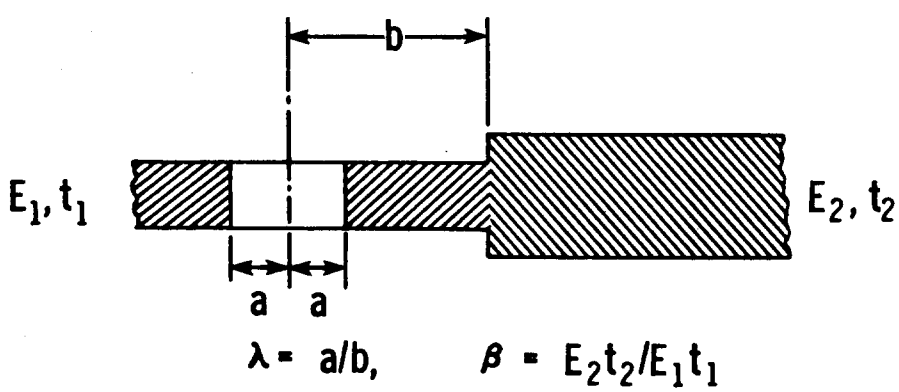

Figure 39. The Stiffening Effect Due To Non-similar Material

3.2 Stress Intensity Factors for Typical Airframe Structures

The compounded solution method is being used to formulate the stress intensity factors for the Task IV structural test specimens which are representative of common airframe design. Two types of specimens are used in Task IV Structural Tests, namely, stringer-reinforced specimens and lap-joint specimens. The stringer-reinforced specimens are intended to simulate spar-to-skin attachments. The lap-joint specimens are intended to simulate chordwise lap-joints.

Figures 40 through 45 show the schematic diagrams of the structural test specimens. The stress intensity factors for each member in a specimen assembly are formulated for the anticipated cracking sequence according to MIL-A-83444 and the combined crack growth and initiation method for life prediction. For all types of stringer-reinforced specimens, the load redistribution accompanying crack growth can be neglected in accordance with the observation made in Refs. 3, 4, and 5. However, the load redistribution (due to crack growth) among fasteners in the chordwise lap-joint specimens will be considered to achieve accurate life predictions.

3.2.1 Skins of Stringer-reinforced Specimens

The fastener load induced by the load redistribution during crack growth need not be considered in accordance with the observation made in Refs. 3, 4, and 5. Therefore, only remote stress is considered in the formulation of the SIF for skins. Figures 46 through 59 show the anticipated cracking sequence and the SIF associated with each configuration. The anticipated cracking sequence with the consideration of crack initiation is merely to illustrate the formulation of the SIF; the actual cracking sequence shall be predicted from crack growth and initiation analyses.

3.2.2 Tee-Stringer

Figures 60-a through 60-e show various configurations where a crack does not extend into the upright leg of a tee-stringer. In such cases, the tee-stringer can be modeled in the way shown in Figure 61 for the compounded solution method. The stiffening effect due to the upright leg can be accounted for using Isida's solution (Ref. 23) given in Equations (77a) through Equations (77d). The normalized SIF calculated in this manner is shown in Table 9. The 3-D FEM analyses were performed to validate the modeling technique shown in Figure 61.

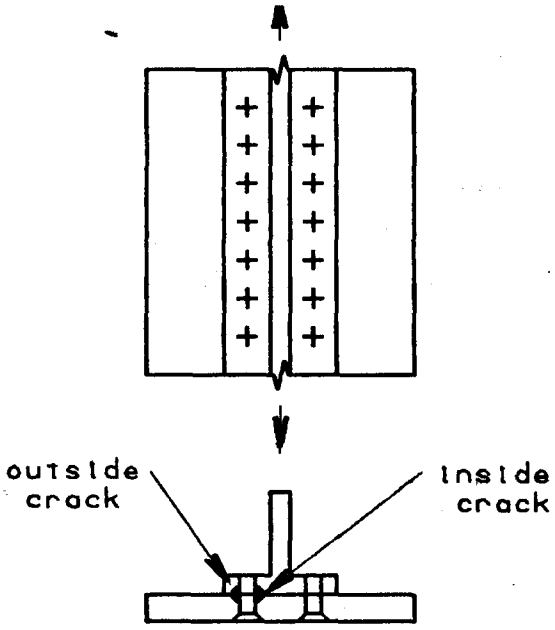

Figure 40. Central Tee-Stringer Continuous Skin Specimen

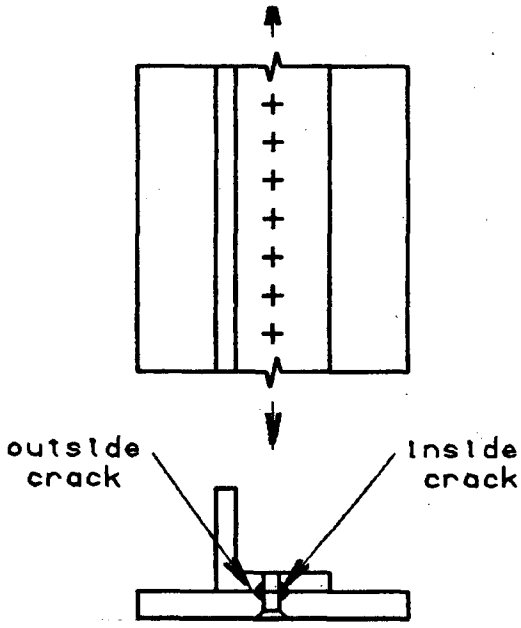

Figure 41. Central Angle-Stringer Continuous Skin Specimen

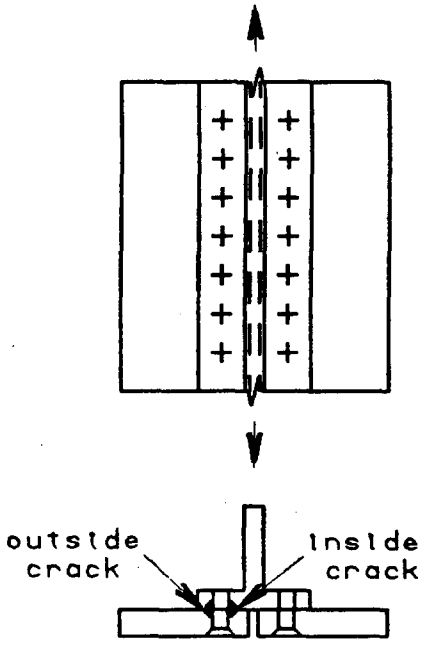

Figure 42. Central Tee-Stringer Split Skin Specimen

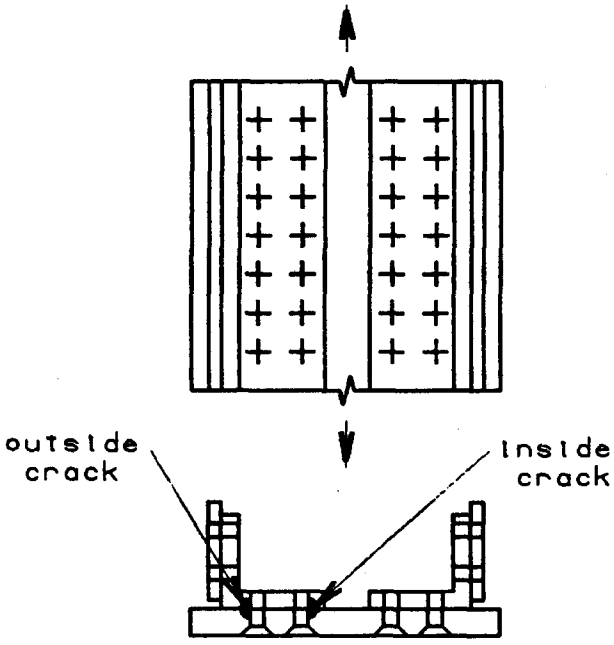

Figure 43. Edge-Stringer Continuous Skin Specimen

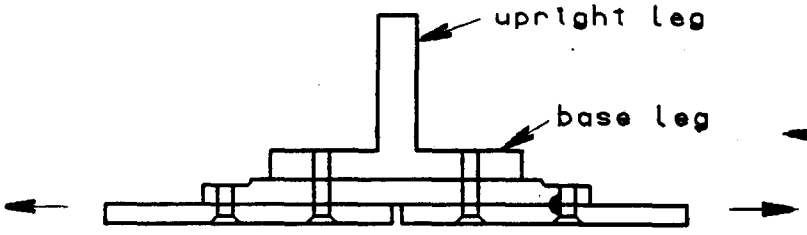

Figure 44. Single-shear Lap-joint Specimen

Figure 45. Double-shear Lap-joint Specimen

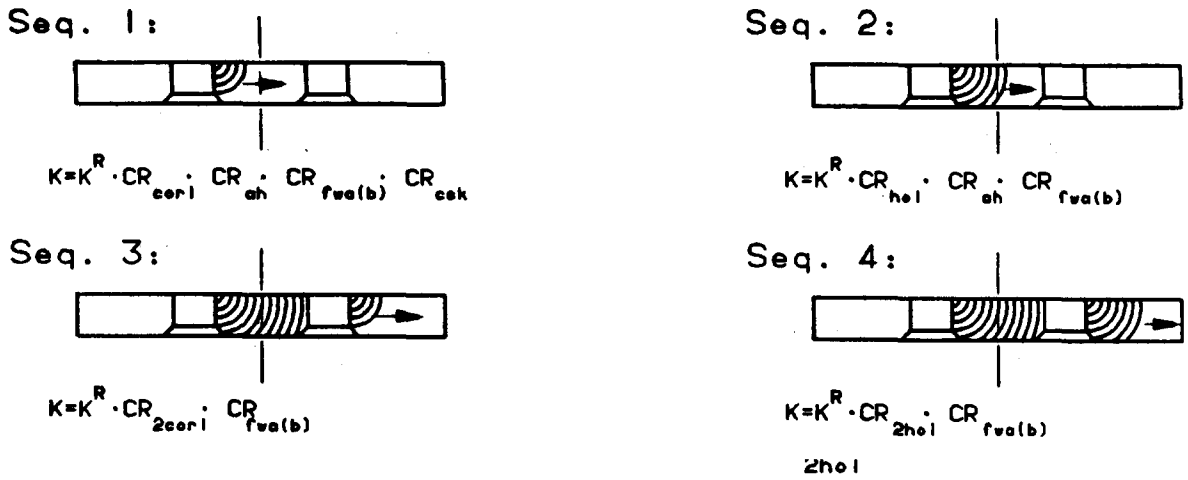

Figure 46. Cracking Sequence and Associated SIF for the Inside Initial Crack in the Skin of Figure 40 - Without Crack Initiation

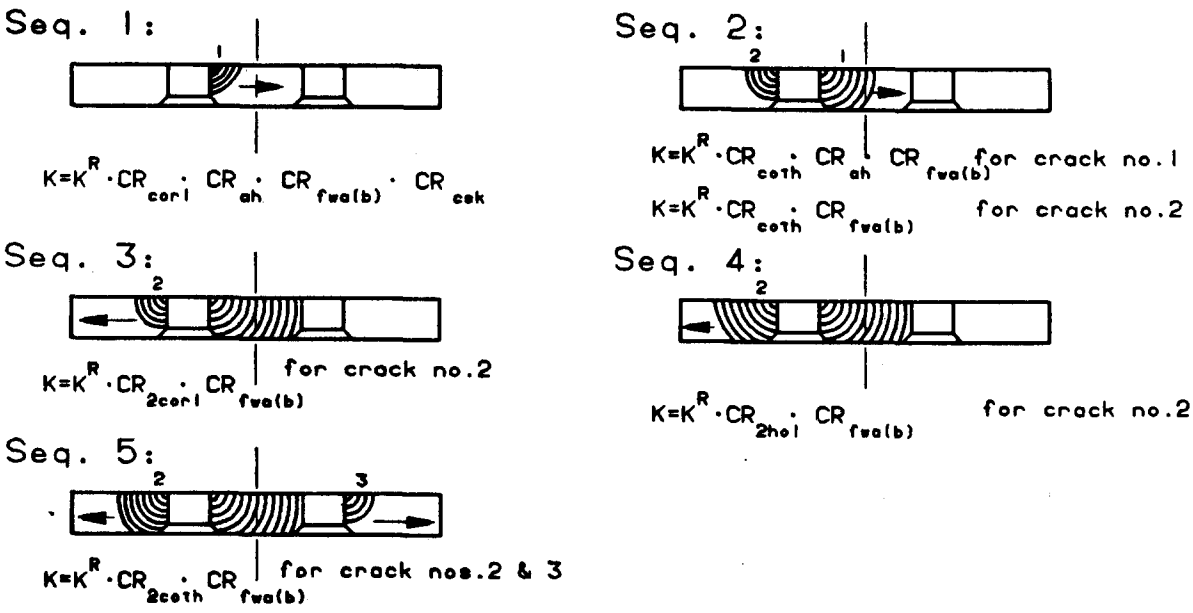

Figure 47. Cracking Sequence and Associated SIF for the Inside Initial Crack in the Skin of Figure 40 - With Crack Initiation

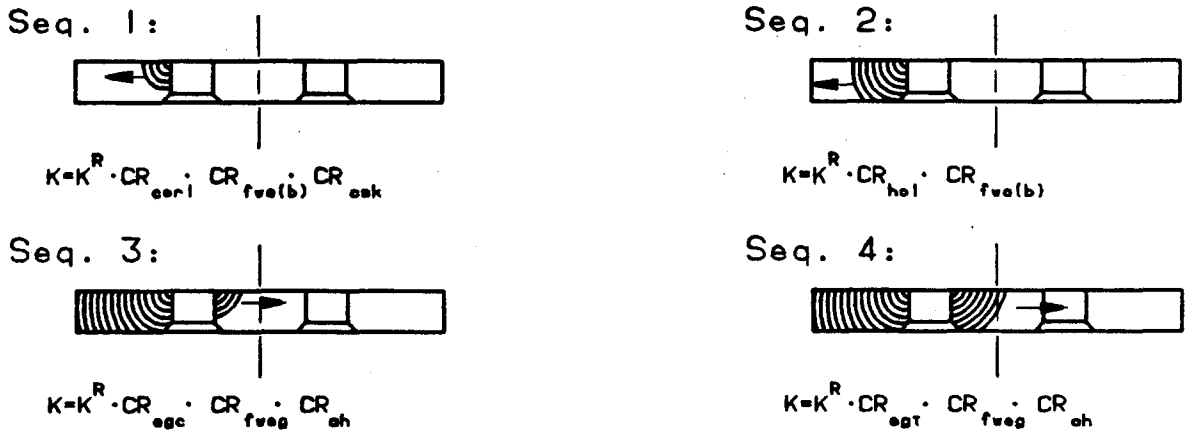

Figure 48. Cracking Sequence and Associated SIF
for the Outside Initial Crack in the Skin
of Figure 40 - Without Crack Initiation

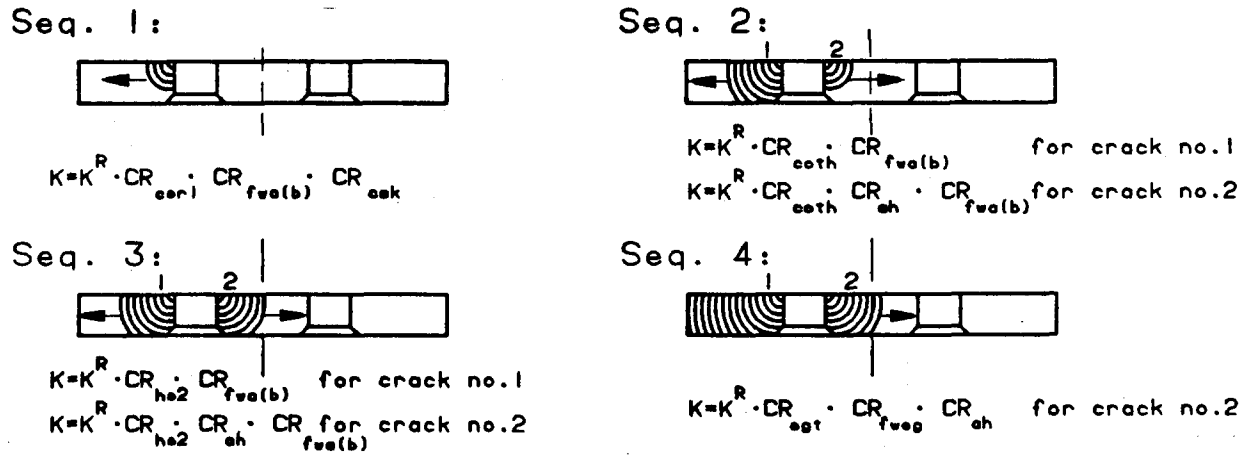

Figure 49. Cracking Sequence and Associated SIF
for the Outside Initial Crack in the Skin
of Figure 40 - With Crack Initiation

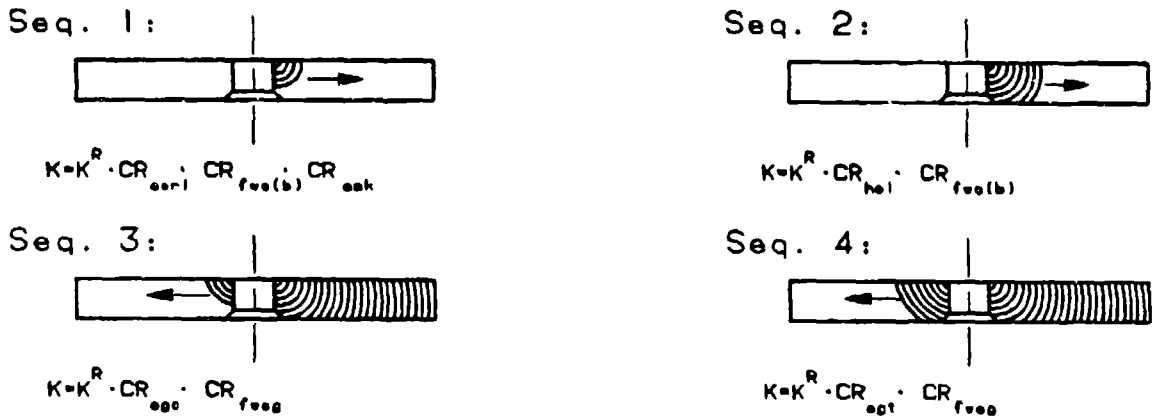

Figure 50. Cracking Sequence and Associated SIF for the Skin of Figure 41 - Without Crack Initiaion

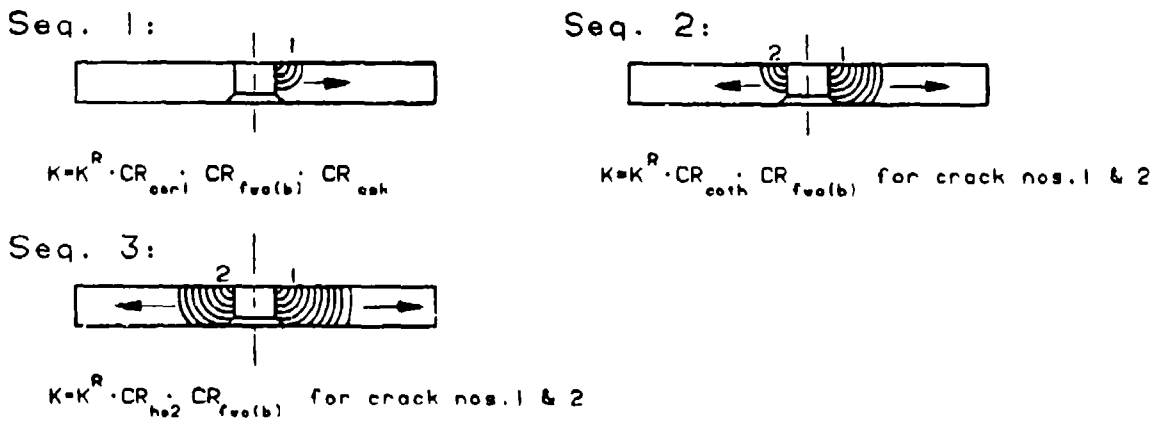

Figure 51. Cracking Sequence and Associated SIF for the Skin of Figure 41 - With Crack Initiation

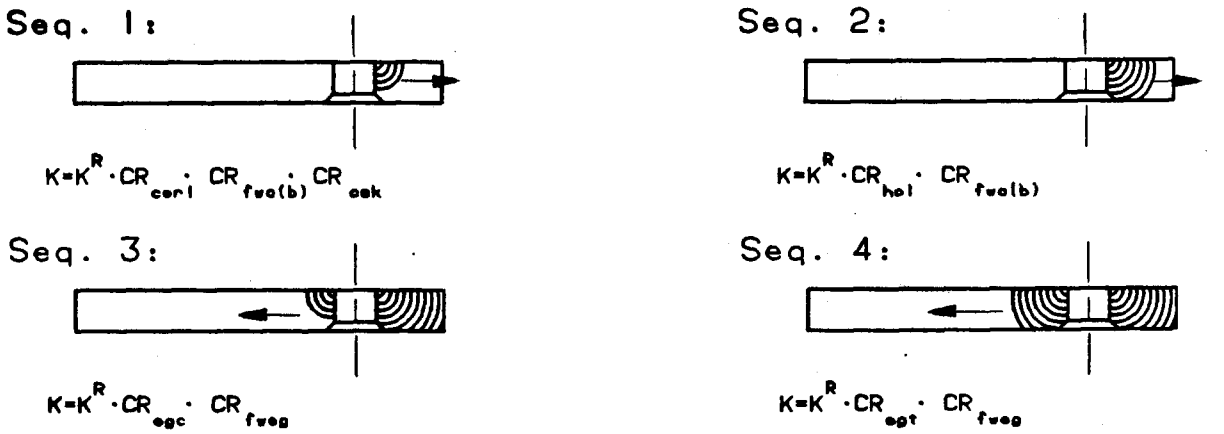

Figure 52. Cracking Sequence and Associated SIF
for the Inside Initial Crack in the Skin
of Figure 42 - Without Crack Initiation

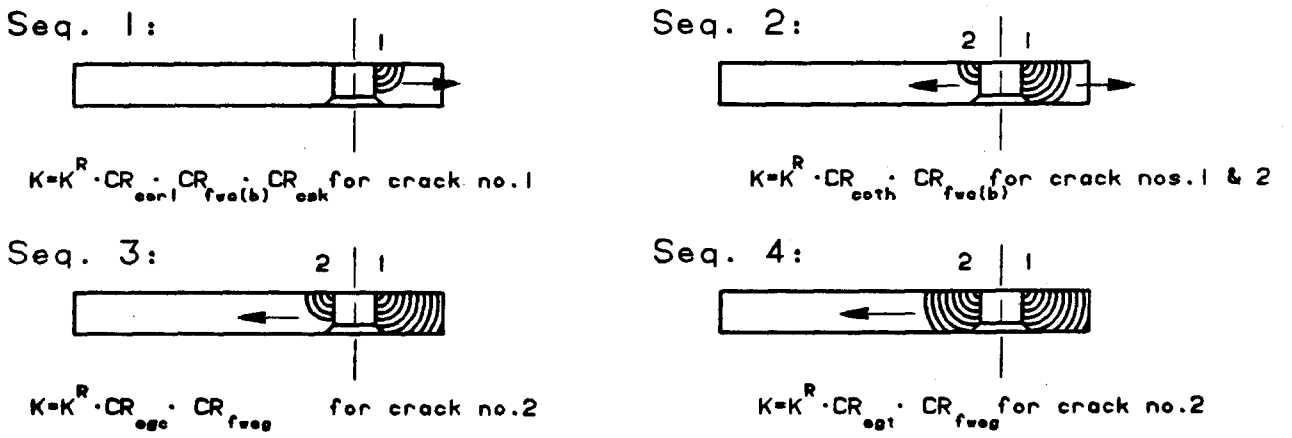

Figure 53. Cracking Sequence and Associated SIF
for the Inside Initial Crack in the Skin
of Figure 42 - With Crack Initiation

Figure 54. Cracking Sequence and Associated SIF
for the Outside Initial Crack in the Skin
of Figure 42 - Without Crack Initiation

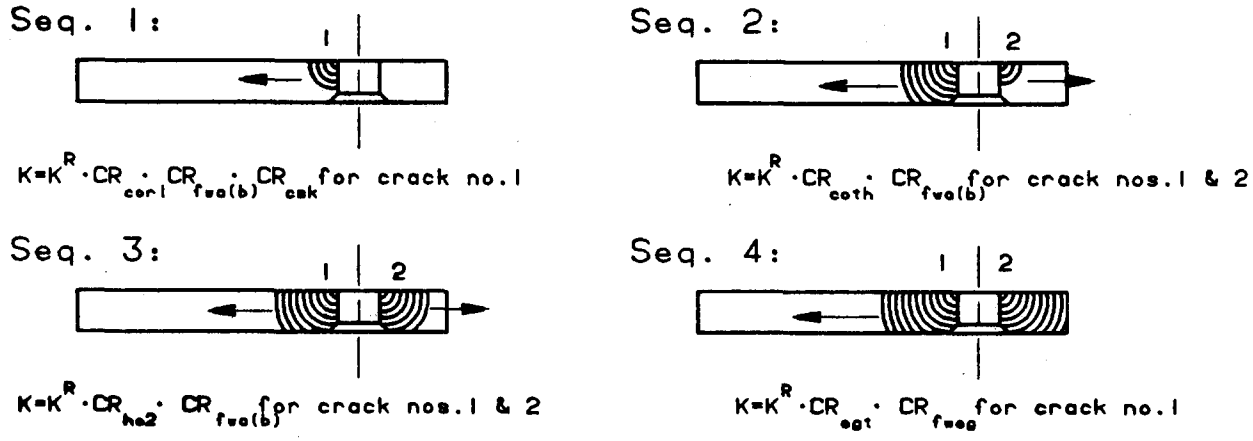

Figure 55. Cracking Sequence and Associated SIF
for the Outside Initial Crack in the Skin
of Figure 42 - With Crack Initiation

Figure 56. Cracking Sequence and Associated SIF
for the Inside Initial Crack in the Skin
of Figure 43 - Without Crack Initiation

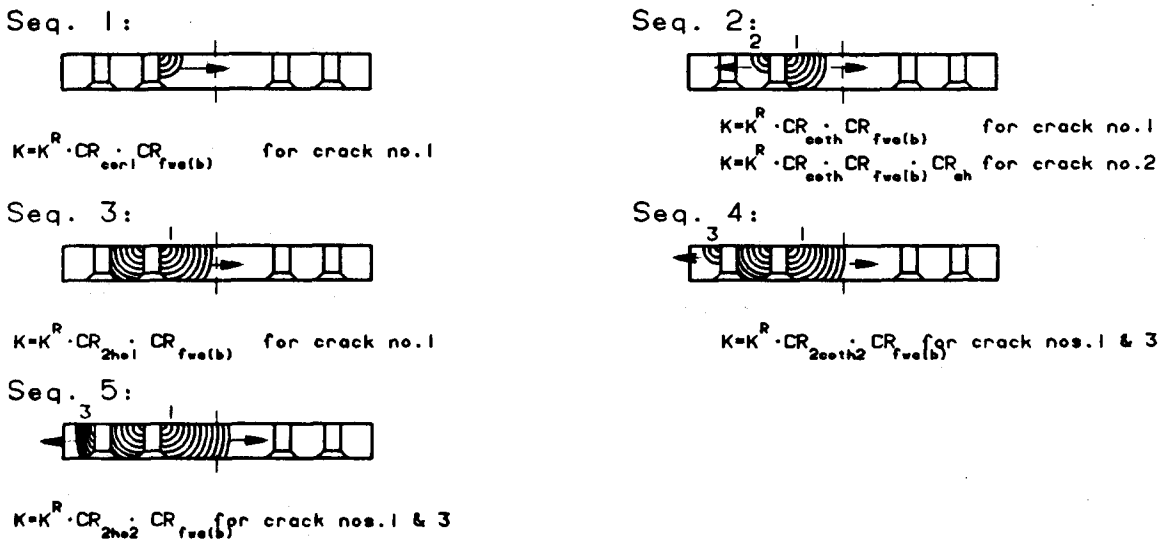

Figure 57. Cracking Sequence and Associated SIF
for the Inside Initial Crack in the Skin
of Figure 43 - With Crack Initiation

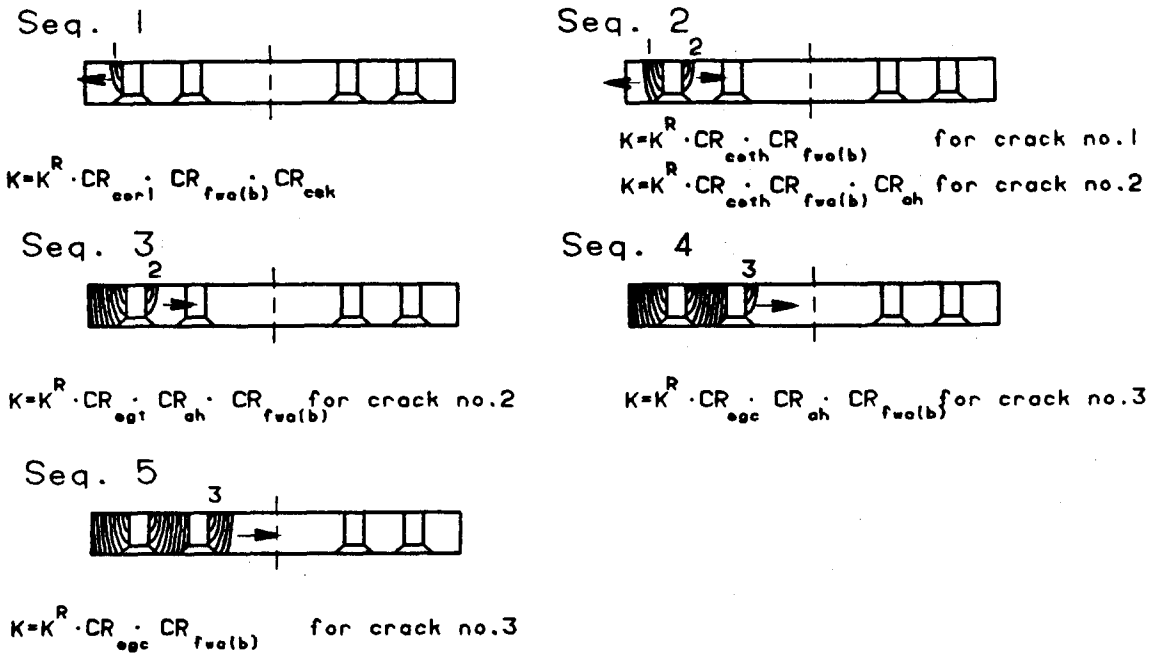

Figure 58. Cracking Sequence and Associated SIF for the Outside Initial Crack in the Skin of Figure 43 - Without Crack Initiation

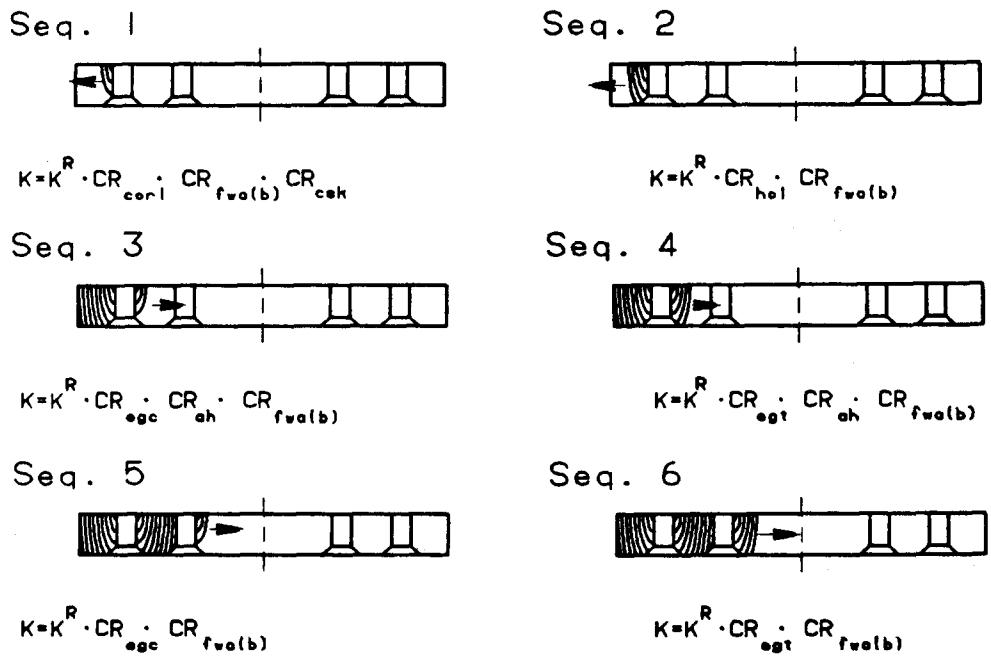

Figure 59. Cracking Sequence and Associated SIF for the Outside Initial Crack in the Skin of Figure 43 - With Crack Initiation

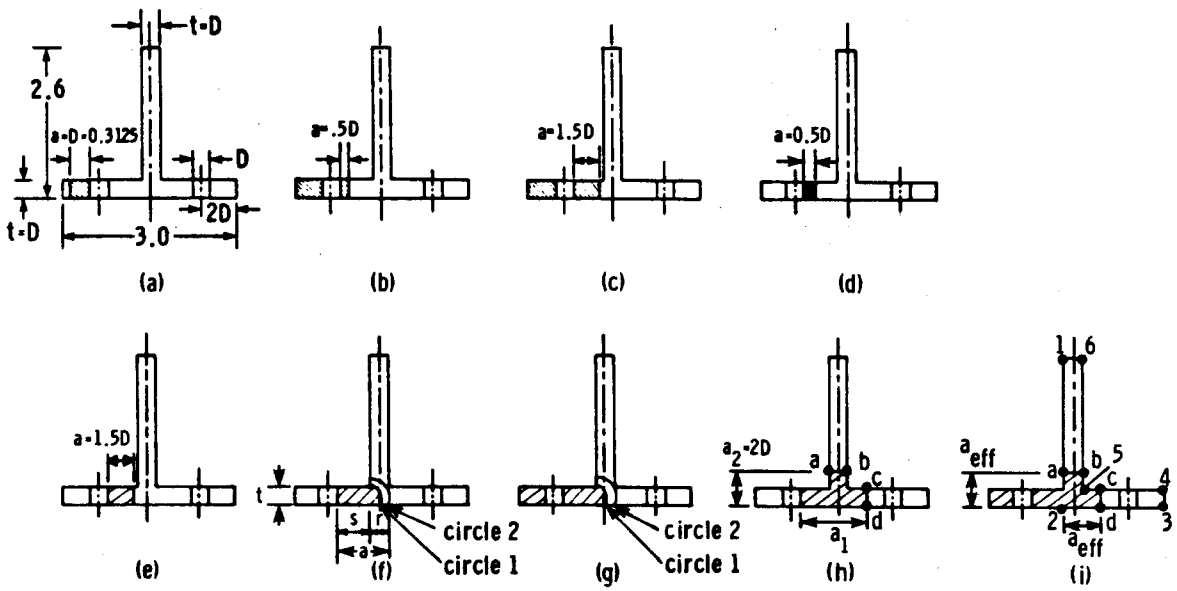

Figure 60. Cracked Tee-Stringers

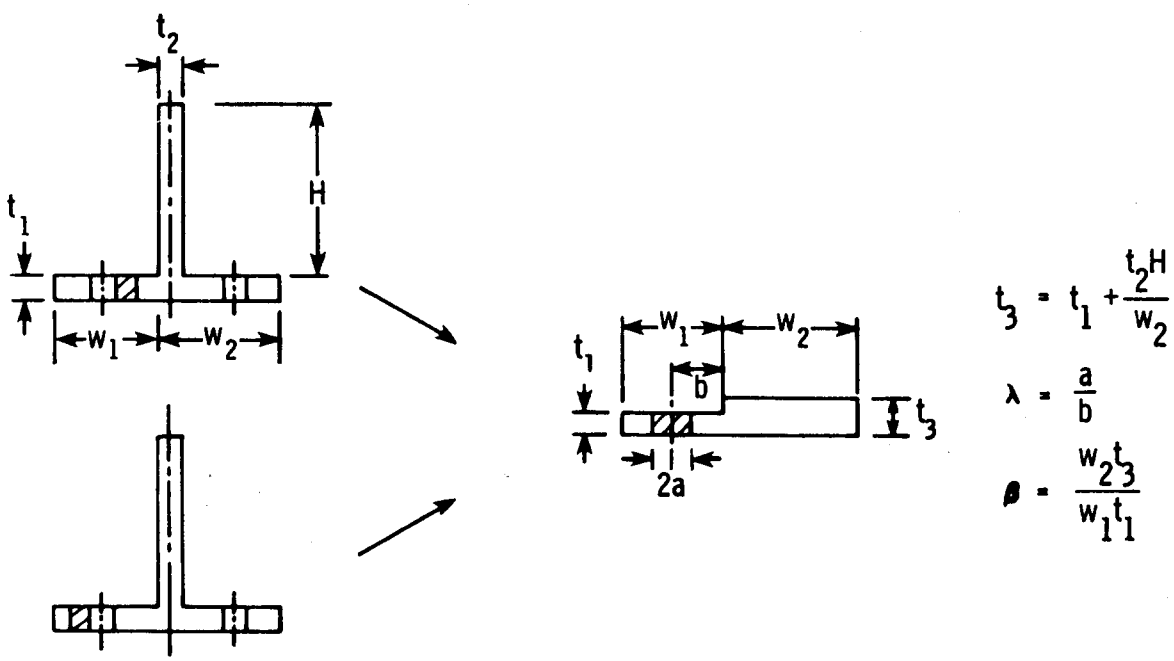

Figure 61. Tee-Stringer Models for Compounded Solution Method

TABLE 8. NORMALIZED SIF FOR TEE-STRINGER

Location for FEM Results	Fig. 60-a	Fig. 60-b	Fig. 60-c	Fig. 60-d	Fig. 60-e	Fig. 60-h Protruding Leg**	Fig. 60-h Base Leg**	Fig. 60-i Protruding Leg**	Fig. 60-i Base Leg**
Z = 0.3125	1.252	2.432	3.412	0.855	1.136	1.393	1.398	3.135	2.170
Z = 0.2344	1.299	2.611	3.547	0.922	1.177	1.563	1.140	4.454	4.182
Z = 0.1562	1.327	2.637	3.646	0.942	1.223	1.681	1.828	5.536	4.965
Z = 0.0781	1.299	2.552	3.442	0.921	1.182	1.705	1.911	6.273	5.428
Z = 0.0	1.327	2.313	3.166	0.851	1.136	1.682	1.949	6.807	5.696
RMS*	1.301	2.512	3.446	0.899	1.171	1.609	1.757	5.404	4.777
Compounded Solution	1.352	2.710	3.844	0.936	1.073	*1.469	*1.515	*5.440	*4.880

*RMS = Root-Mean-Square

**The z-locations of the normalized SIF are different than the ones shown in the Table.

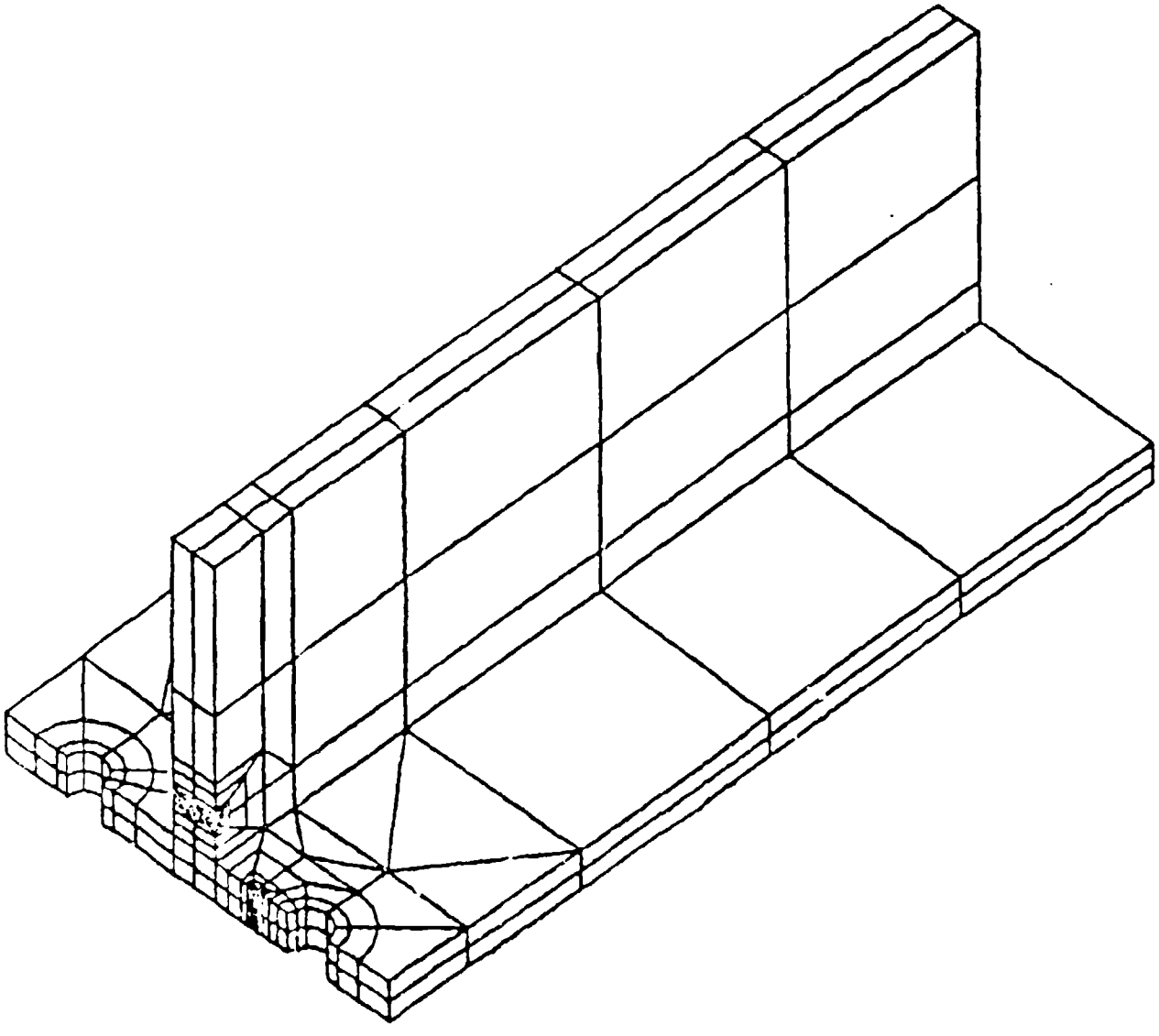

Figure 62. FEM Model for the Tee-Stringer shown in Figure 60-i

The PENTA, HEXA, and HEX20 elements in the MSC/NASTRAN were used in the analyses. Figure 62 shows an example of the finite element meshes. Only two layers of elements were used in the thickness direction. Since the main purpose is to evaluate the load transfer between the base and upright legs of a tee-stringer rather than the stress distribution along the thickness direction, such a modeling technique is expected to give a reasonably good representation of load-transfer. The normalized SIF corresponding to Figures 60-a through 60-e are shown in Table 8 for comparison.

Table 8 indicates that the compounded solution method, in conjunction with the model shown in Figure 61, gave slightly higher SIF values compared to the 3-D FEM results. The largest deviation is about 14% for the longest crack length, (Figure 56-b) where the SIF is high and there is not much life left. Such an accuracy of the compounded solution method is probably acceptable for practical applications.

When an outside crack, e.g. Figure 60-g, grows into the junction area between the upright leg and the base leg of a tee-stringer, the normalized SIF is so large such that the crack virtually grows in a somewhat unstable manner. However, the configuration shown in Figure 60-f, where an inside crack grows into the junction area, is an important one. In both cases, the method due to Brussat et al (Ref. 3) is being adopted and rewritten in the following expression.

$$CR_{sfj} = \sqrt{\frac{st + 0.25 \cdot \pi \cdot r^2}{a \cdot 0.25 \cdot \pi \cdot (2r)}} \tag{78}$$

where a, t, r, and s are shown in Figure 60-f. Equation (78) will be applicable until the crack front reaches circle No. 2 shown in Figures 60-f and 60-g. After this point, the configurations can be treated as having two cracks shown in Figures 60-h and 60-i.

When a crack grows into the protruding leg of a tee-stringer as shown in Figures 60-h and 60-l, the load eccentricity will induce additional bending stress which needs to be considered in the analysis. The bending stress, f_b, at locations a, b, c, and d in Figure 60-h can be calculated with Equation (79) given in pages 156-157 of Ref. 26. The coordinates

$$f_b = \frac{M_x I_{xy} - M_y I_x}{I_x I_y - I_{xy}^2} x + \frac{M_y I_{xy} - M_x I_y}{I_x I_y - I_{xy}^2} y \tag{79}$$

are located at the centroid of the cross section of intact tee-stringer. The moments M_x and M_y are calculated from the stress in the fractured area. The I_x, I_y, and I_{xy} are moments of inertia. The x and y are the coordinates of locations a, b, c, and d, respectively. A correction factor, CR_b, as defined below is included in the SIF.

$$CR_b = 1 + \frac{f_b}{\sigma_o} \tag{80}$$

For the branch of the crack in the base leg of a tee-stringer shown in Figure 60- h, the upright leg is treated as a middle stiffener across a crack. The ancillary solution CR_{stf} given in Equations (76a) and (76b) can be applied to this situation. The effective cross sectional area of the stiffener shall be only the uncracked ligment of the upright leg. Thus, the SIF is given as;

$$K = \sigma \sqrt{\pi a} \cdot CR_{ho1} \cdot CR_{fwa(b)} \cdot CR_{ah} \cdot CR_{stf} \cdot CR_b \tag{81}$$

The root-mean-square of the SIF's calculated from Equation (81) for locations c and d of Figure 60-h is shown in Table 9 to compare with the FEM result. The root-mean-square of the SIF calculated from Equation (81), (1.515) is about 13.8% lower than that from the FEM.

For the branch of the crack in the upright leg of a tee-stringer, shown in Figure 60-h, the base leg is treated as a middle stiffener across the crack. The effective cross sectional area of the stiffener shall be only the uncracked ligment of the base leg. To account for the finite width effect, the crack is treated as an edge crack in a finite plate. Thus, the SIF is given as

$$K = \sigma \sqrt{\pi a} \cdot CR_{fweg} \cdot CR_{stf} \cdot CR_b \tag{82}$$

The root-mean-square of the SIF's calculated according to Equation (82), for locations a and b of Figure 60-h, is shown in Table 8 to compare with the FEM result. The root-mean-square of the calculated SIF's is 1.469 which is about 8.7% lower than that of the FEM result. However, the crack growth rate at this stage is very high so that it will not affect the accuracy of the crack growth life prediction.

To calculate bending stresses at locations a, b, c, and d in Figure 60-i, the moments of inertia and centroid shall be calculated using the area bounded by the six corners 1, 2, 3, 4, 5, and 6, which form an angle shape. However, the stress which contributes to the bending moments M_x and M_y, shall be from the entire fractured area. The two branches of the crack are treated as an edge crack in a finite plate. The stiffening effect due to the other leg can be neglected. The effective crack lengths for the two branches are shown in Figure 60-i. Thus, the SIF is given as

$$K = \sigma \sqrt{\pi a_{eff}} \cdot CR_{fweg} \cdot CR_b \cdot CR_{ah} \qquad \textbf{(for base leg)} \qquad (83a)$$

$$K = \sigma \sqrt{\pi a_{eff}} \cdot CR_{fweg} \cdot CR_b \qquad \textbf{(for upright leg)} \qquad (83b)$$

The root-mean-square of the SIF's calculated according to Equations (83a) and (83b) are shown in Table 8. It appears that the root-mean-square values for the SIF calculated with the compounded solution method agree quite well with the root-mean-square values from the FEM results. However, the crack growth rate at this stage is very high so that the accuracy will not significantly affect the crack growth life predictions.

In summary, the SIF's for the cracked tee-stringer configurations pertinent to life predictions are given in Figures 63 through 66.

3.2.3 Angle-Stringer

Figures 67-a through 67-d show various configurations where a crack does not extend into the upright leg of an angle-stringer. In such cases, two models for the compounded solution method were used for each configuration to obtain the SIF as shown in Table 10. The 3-D FEM analyses were performed to validate the solutions obtained from the compounded solution method. The first model has an effective width equal to that of the base leg of an angle-stringer. The stiffening effect due to the upright leg can be accounted for by using Equations (77a) through (77d). However, such a stiffening effect turns out to be small.

Seq. 1:

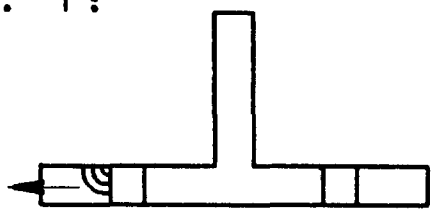

$K=K^R \cdot CR_{cori} \cdot CR_{fwa(b)} \cdot CR_{sf}$

Seq. 2:

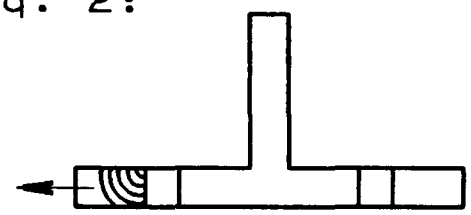

$K=K^R \cdot CR_{hol} \cdot CR_{fwa(b)} \cdot CR_{sf}$

Seq. 3:

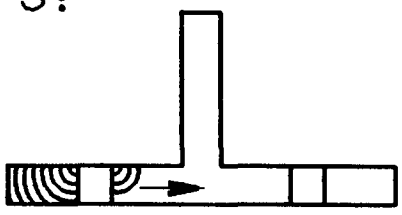

$K=K^R \cdot CR_{agc} \cdot CR_{fwag} \cdot CR_{sf}$

Seq. 4:

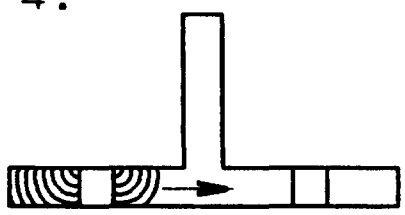

$K=K^R \cdot CR_{agt} \cdot CR_{fwag} \cdot CR_{sf}$

Seq. 5:

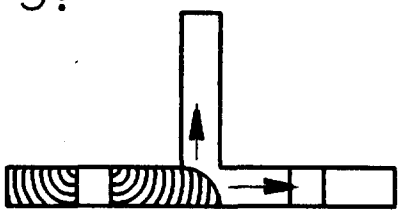

$K=K^R \cdot CR_{agt} \cdot CR_{fwag} \cdot CR_{sfj}$

Figure 63. Cracking Sequence and Associated SIF for the Outside Initial Crack in Tee-Stringer-Without Crack Initiation

Seq. 1:

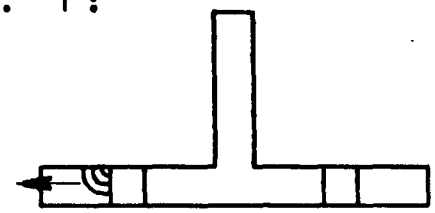

$K=K^R \cdot CR_{cori} \cdot CR_{fwa(b)} \cdot CR_{sf}$

Seq. 2:

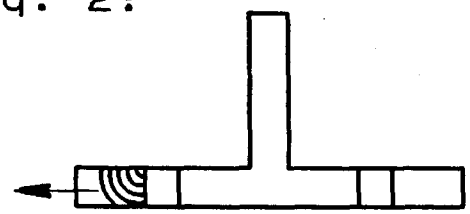

$K=K^R \cdot CR_{hol} \cdot CR_{fwa(b)} \cdot CR_{sf}$

Seq. 3:

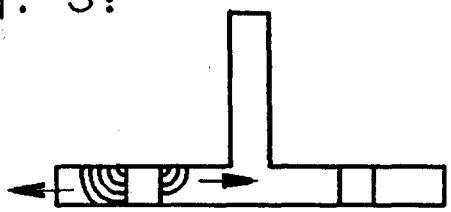

$K=K^R \cdot CR_{coth} \cdot CR_{fwa(b)} \cdot CR_{sf}$

Seq. 4:

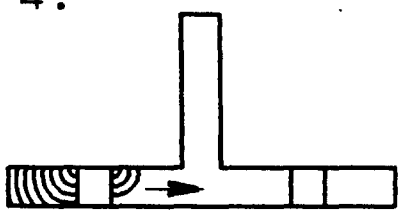

$K=K^R \cdot CR_{egc} \cdot CR_{fweg} \cdot CR_{sf}$

Seq. 5:

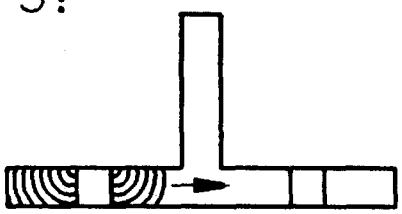

$K=K^R \cdot CR_{egt} \cdot CR_{fweg} \cdot CR_{sf}$

Seq. 6:

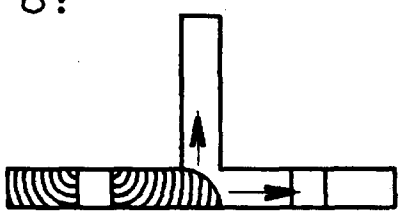

$K=K^R \cdot CR_{egt} \cdot CR_{fweg} \cdot CR_{sfj}$

Figure 64. Cracking Sequence and Associated SIF for the Outside Initial Crack in Tee Stringer - With Crack Initiation

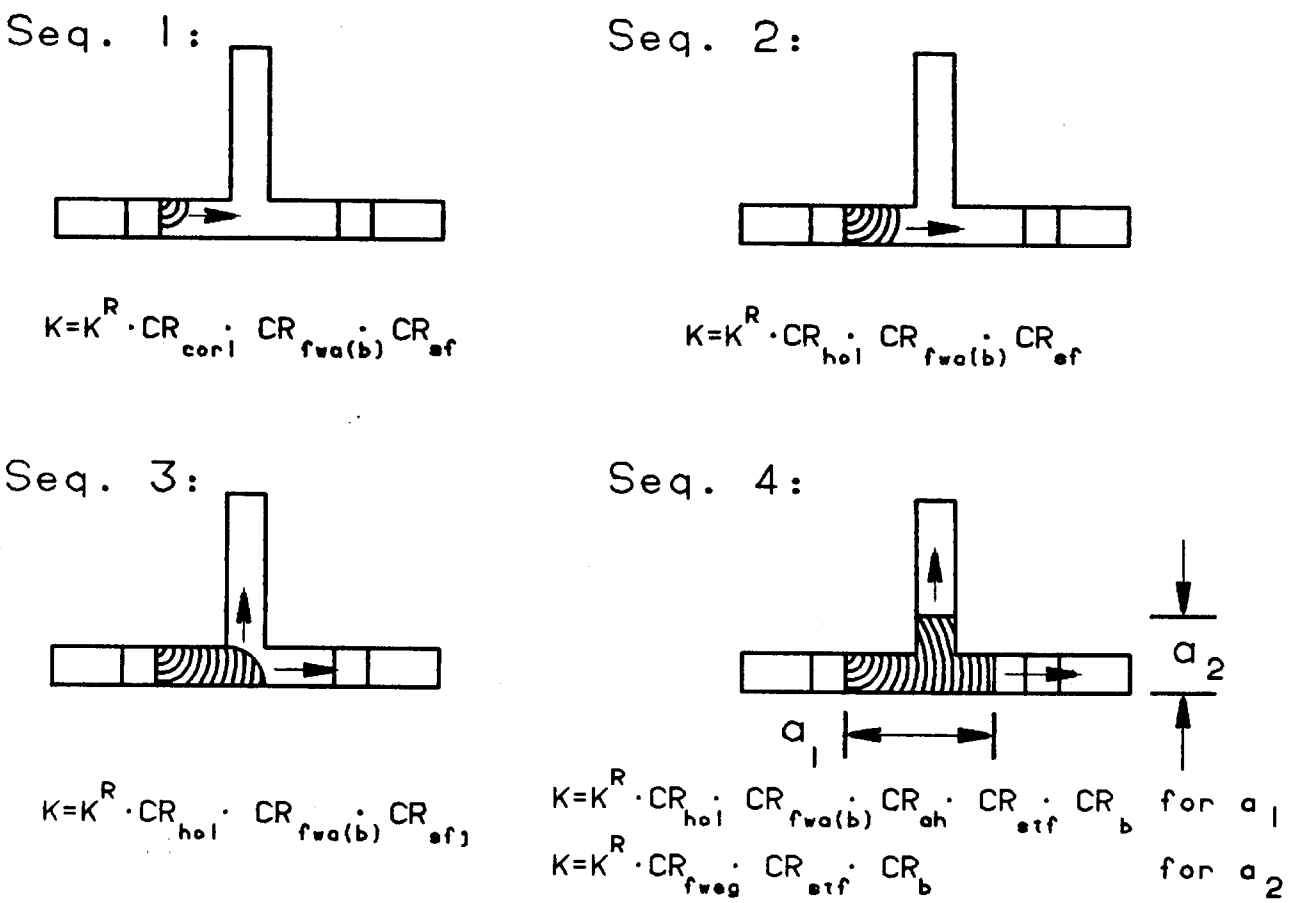

Figure 65. Cracking Sequence and Associated SIF for the Inside Initial Crack in Tee-Stringer - Without Crack Initiation

Seq. 1:

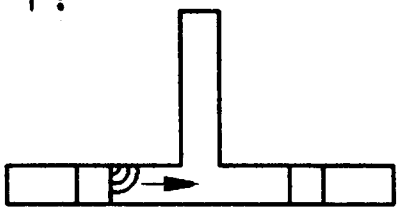

$K=K^R \cdot CR_{cor1} \cdot CR_{fwa(b)} \cdot CR_{sf}$

Seq. 2:

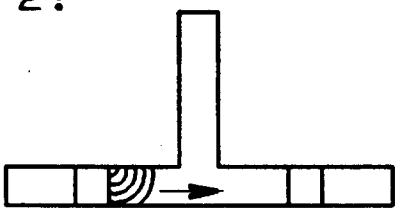

$K=K^R \cdot CR_{ho1} \cdot CR_{fwa(b)} \cdot CR_{sf}$

Seq. 3:

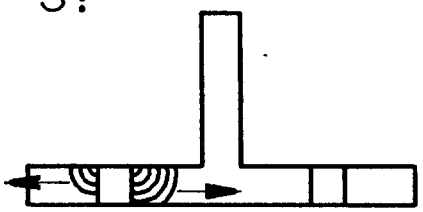

$K=K^R \cdot CR_{coth} \cdot CR_{fwa(b)} \cdot CR_{sf}$

Seq. 4:

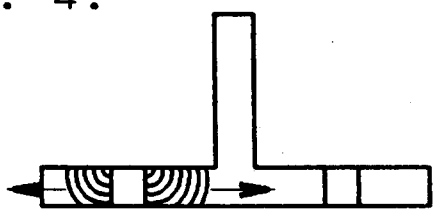

$K=K^R \cdot CR_{ho2} \cdot CR_{fwa(b)} \cdot CR_{sf}$

Seq. 5:

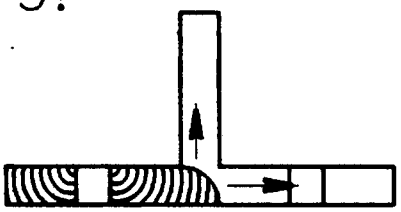

$K=K^R \cdot CR_{sgt} \cdot CR_{fwag} \cdot CR_{sfj}$

Figure 66. Cracking Sequence and Associated SIF
for the Inside Crack in Tee-Stringer - With Crack Initiation

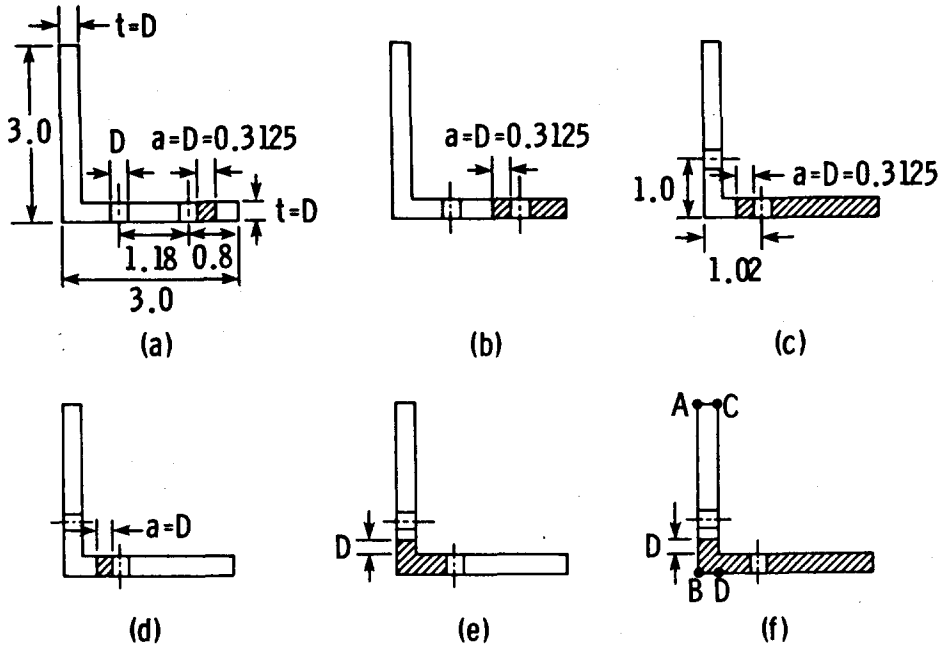

Figure 67. Cracked Angle-Stringer

TABLE 9. NORMALIZED SIF OF ANGLE-STRINGER

	Fig. 67-a	Fig. 67-b	Fig. 67-c	Fig. 67-d	Fig. 67-e	Fig. 67-f
Z=0.3125	1.150	4.151	27.439	1.068	2.181	55.068
Z=0.2344	1.183	4.329	27.892	1.089	2.400	33.244
Z=0.1562	1.236	4.482	27.684	1.126	2.617	13.900
Z=0.0781	1.181	4.210	24.671	1.064	2.589	0.0
Z=0.0	1.146	3.908	20.855	1.016	2.567	0.0
RMS*	1.180	4.220	25.849	1.073	2.476	
Compounded Solution 1	1.208	4.864	27.347	1.112	—	12.110 (Z=0.1562)
Compounded Solution 2	1.208	3.073	6.480	1.004	*2.487	53.043 (Z=0.3125)

*RMS = Root-Mean-Square

Table 9 indicates the agreement between the first model and the FEM results is reasonably good. The second model has an effective width equal to that of an unbent angle-stringer. Table 9 indicates such a model gives a very low SIF for long cracks.

When a crack grows into the upright leg of an angle-stringer shown in Figure 67-e, only the second model described in the last paragraph will be applicable and it gives quite an accurate solution compared to the FEM results, shown in Table 9. In this case, the load eccentricity will induce out-of-plane bending. The bending stress can be calculated using Equation (79). The moment of inertia shall be calculated using the entire cross section of the angle-stringer. However, the bending moment shall be calculated using the stress in the fractured area.

When a crack grows through the entire base-leg and into the upright leg of an angle-stringer, as shown in Figure 67-f, a severe out-of-plane bending is introduced into the upright leg. Along the line AB in Figure 67-f, the crack is closed due to bending. But, along the line CD in Figure 67-f, the bending will further increase the crack opening displacement. Thus, the two models shown in Figure 68 are used to model the SIF at mid-thickness and at the line CD where maximum tension due to bending exists. The estimated maximum tensile stress due to bending is about 27 times that of remote stress. The SIF obtained in this manner agrees reasonably well with FEM result, as shown in Table 9.

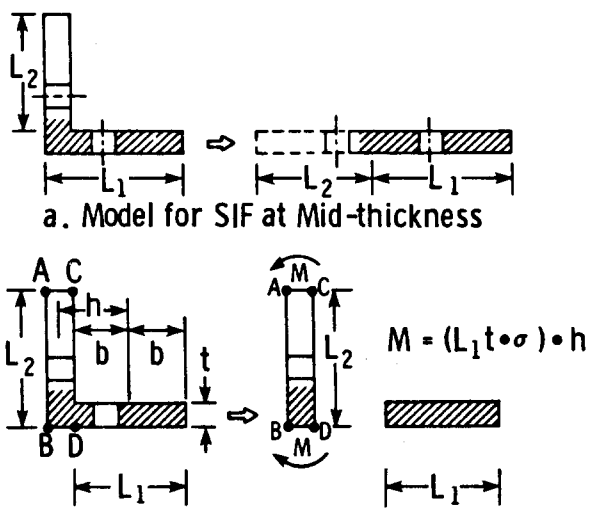

Figure 68. Angle-stringer Models for Compounded Solution Method

In summary, the SIF's for the cracked angle-stringer configurations pertinent to life predictions are given in Figures 69 through 72.

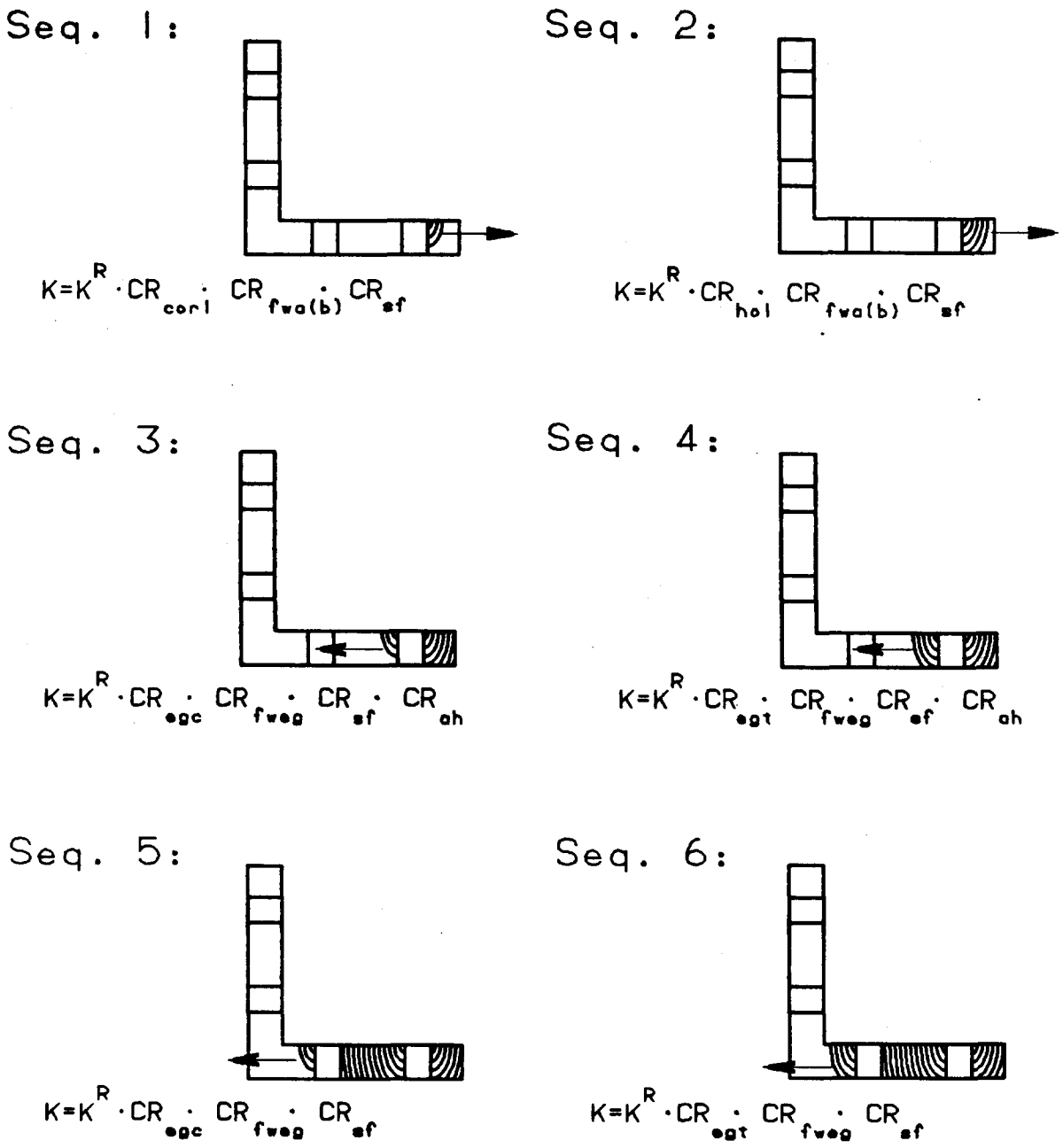

Figure 69. Cracking Sequence and Associated SIF for the Inside Initial Crack in Angle - Stringer - Without Crack Initiation

Seq. 1:

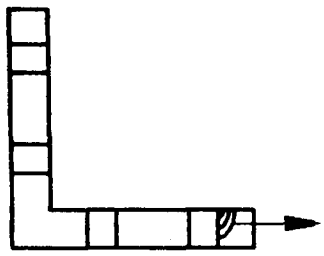

$K=K^R \cdot CR_{cori} \cdot CR_{fwa(b)} \cdot CR_{sf}$

Seq. 2:

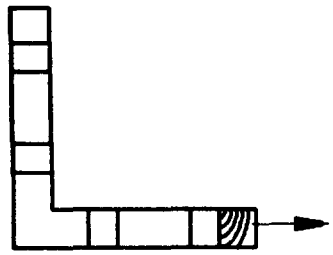

$K=K^R \cdot CR_{hol} \cdot CR_{fwa(b)} \cdot CR_{sf}$

Seq. 3:

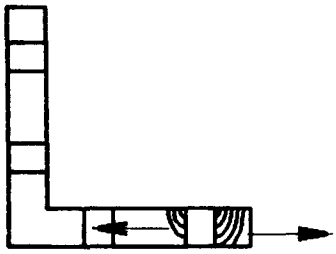

$K=K^R \cdot CR_{coth} \cdot CR_{fwa(b)} \cdot CR_{sf} \cdot CR_{ah}$

Seq. 4:

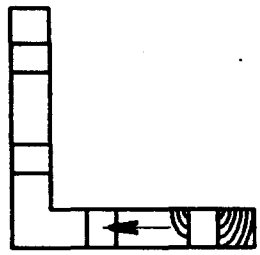

$K=K^R \cdot CR_{sgc} \cdot CR_{fwsg} \cdot CR_{sf} \cdot CR_{ah}$

Seq. 5:

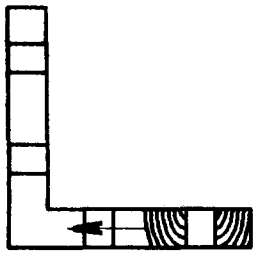

$K=K^R \cdot CR_{sgt} \cdot CR_{fwsg} \cdot CR_{sf} \cdot CR_{ah}$

Seq. 6:

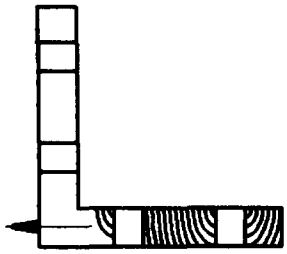

$K=K^R \cdot CR_{sgc} \cdot CR_{fwsg} \cdot CR_{sf}$

Seq. 7:

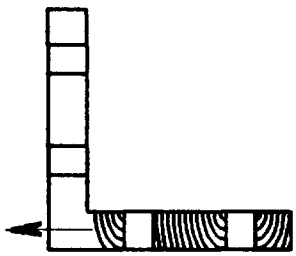

$K=K^R \cdot CR_{sgt} \cdot CR_{fwsg} \cdot CR_{sf}$

Figure 70. Cracking Sequence and Associated SIF for the Inside Initial Crack in Angle-Stringer - With Crack Initiation

Seq. 1:

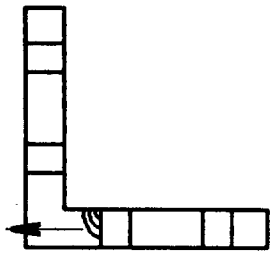

$K=K^R \cdot CR_{cor1} \cdot CR_{fwa(b)} \cdot CR_{sf}$

Seq. 2:

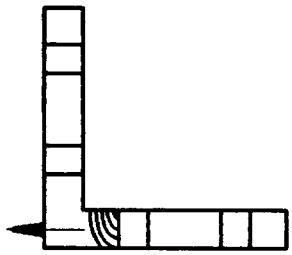

$K=K^R \cdot CR_{hol} \cdot CR_{fwa(b)} \cdot CR_{sf}$

Seq. 3:

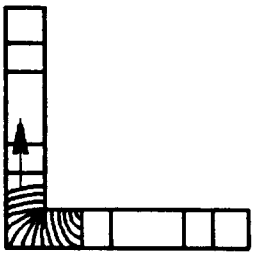

$K=K^R \cdot CR_{fwa(b)} \cdot CR_{ah} \cdot CR_b \cdot CR_{hol}$

Seq. 4:

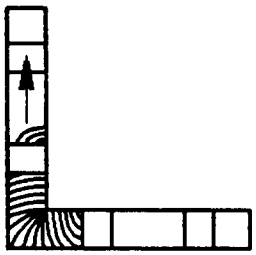

$K=K^R \cdot CR_{2cor1} \cdot CR_{fwa(b)} \cdot CR_b$

Seq. 5:

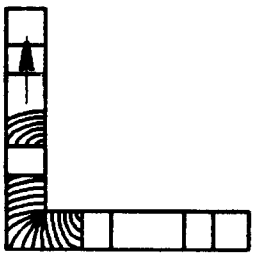

$K=K^R \cdot CR_{2hol} \cdot CR_{fwa(b)} \cdot CR_b$

Figure 71. Cracking Sequence and Associated SIF for the Outside Initial Crack in Angle-Stringer - Without Crack Initiation

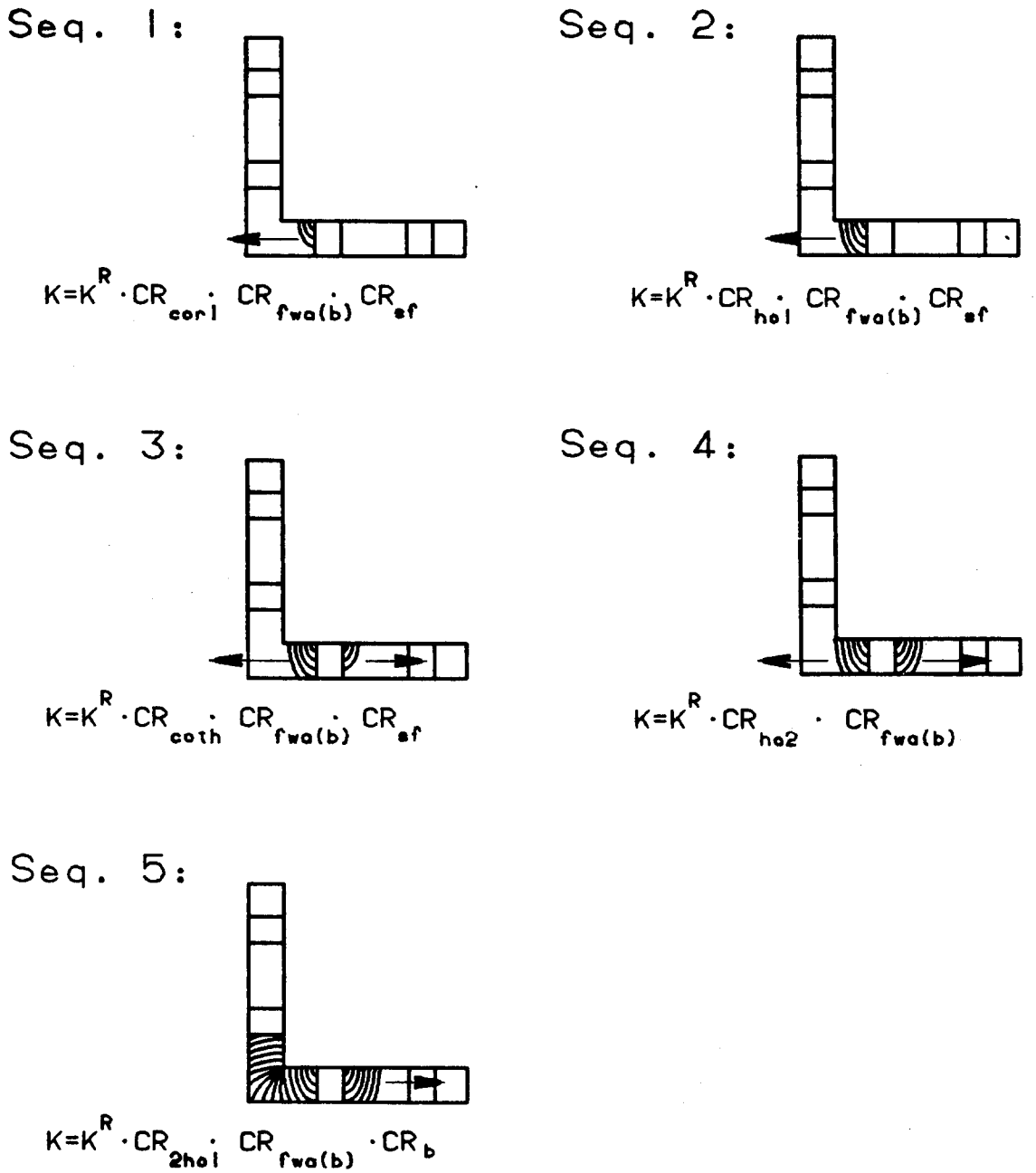

Figure 72. Cracking Sequence and Associated SIF for the Outside Initial Crack in Angle-Stringer - With Crack Initiation

3.2.4 Skins and Doublers in Lap-Joints

The crack growth in skins and doublers can be modeled in the manner shown in Figure 73 where a crack grows along an array of holes. The model shown in Figure 73 is applicable to both single-shear and double-shear lap joints. The skins and doublers in lap-joints are subjected to both remote stress and fastener load, whereas the skin in stringer-reinforced panels is subjected to remote stress only (assuming load redistribution due to crack growth is negligible). The crack in Figure 73 is located in one of the row 1 holes. To calculate the contributions of row 2 fastener loads to the SIF, Brussat el al (Ref. 3) treated the fastener loads as point loads. Since the typical distance between holes is four diameters for airframe design, the real loading condition of row 2 fasteners deviates considerably from the idealized point loads. In this investigation, the total row 2 fastener loads are converted to a remote stress as shown in Figure 73-b to simplify the analysis. For the row 1 fastener loads, P_{1j}, only the holes which are in the crack path will contribute to the SIF. Thus, only fastener loads P_{14} and P_{15} shown in Figure 73-d will contribute to the SIF. The total SIF (K) is the sum of K_r and K_f which are due to remote stress and fastener load, respectively. The remote stress is calculated using the gross section area. The fastener loads are calculated as a function of crack length. The FEM is well suited for the calculation. The computation of fastener load using on the FEM will be described in Section 3.3.

Figure 75 shows the cracking sequence without the consideration of crack initiation and the associated SIF.

For the case which considers crack initiation, the frictional force between the faying surfaces of the skin and doubler needs to be included in accordance with the analytical/experimental correlation due to Brussat et al (Ref. 3). Figure 74 shows a model which includes this frictional force. The f_{ij} in Figure 74 represents the frictional force due to each fastener. The external force F equals the sum of the fastener loads and frictional forces. It is evident that the fastener loads, P_{ij}, in Figure 74 are smaller than the P_{ij} in Figure 73. Thus, the presence of frictional forces reduces the amount of external load effects to crack growth. The computation of fastener loads with the consideration of faying surface frictional forces is given in Section 3.3. The frictional force between the fastener head (or collar) and skin (or doubler) may be neglected in crack growth analyses because their magnitudes are small compared to the faying surface frictional forces. However, this kind of frictional force needs to be considered in the analysis of crack initiation which is a very localized event.

Figure 76 shows the cracking sequence with the consideration of crack initiation and the associated SIF.

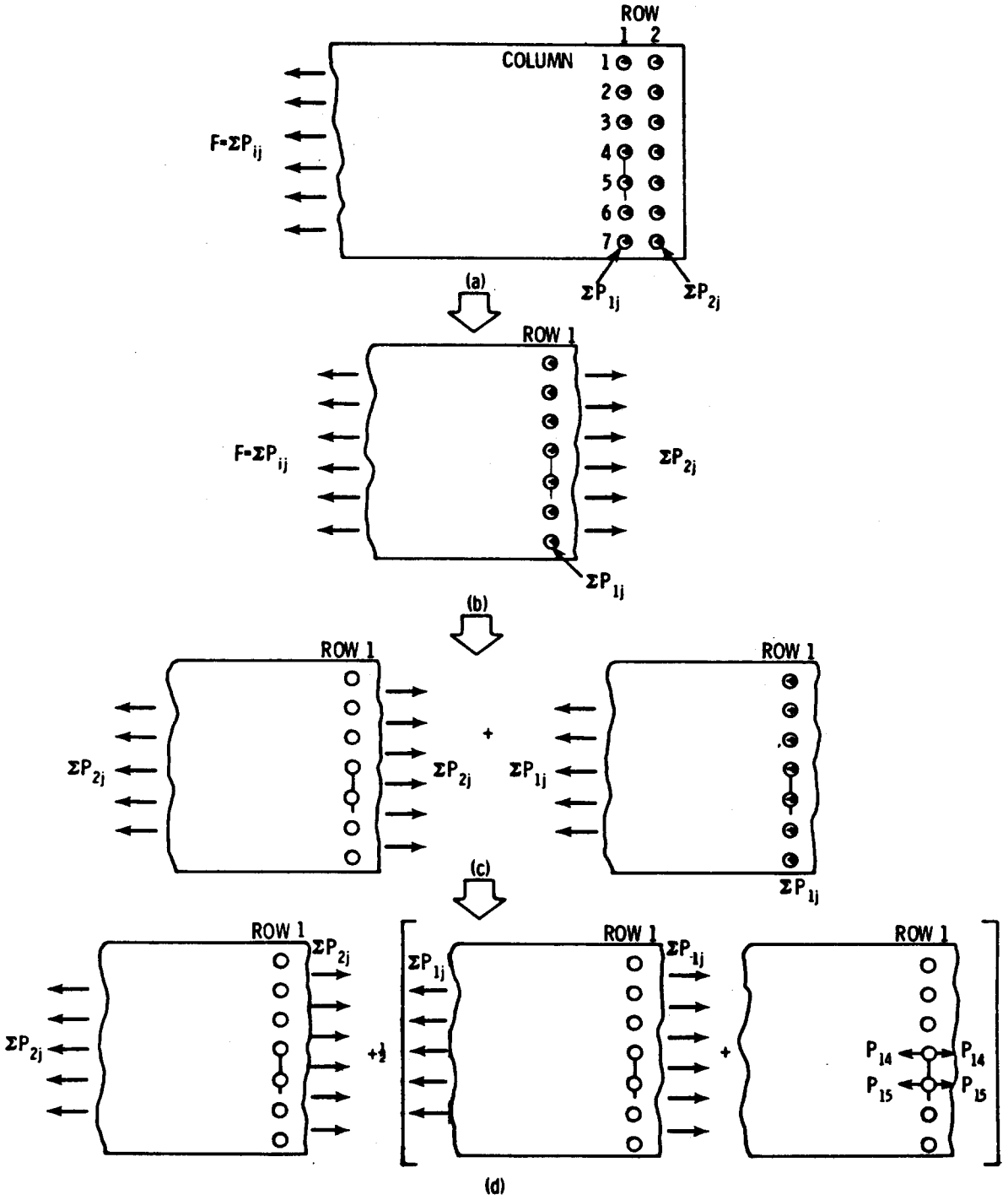

Figure 73. A Model for Skins and Doublers in Lap-joints - No Friction

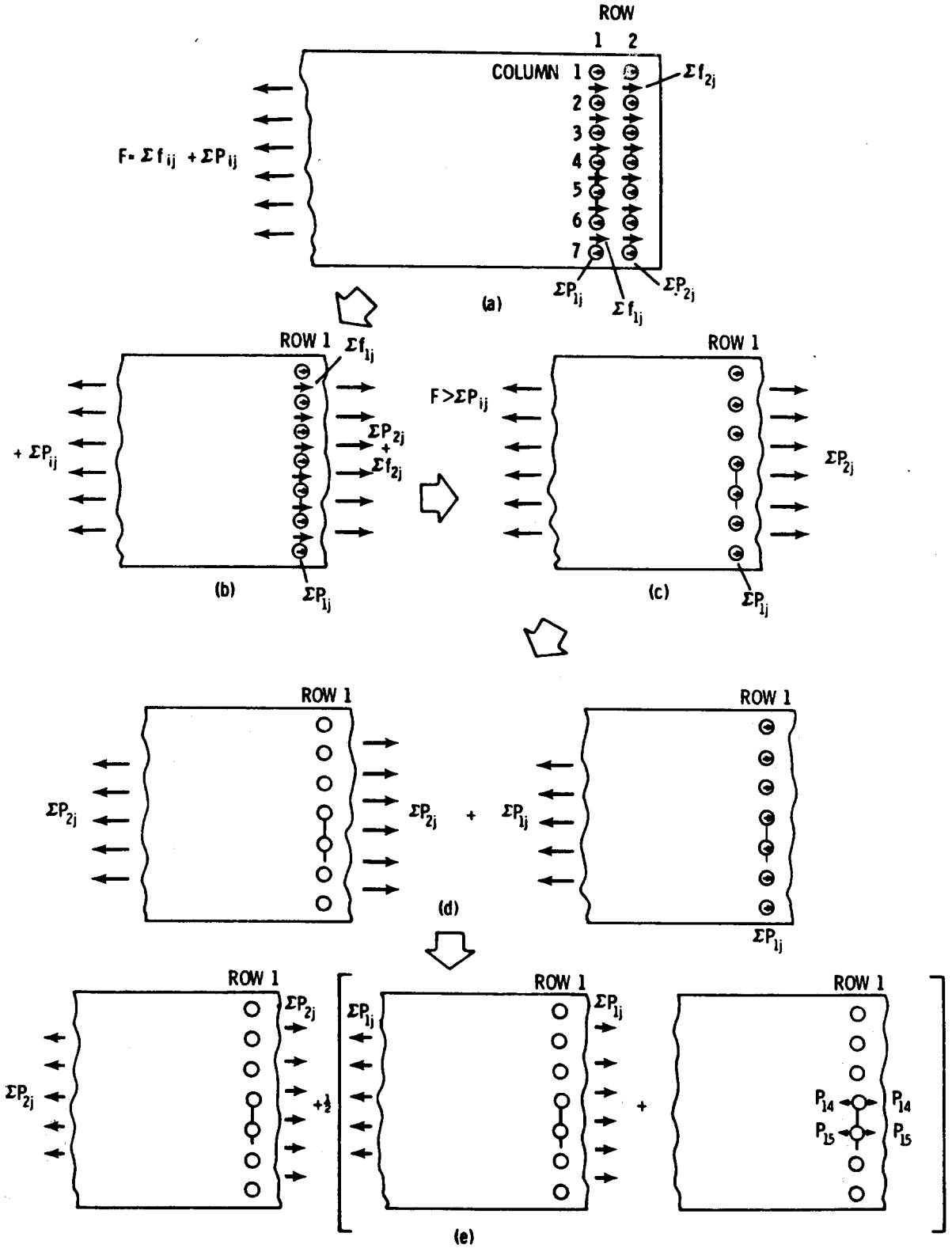

Figure 74. A Model for Skins and Doublers in Lap-joints - With Friction

Seq. 1:

$K_r = K^R \cdot CR_{cor1} \cdot CR_{ah} \cdot CR_{fwa(b)}$

$K_f = K^P \cdot CP_{cor1} \cdot CR_{ah} \cdot CP_{fwa(b)}$

Seq. 2:

$K_r = K^R \cdot CR_{hol} \cdot CR_{ah} \cdot CR_{fwa(b)}$

$K_f = K^P \cdot CP_{hol} \cdot CR_{ah} \cdot CP_{fwa(b)}$

Seq. 3:

$K_r = K^R \cdot CR_{2cor1} \cdot CR_{ah} \cdot CR_{fwa(b)}$

$K_f = K^P \cdot CP_{2cor1} \cdot CR_{ah} \cdot CP_{fwa(b)}$

Seq. 4:

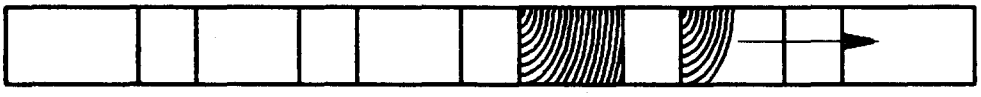

$K_r = K^R \cdot CR_{2hol} \cdot CR_{ah} \cdot CR_{fwa(b)}$

$K_f = K^P \cdot CP_{2hol} \cdot CR_{ah} \cdot CP_{fwa(b)}$

Seq. 5:

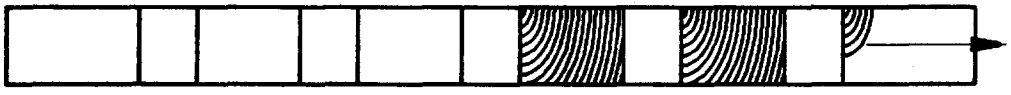

$K_r = K^R \cdot CR_{2cor1} \cdot CR_{ah} \cdot CR_{fwa(b)}$

$K_f = K^P \cdot CP_{2cor1} \cdot CR_{ah} \cdot CP_{fwa(b)}$

Seq. 6:

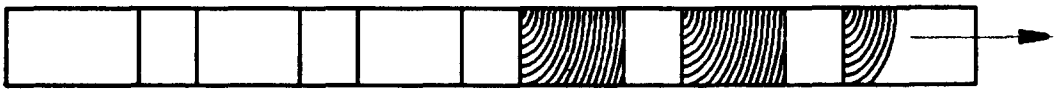

$K_r = K^R \cdot CR_{2hol} \cdot CR_{ah} \cdot CR_{fwa(b)}$

$K_f = K^P \cdot CP_{2hol} \cdot CR_{ah} \cdot CP_{fwa(b)}$

Figure 75. Cracking Sequence and Associated SIF for Figure 73

Seq. 1:

$K_r = K^R \cdot CR_{cor1} \cdot CR_{ah} \cdot CR_{fwa(b)}$

$K_f = K^P \cdot CP_{cor1} \cdot CR_{ah} \cdot CP_{fwa(b)}$

Seq. 2:

$K_r = K^R \cdot CR_{hol} \cdot CR_{ah} \cdot CR_{fwa(b)}$

$K_f = K^P \cdot CP_{hol} \cdot CR_{ah} \cdot CP_{fwa(b)}$

Seq. 3:

$K_r = K^R \cdot CR_{coth} \cdot CR_{ah} \cdot CR_{fwa(b)}$

$K_f = K^P \cdot CP_{coth} \cdot CR_{ah} \cdot CP_{fwa(b)}$

Seq. 4:

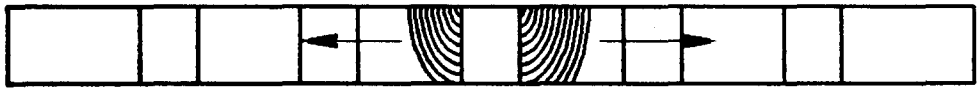

$K_r = K^R \cdot CR_{ho2} \cdot CR_{ah} \cdot CR_{fwa(b)}$

$K_f = K^P \cdot CP_{ho2} \cdot CR_{ah} \cdot CP_{fwa(b)}$

Seq. 5:

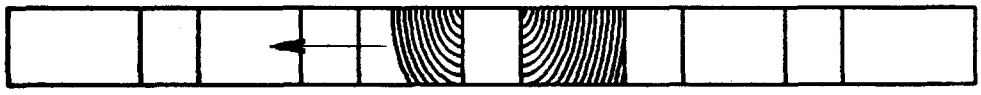

$K_r = K^R \cdot CR_{2hol} \cdot CR_{ah} \cdot CR_{fwa(b)}$

$K_f = K^P \cdot CP_{2hol} \cdot CR_{ah} \cdot CP_{fwa(b)}$

Seq. 6:

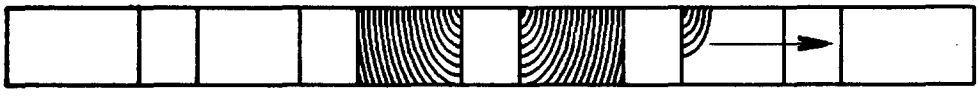

$K_r = K^R \cdot CR_{2cor1} \cdot CR_{ah} \cdot CR_{fwa(b)}$

$K_f = K^P \cdot CP_{2cor1} \cdot CR_{ah} \cdot CP_{fwa(b)}$

Seq. 7:

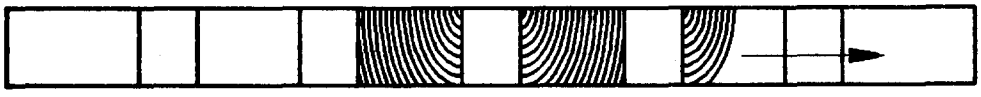

$K_r = K^R \cdot CR_{2hol} \cdot CR_{ah} \cdot CR_{fwa(b)}$

$K_f = K^P \cdot CP_{2hol} \cdot CR_{ah} \cdot CP_{fwa(b)}$

Figure 76. Cracking Sequence and Associated SIF for Figure 74

3.3 Fastener Load Distributions in Cracked Lap-Joints

3.3.1 General Approach

In order to obtain accurate stress intensity factors in lap-joints, the fastener load distributions need to be accurately determined. The two-dimensional FEM is well suited to solve the fastener load distributions in the single-shear and double-shear lap-joint specimens to be used in Task IV - Structural Tests.

The QUAD8 element in MSC/NASTRAN is adopted for modeling both the skin and doubler of a lap-joint. The QUAD8 element, which is an 8-noded quadratic quadrilateral isoparametric element, can simulate curved boundaries better than other types of elements. The fastener holes can be idealized as a nodal point except along the row of holes in the crack path. Here, the boundaries of the holes must be realistically modeled. The modeling technique to compensate for the loss of stiffness due to these holes is explained below.

Each fastener is modeled as a spring element (ELAS2 element) in MSC/NASTRAN. The spring constant of each fastener is calculated as a function of plate thickness, Young's moduli of plates and fasteners, hole size, plate width, and Poisson's ratio of the fasteners. Barrois' method (Ref. 27) was used in the calculation. A computer program, FASTENER, based on Barrois method was developed previously by Fairchild Republic Co. under a separate funding. Two ELAS2 elements are required to model a fastener; one ELAS2 for the loading direction and the other ELAS2 for the direction perpendicular to loading.

In Ref. 3, an elaborated finite element analysis was performed to obtain the spring constant for the fasteners. Whether such an analysis will give better result is questionable. The important point is that the fastener load distribution is only slightly affected by the magnitude of the fastener spring constant. This fact has been demonstrated on page 168 of Ref. 27 and was further confirmed herein. In this investigation, the same finite element model was analyzed using two different spring constants: the FASTENER program gave a value of 7.4×10^5 lb/in. while Swift and Wang's formula (Ref. 28) yielded 9.5×10^5 lb/in. (a 28.4% increase). The two computer runs give essentially the same results. Incidentally, Swift and Wang's formula indicates that the spring constant increases with increasing stacking thickness. This functional relationship

common engineering principles which indicate that as the fastener length increases, its spring constant decreases.

The interface between the fastener and hole boundary is modeled as a set of rod elements, i.e. ROD element in MSC/NASTRAN. To determine the actual contact region between the fastener and hole boundary, iterations of computer runs are made. In the first computer run, the rod elements are distributed around the entire hole boundary. In each iteration, if a tensile load exists in a rod element, that particular rod element is removed in the next iteration. The iterations continue until no tensile load exists in any rod element. The final contact region can be determined in as few as three iterations.

As stated earlier, the faying surface frictional forces need to be considered in the combined crack growth and initiation method of life prediction; otherwise, the life prediction will be overly conservative. The frictional force per faying surface per fastener F, can be calculated with the following empirical formula where μ is static coefficient between faying surfaces and P is preload in a fastener.

$$F = \mu \cdot P \tag{84}$$

$$P = 0.25 \cdot \text{(Ultimate Strength of Collar as Specified by Manufacturer)} \tag{85}$$

TABLE 10. EXPERIMENTAL VERIFICATION OF FRICTION FORCE EQUATION

FASTENER DIAMETER	EXPERIMENTAL "F"	PREDICTED "F"
0.375 INCH	979 lb. (Brussat et al, Ref 3)	910 lb.
0.50 INCH	1800 lb. (Yen & Smillie, Ref. 29)	1625 lb.

Table 10 shows a comparison of faying surface friction force obtained from experiments and Equations (84) and (85). The μ is experimentally determined by setting a piece of 2024-T3 sheet (0.188 inch thick) on the surface of another piece of 2024-T3 sheet (0.188 inch thick), tilting the sheets until sliding occurs, and measuring the tangent of the angle with horizontal. The value of μ determined in this manner is 0.52. It is noted that the value depends very much on the finishing of the faying surfaces. The μ value of 0.52 represents the faying surface condition of the Task IV structural test specimens. The preload in a fastener is nominally about 50% of the ultimate strength of a fastener at shear-off of collar. Thus, Equation (85) is a very conservative estimation of preload. The experimental friction force of 979 lb for a 0.375 inch fastener shown in Table 10 is the lower estimate from experiment (Ref. 3); the upper estimate is about 1583 lb. Considering the complexity of actual airframe structures and the possible loss of preload due to wear-out, Equation (85) will be a conservative and safe approach to treat the beneficial effect of faying surface friction force. Table 10 does indicate that predicted friction force agree well with experiments.

In the FEM analysis, the frictional forces were applied as point loads in opposite directions to the pair of nodal points which are connected by the two spring elements used to simulate a fastener. However, the frictional forces were uniformly applied as surface tractions to the first-ring elements surrounding the holes in the cracking path.

3.3.2 Single-Shear Lap-Joint Specimen

The basic considerations required to model a lap-joint specimen is already described in Section 3.3.1. In this section, a step-by-step procedure is given below for a single-shear lap-joint specimen.

Step 1:

The single-shear lap-joint specimen is idealized as shown in Figure 79. The island in the doubler, if any, and rib need to be considered in the idealized specimen.

Step 2:

Spring elements are used to simulate fasteners. Barrois' method (Ref. 27) is used to calculate the spring constant. The distance between two fasteners is used as the effective plate width in the calculation. The spring constant for each row of fasteners may not be the same. It depends primarily on the thickness, fastener diameter, and Young's moduli.

Step 3:

Figure 79 is modeled as shown in Figure 80 which consists of 632 QUAD8 elements, 32 TRIA6 elements, 56 ELAS2 elements and 150 ROD elements. There are 2317 nodal points in the model. The area surrounding the crack path is modeled as shown in Figure 81. Two nodal points are assigned to each grid point along the crack line. These two nodal points simulate the upper and lower surfaces of the crack. When there is no crack, each pair of nodal points along the crack line are connected by a rigid rod to close up the crack. When a crack of a certain length exists, the rigid rods between the upper and lower crack surfaces are removed. Such a technique to simulate a crack allows the use of one finite element model to analyze several cracked lap-joint configurations of different lengths.

Step 4:

The fasteners are connected to the hole boundaries by rigid rod elements as shown in Figure 82. Iterations of computer runs are made to determine the actual contact points between fasteners and holes.

Step 5:

Since most of the fastener holes (except those along cracking path) are modeled as nodal points in the finite element model, to obtain a realistic fastener load distribution, a compensation needs to be made for the loss of stiffness due to the circular cut-outs. This is done by increasing the spring constant of the fasteners in that particular row. The amount of increase in the spring constant is obtained by iterating computer runs until the proper load distribution is achieved. For example, the loads in rows 1 and 4 of Figure 79 should be the same and the loads in rows 2 and 3 should be the same. Note that the loads in rows 1 and 2 will not be the same due to the difference in stacking thickness.

Step 6:

When the faying surface frictional force is to be considered in the analysis, Equations (84) and (85) are used to calculate the frictional force per faying surface per fastener.

The procedures described above have been used to calculate the fastener load distributions in single-shear lap-joint specimens. Calculations were made for two cases. In the first case, no frictional force was considered according to the current MIL-A-83444; analyses were made for six different crack lengths. In the second case, frictional

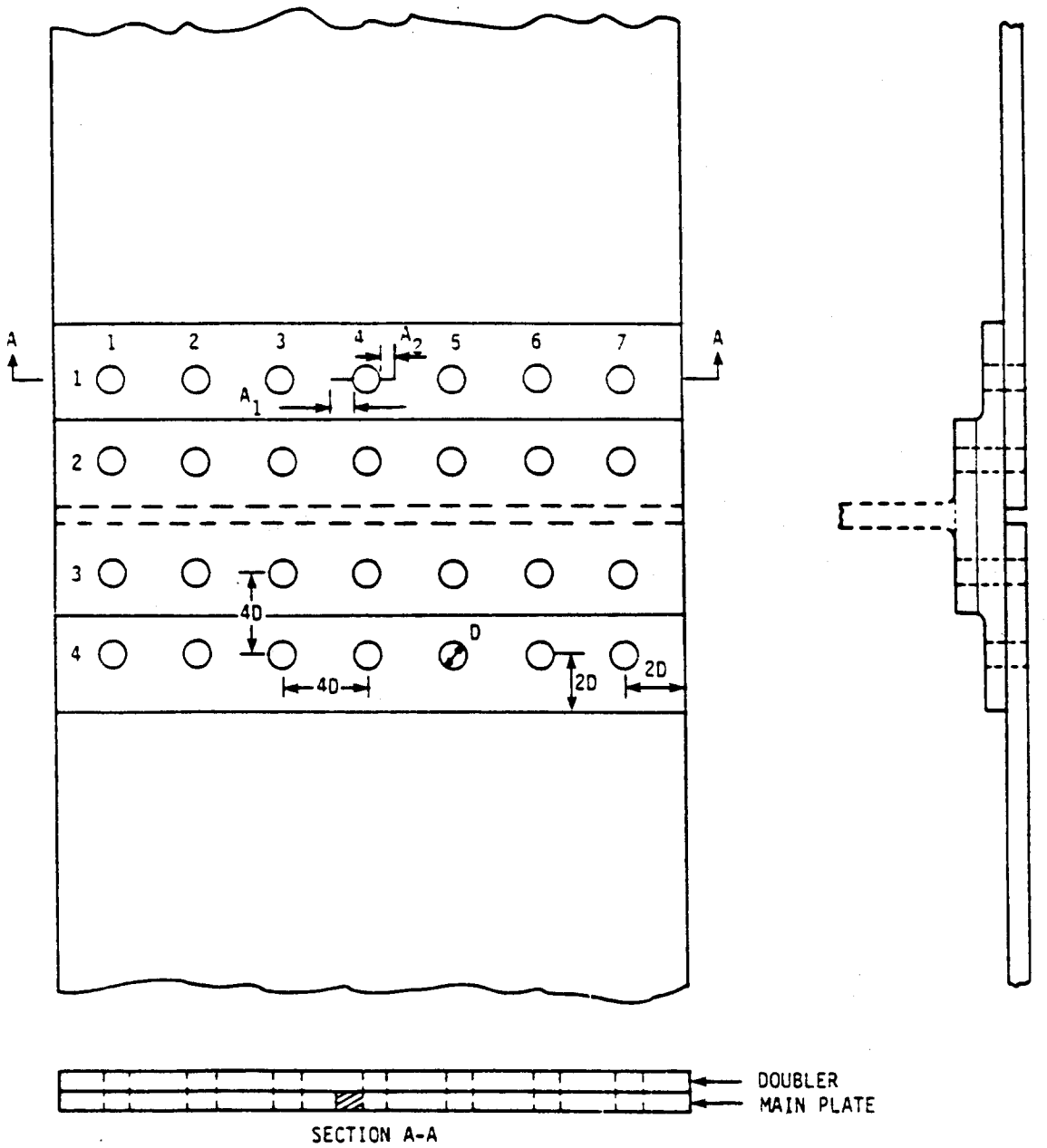

Figure 79. Single-shear Lap-joint Specimen

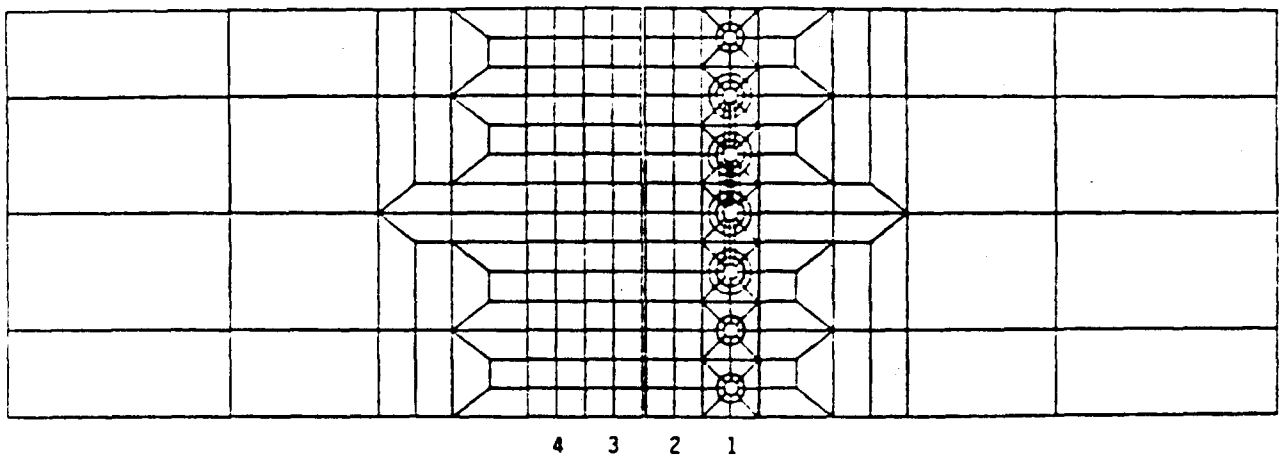

Figure 80. Finite Element Model for Single-shear Lap-joint Specimen

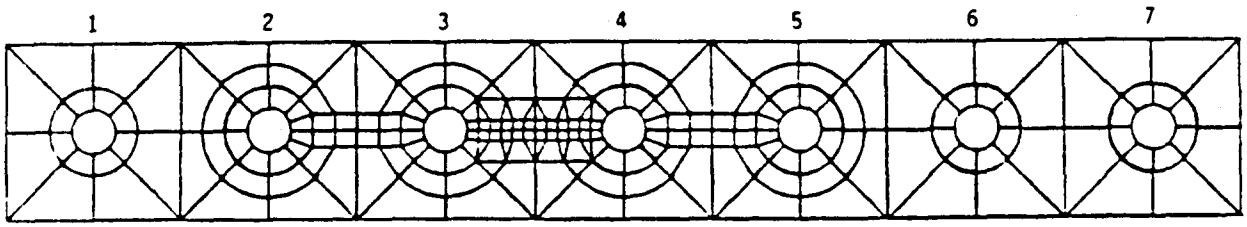

Figure 81. Detail of the Area Surrounding Row I Holes

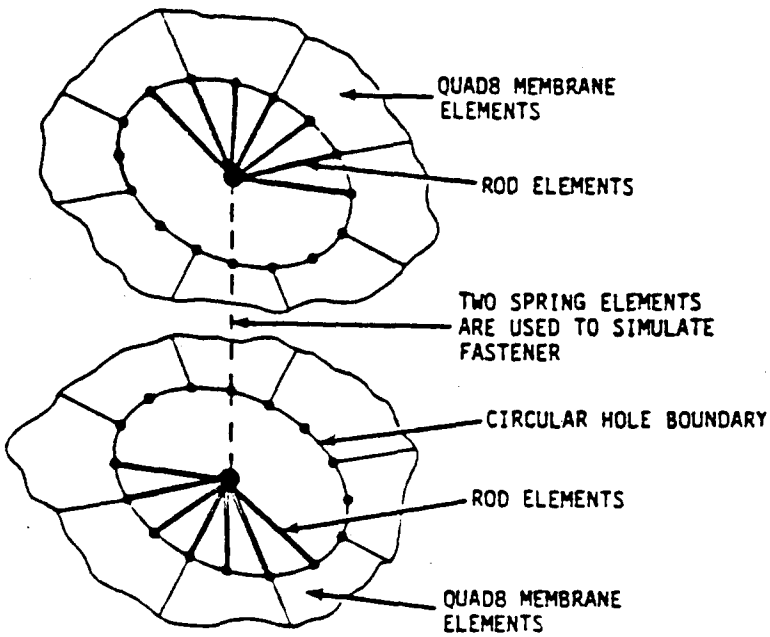

Figure 82. Modeling of the Interface Between the Hole and Fastener

force was considered according to the combined crack growth and initiation method for life prediction as required by Task III; analyses were made for seven different crack lengths.

Table 11 shows the normalized fastener load distributions for the case without frictional forces. The fastener loads are normalized with respect to the average fastener load which is defined as the total applied load divided by the number of fasteners. This way of data presentation will facilitate the application of the computed result for a particular applied load level to any other load levels in a stress spectrum. In the table, the number within the parentheses corresponds to the hole which has an initial crack. For the case without friction, the spring constants for each row of fasteners are:

row 1	=	0.8999E6	lb/in. (21.5% increase w.r.t. row 4)
row 2	=	0.6644E6	lb/in.
row 3	=	0.6644E6	lb/in.
row 4	=	0.7405E6	lb/in.

Since the stacking thickness of rows 2 and 3 is larger (due to the rib and the island in the doubler) than that of rows 1 and 4, the spring constants of rows 2 and 3 are lower than those of rows 1 and 4. As expected, Table 11 shows that the loads in rows 1 and 4 are slightly higher than the loads in rows 2 and 3. This is due to the large spring constants for rows 1 and 4. The data shown in Table 11 are plotted in Figure 83 for the row 1 fasteners to show the change in fastener loads for various crack lengths. Table 11 indicates that there is no substantial load variation in rows 3 and 4, whereas there is a drastic load variation in rows 1 and 2. The crack grows from fastener No. 4 toward fastener No. 3 along row 1. Six crack lengths, A_1= 2R, 4R, 6R, 10R, 12R and 14R, were analyzed. Crack A_2 is assumed to be zero in accordance with MIL-A-83444. The crack lengths A_1= 6R and 14R correspond to one and two ligments broken, respectively. As can be seen from Figure 83, there is a drastic decrease of load in fastener No. 3 after one ligment is broken. The normalized fastener loads for fastener Nos. 3 and 4 are curve-fitted into the following expressions as a function of A_1.

$$\frac{P_4}{P_{AVG}} = 1.00374 - 0.018805 \frac{A_1}{R}, \quad \text{for } \frac{A_1}{R} \leq 6 \tag{86}$$

$$\frac{P_4}{P_{AVG}} = 0.88896 + 0.00608 \left(\frac{A_1}{R} - 8\right), \quad \text{for } \frac{A_1}{R} \geq 8 \tag{87}$$

$$\frac{P_3}{P_{AVG}} = 0.89609 - 0.06003 \left(\frac{A_1}{R} - 8\right), \quad \text{for } \frac{A_1}{R} \geq 8 \tag{88}$$

TABLE 11. NORMALIZED FASTENER LOAD DISTRIBUTION OF SINGLE-SHEAR LAP-JOINT SPECIMEN -- NO FRICTION

SINGLE LAP JOINT MODEL W/O FRICTION
INTACT MAIN PLATE, KX(1)=0.8999E6 (21.5% INCR), KX(2,3)=0.6644E6
NORMALIZED FASTENER LOADS, PI/PAVG, (PAVG = 1953.125 LBS.)

COL / ROW	1	2	3	4	5	6	7
1	1.0752	1.0226	1.0120	(1.0095)	1.0118	1.0242	1.0749
2	1.0103	0.9589	0.9450	0.9418	0.9447	0.9591	1.0099
3	-0.9987	-0.9535	-0.9430	-0.9409	-0.9431	-0.9535	-0.9986
4	-1.0730	-1.0304	-1.0212	-1.0197	-1.0212	-1.0304	-1.0730

SINGLE LAP JOINT MODEL W/O FRICTION
MAIN PLATE CRACK LENGTH OF (+02R)
NORMALIZED FASTENER LOADS, PI/PAVG, (PAVG = 1953.125 LBS.)

COL / ROW	1	2	3	4	5	6	7
1	1.0824	1.0304	1.0186	(0.9589)	1.0201	1.0310	1.0802
2	1.0177	0.9662	0.9431	0.9228	0.9475	0.9656	1.0154
3	-1.0007	-0.9538	-0.9416	-0.9386	-0.9419	-0.9540	-1.0005
4	-1.0748	-1.0306	-1.0200	-1.0179	-1.0202	-1.0307	-1.0747

SINGLE LAP JOINT MODEL W/O FRICTION
MAIN PLATE CRACK LENGTH OF (+04R)
NORMALIZED FASTENER LOADS, PI/PAVG, (PAVG = 1953.125 LBS.)

COL / ROW	1	2	3	4	5	6	7
1	1.0938	1.0406	1.0177	(0.9257)	1.0290	1.0391	1.0863
2	1.0294	0.9739	0.9254	0.8925	0.9512	0.9736	1.0217
3	-1.0033	-0.9541	-0.9395	-0.9357	-0.9406	-0.9547	-1.0027
4	-1.0773	-1.0309	-1.0184	-1.0157	-1.0190	-1.0313	-1.0768

SINGLE LAP JOINT MODEL W/O FRICTION
MAIN PLATE CRACK LENGTH OF (+06R)
NORMALIZED FASTENER LOADS, PI/PAVG, (PAVG = 1953.125 LBS.)

COL / ROW	1	2	3	4	5	6	7
1	1.1388	1.0811	0.8990	(0.8952)	1.0583	1.0621	1.1006
2	1.0748	0.9956	0.8467	0.8422	0.9720	0.9966	1.0368
3	-1.0122	-0.9542	-0.9317	-0.9277	-0.9377	-0.9572	-1.0089
4	-1.0852	-1.0313	-1.0127	-1.0092	-1.0161	-1.0331	-1.0828

TABLE II. NORMALIZED FASTENER LOAD DISTRIBUTION OF SINGLE-SHEAR LAP-JOINT SPECIMEN -- NO FRICTION (CONT'D)

SINGLE LAP JOINT MODEL W/O FRICTION
MAIN PLATE CRACK LENGTH OF (+10R)
NORMALIZED FASTENER LOADS, PI/PAVG, (PAVG = 1953.125 LBS.)

COL / ROW	1	2	3	4	5	6	7
1	1.1788	1.1133	0.7670	(0.8973)	1.0790	1.0759	1.1068
2	1.1140	1.0052	0.7898	0.8297	0.9891	1.0105	1.0436
3	-1.0185	-0.9536	-0.9260	-0.9227	-0.9366	-0.9590	-1.0125
4	-1.0906	-1.0312	-1.0087	-1.0052	-1.0147	-1.0345	-1.0863

SINGLE LAP JOINT MODEL W/O FRICTION
MAIN PLATE CRACK LENGTH OF (+12R)
NORMALIZED FASTENER LOADS, PI/PAVG, (PAVG = 1953.125 LBS.)

COL / ROW	1	2	3	4	5	6	7
1	1.2297	1.1347	0.6653	(0.9022)	1.1029	1.0904	1.1111
2	1.1606	0.9874	0.7113	0.8207	1.0099	1.0252	1.0487
3	-1.0250	-0.9525	-0.9199	-0.9181	-0.9358	-0.9609	-1.0158
4	-1.0962	-1.0309	-1.0045	-1.0013	-1.0136	-1.0359	-1.0896

SINGLE LAP JOINT MODEL W/O FRICTION
MAIN PLATE CRACK LENGTH OF (+14R)
NORMALIZED FASTENER LOADS, PI/PAVG, (PAVG = 1953.125 LBS.)

COL / ROW	1	2	3	4	5	6	7
1	1.3887	1.0001	0.5327	(0.9341)	1.1622	1.1198	1.1098
2	1.2873	0.8888	0.5782	0.8291	1.0637	1.0555	1.0500
3	-1.0389	-0.9480	-0.9068	-0.9102	-0.9360	-0.9652	-1.0213
4	-1.1079	-1.0293	-0.9955	-0.9943	-1.0124	-1.0390	-1.0952

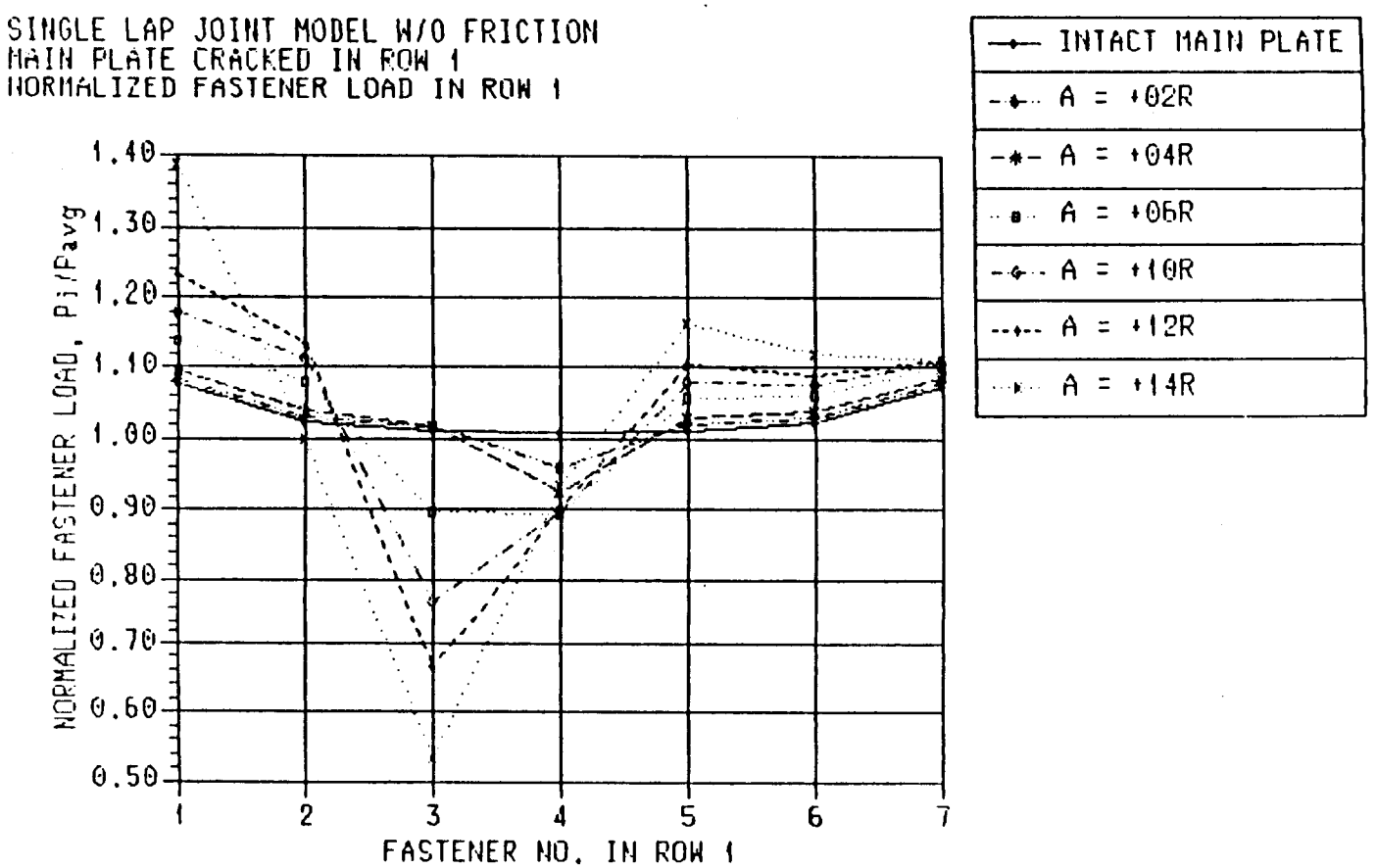

Figure 83. Fastener Load Distribution in Row 1 of Single-shear Lap-joint Specimen -- No Friction

Table 12 shows the normalized fastener load distributions for the case with frictional forces. The fastener loads are normalized with respect to the average fastener load, which is defined as the total fastener load (which equals the total applied load minus total frictional forces) divided by the number of fasteners. For the case with friction, the spring constants for each row of fasteners are:

row 1	=	0.8395E6	lb/in. (13.4% increase w.r.t. row 4)
row 2	=	0.6644E6	lb/in.
row 3	=	0.6644E6	lb/in.
row 4	=	0.7405E6	lb/in.

Seven models corresponding to the seven crack lengths shown below were analyzed:

(1)	A_1 =2R,	A_2 =	0.
(2)	A_1 =4R,	A_2 =	0.
(3)	A_1 =6R,	A_2 =	0. One ligment broken
(4)	A_1 =6R,	A_2 =	2R One ligment broken
(5)	A_1 =10R,	A_2 =	4R One ligment broken
(6)	A_1 =12R,	A_2 =	6R Two ligments broken
(7)	A_1 =14R,	A_2 =	6R Three ligments broken

where A_1 and A_2 are the crack lengths from the R.H.S. and L.H.S. of a hole, respectively (see Figure 79). The above combination of A_1 and A_2 is expected to be commensurated with the anticipated crack growth and crack initiation behavior. Table 12 shows the normalized fastener load distribution for various crack lengths. The data in Table 12 are plotted in Figure 84 for the row 1 fasteners. The figure shows that there is a substantial change in load as the crack grows. Table 12 shows that the loads in fastener Nos. 3 and 4 of rows 1 and 2 drop drastically after two ligments are broken. This phenomenon can be explained as follows. When cracks A_1 and A_2 become long enough, there is a great decrease in the local plate stiffness. Hence, the load passing through the fasteners in this region is also reduced. The little load in these fasteners is then further decreased by the faying surface frictional forces.

TABLE 12. NORMALIZED FASTENER LOAD DISTRIBUTION OF SINGLE-SHEAR LAP-JOINT SPECIMEN -- WITH FRICTION

SINGLE LAP JOINT MODEL W/ FRICTION
INTACT MAIN PLATE, KX(1)=0.8395E6 (13.4% INCR), KX(2,3)=0.6644E6
NORMALIZED FASTENER LOADS, PI/PAVG, (PAVG = 1906.250 LBS.)

COL / ROW	1	2	3	4	5	6	7
1	1.1051	1.0276	1.0123	(1.0087)	1.0121	1.0315	1.1058
2	1.0425	0.9643	0.9438	0.9393	0.9436	0.9658	1.0430
3	-1.0319	-0.9613	-0.9448	-0.9415	-0.9449	-0.9613	-1.0319
4	-1.1050	-1.0383	-1.0235	-1.0209	-1.0235	-1.0383	-1.1050

SINGLE LAP JOINT MODEL W/ FRICTION
MAIN PLATE CRACK LENGTH OF (+02R)
NORMALIZED FASTENER LOADS, PI/PAVG, (PAVG = 1906.250 LBS.)

COL / ROW	1	2	3	4	5	6	7
1	1.1146	1.0380	1.0210	(0.9419)	1.0227	1.0405	1.1129
2	1.0527	0.9745	0.9411	0.9128	0.9472	0.9748	1.0507
3	-1.0346	-0.9618	-0.9429	-0.9383	-0.9432	-0.9620	-1.0344
4	-1.1076	-1.0387	-1.0218	-1.0185	-1.0221	-1.0388	-1.1074

SINGLE LAP JOINT MODEL W/ FRICTION
MAIN PLATE CRACK LENGTH OF (+04R)
NORMALIZED FASTENER LOADS, PI/PAVG, (PAVG = 1906.250 LBS.)

COL / ROW	1	2	3	4	5	6	7
1	1.1303	1.0522	1.0199	(0.8958)	1.0348	1.0518	1.1215
2	1.0696	0.9858	0.9161	0.8690	0.9522	0.9863	1.0600
3	-1.0384	-0.9623	-0.9399	-0.9343	-0.9414	-0.9630	-1.0376
4	-1.1110	-1.0391	-1.0195	-1.0154	-1.0204	-1.0395	-1.1104

SINGLE LAP JOINT MODEL W/ FRICTION
MAIN PLATE CRACK LENGTH OF (+06R)
NORMALIZED FASTENER LOADS, PI/PAVG, (PAVG = 1906.250 LBS.)

COL / ROW	1	2	3	4	5	6	7
1	1.1921	1.1067	0.8592	(0.8540)	1.0746	1.0832	1.1411
2	1.1345	1.0161	0.8038	0.7975	0.9819	1.0192	1.0815
3	-1.0508	-0.9623	-0.9291	-0.9230	-0.9375	-0.9664	-1.0461
4	-1.1220	-1.0396	-1.0117	-1.0064	-1.0164	-1.0421	-1.1186

TABLE 12. NORMALIZED FASTENER LOAD DISTRIBUTION OF SINGLE-SHEAR LAP-JOINT SPECIMEN -- WITH FRICTION (CONT'D)

SINGLE LAP JOINT MODEL W/ FRICTION
MAIN PLATE CRACK LENGTH OF (+06R,-02R)
NORMALIZED FASTENER LOADS, PI/PAVG, (PAVG = 1906.250 LBS.)

COL / ROW	1	2	3	4	5	6	7
1	1.2236	1.1397	0.8610	(0.6741)	1.1062	1.1150	1.1672
2	1.1680	1.0445	0.7854	0.7144	0.9860	1.0509	1.1095
3	-1.0596	-0.9639	-0.9227	-0.9129	-0.9320	-0.9685	-1.0544
4	-1.1302	-1.0408	-1.0066	-0.9987	-1.0118	-1.0437	-1.1264

SINGLE LAP JOINT MODEL W/ FRICTION
MAIN PLATE CRACK LENGTH OF (+10R,-04R)
NORMALIZED FASTENER LOADS, PI/PAVG, (PAVG = 1906.250 LBS.)

COL / ROW	1	2	3	4	5	6	7
1	1.3281	1.2357	0.6543	(0.5012)	1.1582	1.1823	1.2214
2	1.2769	1.1004	0.6717	0.5575	0.9753	1.1141	1.1683
3	-1.0816	-0.9656	-0.9052	-0.8909	-0.9214	-0.9738	-1.0725
4	-1.1500	-1.0428	-0.9933	-0.9813	-1.0025	-1.0478	-1.1434

SINGLE LAP JOINT MODEL W/ FRICTION
MAIN PLATE CRACK LENGTH OF (+12R,-06R)
NORMALIZED FASTENER LOADS, PI/PAVG, (PAVG = 1906.250 LBS.)

COL / ROW	1	2	3	4	5	6	7
1	1.5271	1.3985	0.4551	(0.2524)	0.9560	1.3585	1.3818
2	1.4789	1.1737	0.4939	0.2670	0.8154	1.2475	1.3395
3	-1.1257	-0.9716	-0.8739	-0.8446	-0.8922	-0.9816	-1.1150
4	-1.1904	-1.0486	-0.9683	-0.9442	-0.9788	-1.0545	-1.1827

SINGLE LAP JOINT MODEL W/ FRICTION
MAIN PLATE CRACK LENGTH OF (+14R,-06R)
NORMALIZED FASTENER LOADS, PI/PAVG, (PAVG = 1906.250 LBS.)

COL / ROW	1	2	3	4	5	6	7
1	1.8632	1.1924	0.2164	(0.1955)	1.0429	1.4582	1.4207
2	1.7685	1.0099	0.1923	0.1724	0.8826	1.3442	1.3862
3	-1.1635	-0.9652	-0.8412	-0.8168	-0.8846	-0.9918	-1.1367
4	-1.2230	-1.0474	-0.9448	-0.9210	-0.9702	-1.0622	-1.2039

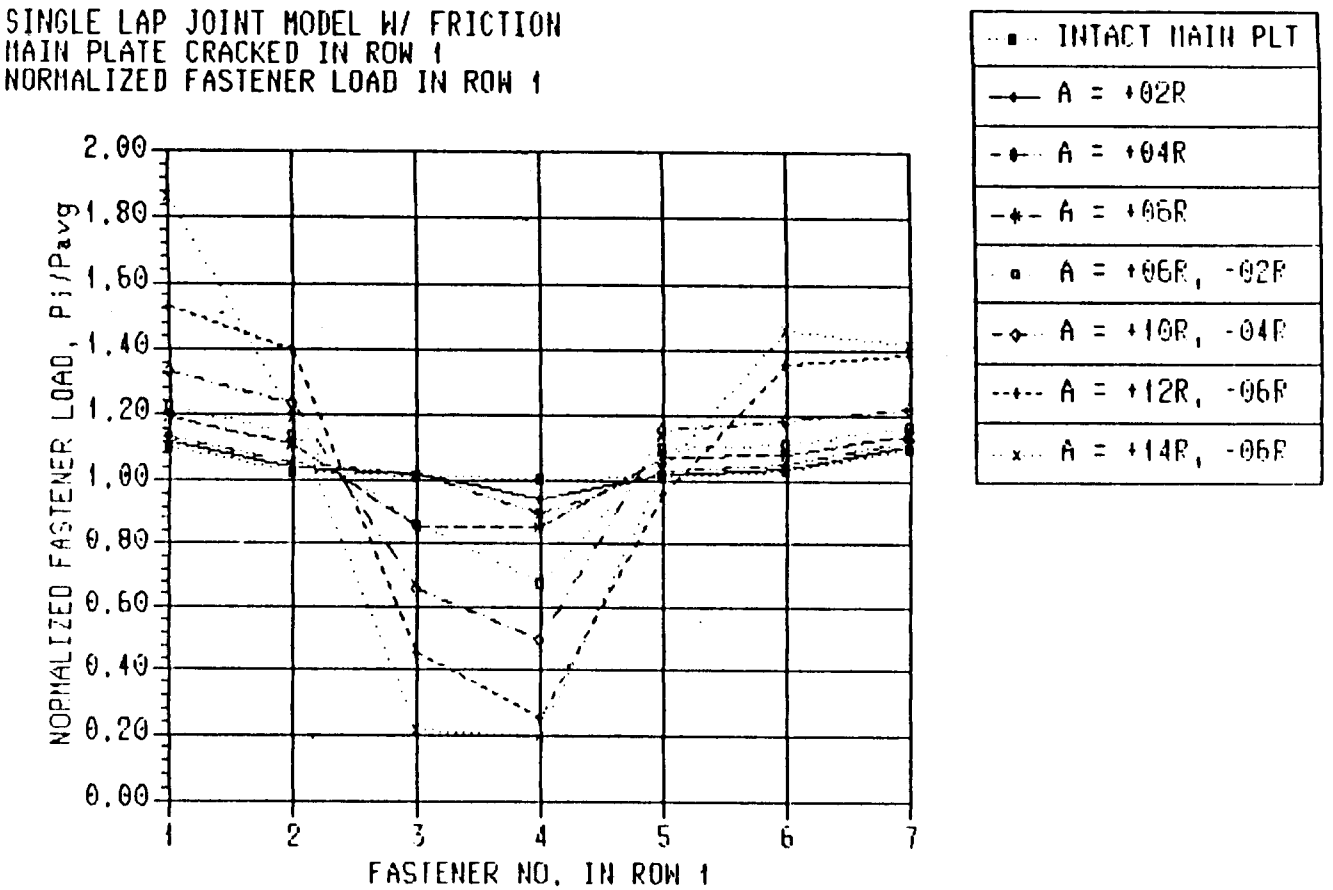

Figure 84. Fastener Load Distribution in Row 1
of Single-shear Lap-joint Specimen -- With Friction

The normalized fastener loads for fasteners No. 3 and 4 are curve-fitted into the following expressions as a function of A_1 and A_2.

$$\frac{P_4}{P_{AVG}} = 1.00163 - 0.02551 \frac{A_1}{R}, \qquad \text{for } \frac{A_1}{R} \leqslant 6 \tag{89}$$

$$\frac{P_4}{P_{AVG}} = [0.854 - 0.06752 (\frac{A_1}{R} - 8)] (1.0 + 0.09042 \frac{A_2}{R}), \qquad \text{for } \frac{A_1}{R} \geqslant 8 \text{ and } \frac{A_2}{R} \leqslant 6 \tag{90}$$

$$\frac{P_3}{P_{AVG}} = [0.8592 - 0.1072 (\frac{A_1}{R} - 8)] (1.0 - 0.005059 \frac{A_2}{R}), \qquad \text{for } \frac{A_1}{R} \geqslant 8 \text{ and } \frac{A_2}{R} \leqslant 6 \tag{91}$$

3.3.3 Double-Shear Lap-Joint Specimen

The procedure described in section 3.3.2 was used to analyze the fastener load distribution in the double-shear lap-joint specimens of Task IV-Structural Tests. Figure 85 shows the idealized double-shear lap-joint specimen being analyzed. Figure 86 shows the entire finite element mesh which is similar to Figure 80. The crack is located at fastener No. 4 of row 2 and grows toward fastener No. 3. The detail of row 2 is shown in Figure 87. Both doublers have cracks of equal length. The main plates are assumed to be intact. As in the single-shear lap-joint specimen, the fastener stiffness was modeled with one spring parallel and one spring perpendicular to the load direction. However, for the double-shear lap-joint specimen, two sets of spring elements are required to simulate one fastener. One set of spring elements connects a hole in the main plate with the corresponding hole in the top doubler; the other set of spring elements connects the same hole in main plate with the corresponding hole in the bottom doubler. Both sets of spring elements have the same spring constants since the doublers have equal thicknesses. The model shown in Figure 86 consists of 912 QUAD8 elements, 48 TRIA6 elements, 112 ELAS2 elements, 225 ROD elements and 3353 nodal points.

Table 13 shows the normalized fastener load distribution for the case without friction. In the table, the number within the parentheses corresponds to the hole which has an initial crack. For the case without friction, the spring constants for each row of fasteners are:

row 1 = 0.6520E6 lb/in.
row 2 = 0.9694E6 lb/in. (48.7% increase w.r.t. row 1)
row 3 = 0.6520E6 lb/in.
row 4 = 0.6520E6 lb/in.

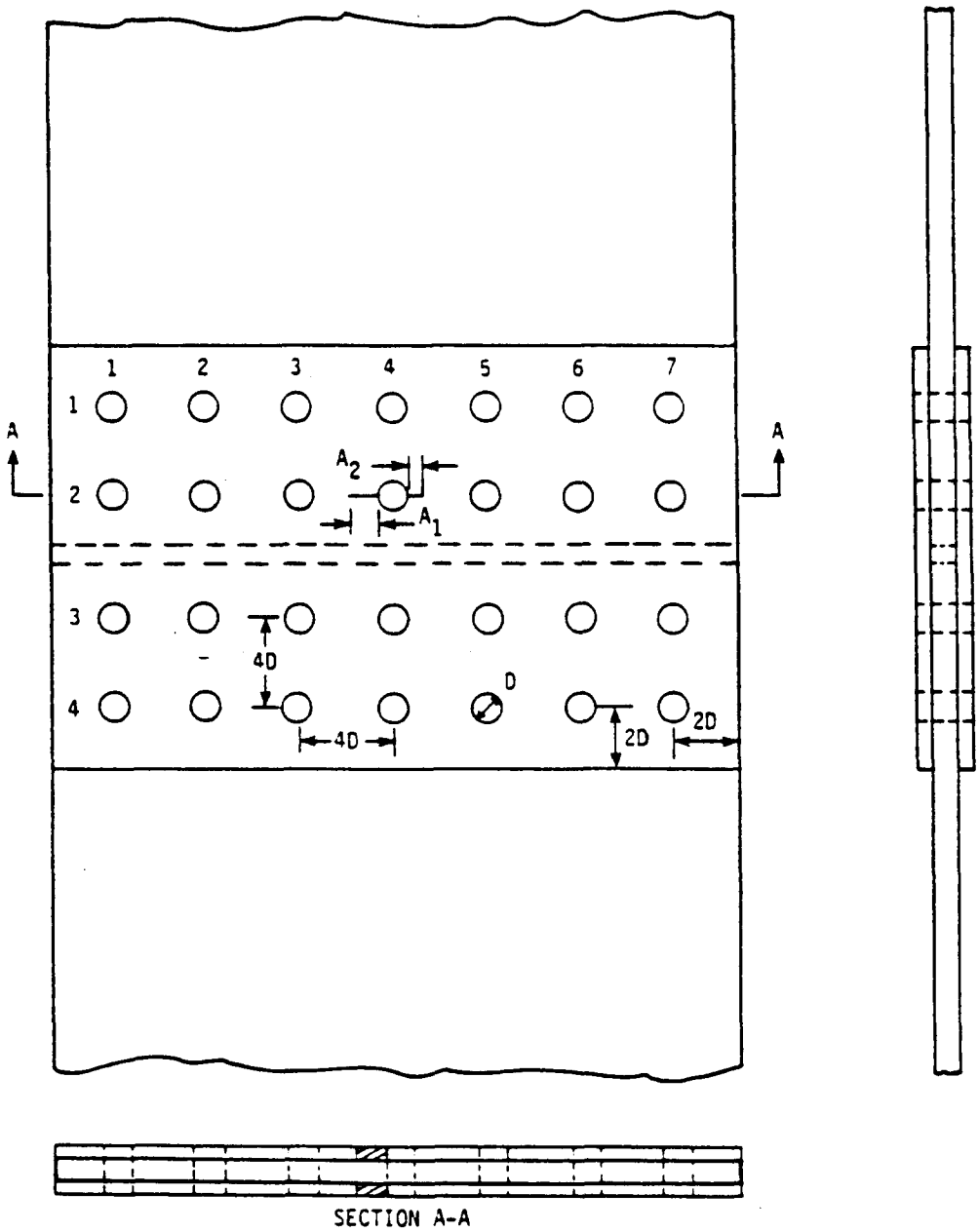

Figure 85. Double-shear Lap-Joint Specimen

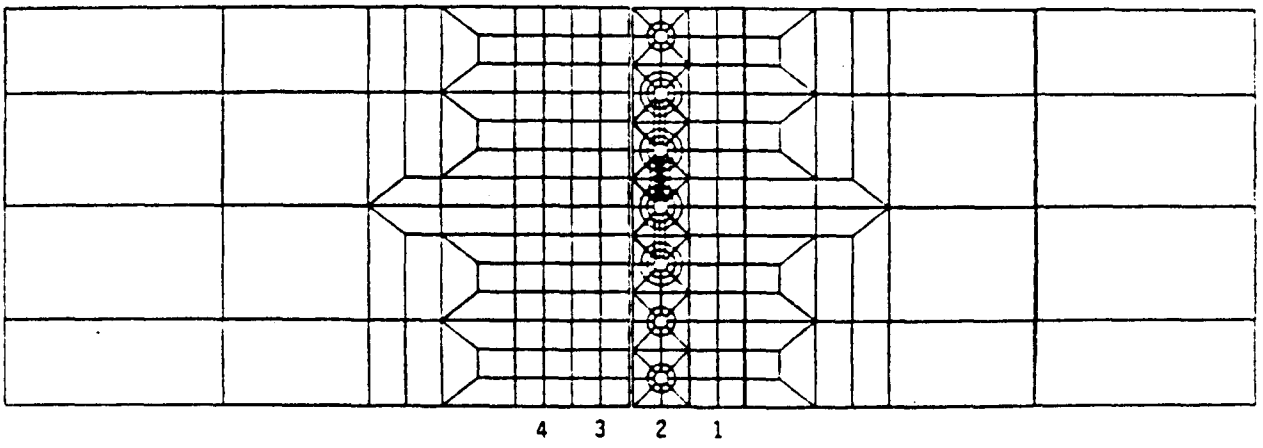

Figure 86. Finite Element Model for Double-shear Lap-joint Specimen

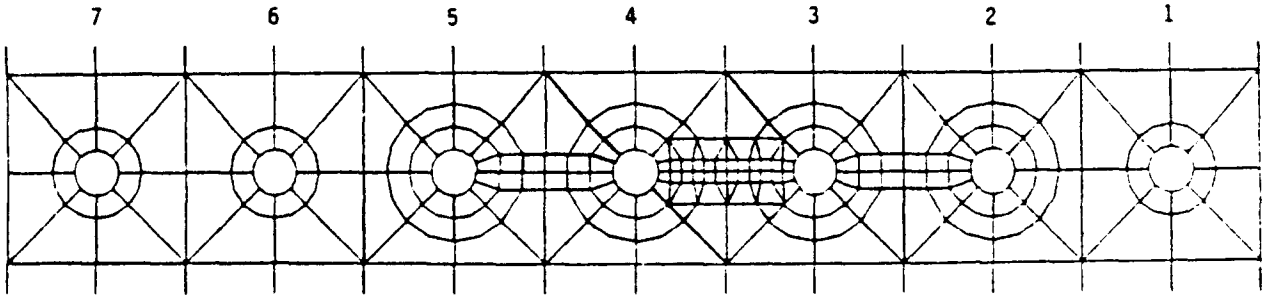

Figure 87. Detail of the Area Surrounding Row 2 Holes

TABLE 13. NORMALIZED FASTENER LOAD DISTRIBUTION OF DOUBLE-SHEAR LAP-JOINT SPECIMEN -- NO FRICTION

DOUBLE LAP JOINT MODEL W/O FRICTION
INTACT DOUBLERS, KX(2)=0.9694E6 (48.7% INCREASE)
NORMALIZED FASTENER LOADS, PI/PAVG, (PAVG = 1953.125 LBS.)

COL / ROW	1	2	3	4	5	6	7
1	1.0505	0.9863	0.9827	0.9835	0.9823	0.9867	1.0498
2	1.0473	0.9786	0.9752	(0.9751)	0.9748	0.9806	1.0467
3	-1.0440	-0.9869	-0.9798	-0.9790	-0.9799	-0.9874	-1.0438
4	-1.0430	-0.9839	-0.9814	-0.9828	-0.9814	-0.9838	-1.0429

DOUBLE LAP JOINT MODEL W/O FRICTION
BOTH DOUBLERS HAVING A CRACK LENGTH OF (+02R)
NORMALIZED FASTENER LOADS, PI/PAVG, (PAVG = 1953.125 LBS.)

COL / ROW	1	2	3	4	5	6	7
1	1.0580	0.9949	0.9822	0.9623	0.9875	0.9940	1.0551
2	1.0536	0.9877	0.9877	(0.9091)	0.9891	0.9880	1.0508
3	-1.0494	-0.9925	-0.9777	-0.9587	-0.9820	-0.9924	-1.0481
4	-1.0485	-0.9863	-0.9767	-0.9740	-0.9794	-0.9868	-1.0475

DOUBLE LAP JOINT MODEL W/O FRICTION
BOTH DOUBLERS HAVING A CRACK LENGTH OF (+04R)
NORMALIZED FASTENER LOADS, PI/PAVG, (PAVG = 1953.125 LBS.)

COL / ROW	1	2	3	4	5	6	7
1	1.0700	1.0043	0.9612	0.9254	0.9934	1.0029	1.0613
2	1.0640	1.0006	0.9915	(0.8692)	1.0038	0.9967	1.0556
3	-1.0581	-1.0007	-0.9678	-0.9355	-0.9868	-0.9989	-1.0531
4	-1.0569	-0.9890	-0.9682	-0.9626	-0.9783	-0.9910	-1.0531

DOUBLE LAP JOINT MODEL W/O FRICTION
BOTH DOUBLERS HAVING A CRACK LENGTH OF (+06R)
NORMALIZED FASTENER LOADS, PI/PAVG, (PAVG = 1953.125 LBS.)

COL / ROW	1	2	3	4	5	6	7
1	1.1169	1.0335	0.8702	0.8689	1.0207	1.0276	1.0754
2	1.1058	1.0587	0.8471	(0.8448)	1.0445	1.0198	1.0661
3	-1.0923	-1.0228	-0.9020	-0.8975	-1.0061	-1.0163	-1.0639
4	-1.0872	-0.9922	-0.9353	-0.9338	-0.9807	-1.0038	-1.0661

TABLE 13. NORMALIZED FASTENER LOAD DISTRIBUTION OF DOUBLER-SHEAR LAP-JOINT SPECIMEN -- NO FRICTION (CONT'D)

DOUBLE LAP JOINT MODEL W/O FRICTION
BOTH DOUBLERS HAVING A CRACK LENGTH OF (+10R)
NORMALIZED FASTENER LOADS, PI/PAVG, (PAVG = 1953.125 LBS.)

COL / ROW	1	2	3	4	5	6	7
1	1.1068	1.0147	0.8930	0.9301	1.0124	1.0133	1.0643
2	1.0990	1.0442	0.8078	(0.9300)	1.0214	1.0058	1.0571
3	-1.0841	-1.0060	-0.9086	-0.9400	-1.0006	-1.0063	-1.0552
4	-1.0770	-0.9841	-0.9449	-0.9541	-0.9848	-0.9977	-1.0567

DOUBLE LAP JOINT MODEL W/O FRICTION
BOTH DOUBLERS HAVING A CRACK LENGTH OF (+12R)
NORMALIZED FASTENER LOADS, PI/PAVG, (PAVG = 1953.125 LBS.)

COL / ROW	1	2	3	4	5	6	7
1	1.1384	0.9947	0.8343	0.9321	1.0273	1.0215	1.0657
2	1.1332	1.0627	0.7353	(0.9468)	1.0379	1.0131	1.0571
3	-1.1080	-1.0005	-0.8703	-0.9420	-1.0109	-1.0122	-1.0567
4	-1.0936	-0.9774	-0.9271	-0.9493	-0.9898	-1.0028	-1.0595

DOUBLE LAP JOINT MODEL W/O FRICTION
BOTH DOUBLERS HAVING A CRACK LENGTH OF (+14R)
NORMALIZED FASTENER LOADS, PI/PAVG, (PAVG = 1953.125 LBS.)

COL / ROW	1	2	3	4	5	6	7
1	1.2346	0.8979	0.7442	0.9594	1.0663	1.0382	1.0610
2	1.2626	0.9134	0.6704	(0.9975)	1.0783	1.0271	1.0491
3	-1.1769	-0.9375	-0.8091	-0.9610	-1.0377	-1.0237	-1.0534
4	-1.1348	-0.9507	-0.8883	-0.9482	-1.0058	-1.0133	-1.0597

Table 13 shows that the load distribution among the fastener rows is quite uniform in the intact joint. As shown in Table 13, analyses were made for crack lengths A_1 = 2R, 4R, 6R, 10R, 12R, and 14R. The crack lengths A_1 = 6R and 14R correspond to one and two ligments broken. The data in Table 13 are plotted in Figure 88 to show the change of row 2 fastener loads for various crack lengths. Compared to the single-shear lap-joint specimen, there is quite a substantial load variation in rows 3 and 4. This effect occurs because rows 3 and 4 are closer to the local loss of stiffness due to crack growth in row 2 than they are in the single-shear lap-joint specimen. The normalized fastener loads for fasteners No's. 4 and 3 are curve-fitted into the following expressions.

$$\frac{P_4}{P_{AVG}} = 0.96417 - 0.02154 \frac{A_1}{R}, \qquad \text{for } \frac{A_1}{R} \leqslant 6 \tag{92}$$

$$\frac{P_4}{P_{AVG}} = 0.85854 + 0.023745 \left(\frac{A_1}{R} - 8\right), \qquad \text{for } \frac{A_1}{R} \geqslant 8 \tag{93}$$

$$\frac{P_3}{P_{AVG}} = 0.85554 - 0.03013 \left(\frac{A_1}{R} - 8\right), \qquad \text{for } \frac{A_1}{R} \geqslant 8 \tag{94}$$

For the case with friction, the spring constant for each row of fasteners are:

row 1	=	0.6520E6	lb/in.
row 2	=	0.7277E6	lb/in. (11.6% increase w.r.t. row 1)
row 3	=	0.6520E6	lb/in.
row 4	=	0.6520E6	lb/in.

Seven models corresponding to the seven combinations of crack lengths shown on page 96 have been analyzed. It should be mentioned that there are two pairs of faying surfaces associated with a fastener. Therefore, the total frictional force in the double-shear lap-joints is twice that in the single-shear lap-joints. Table 14 shows the normalized fastener load distribution for various crack lengths. The data in Table 14 are plotted in Figure 89 for the row 2 fasteners. The figure shows that there are substantial changes in fastener loads as the crack grows. Table 14 show that the loads of fastener Nos. 3 and 4 in rows 1 and 2 drop to almost zero after two ligments are broken. This phenomenon is similar to

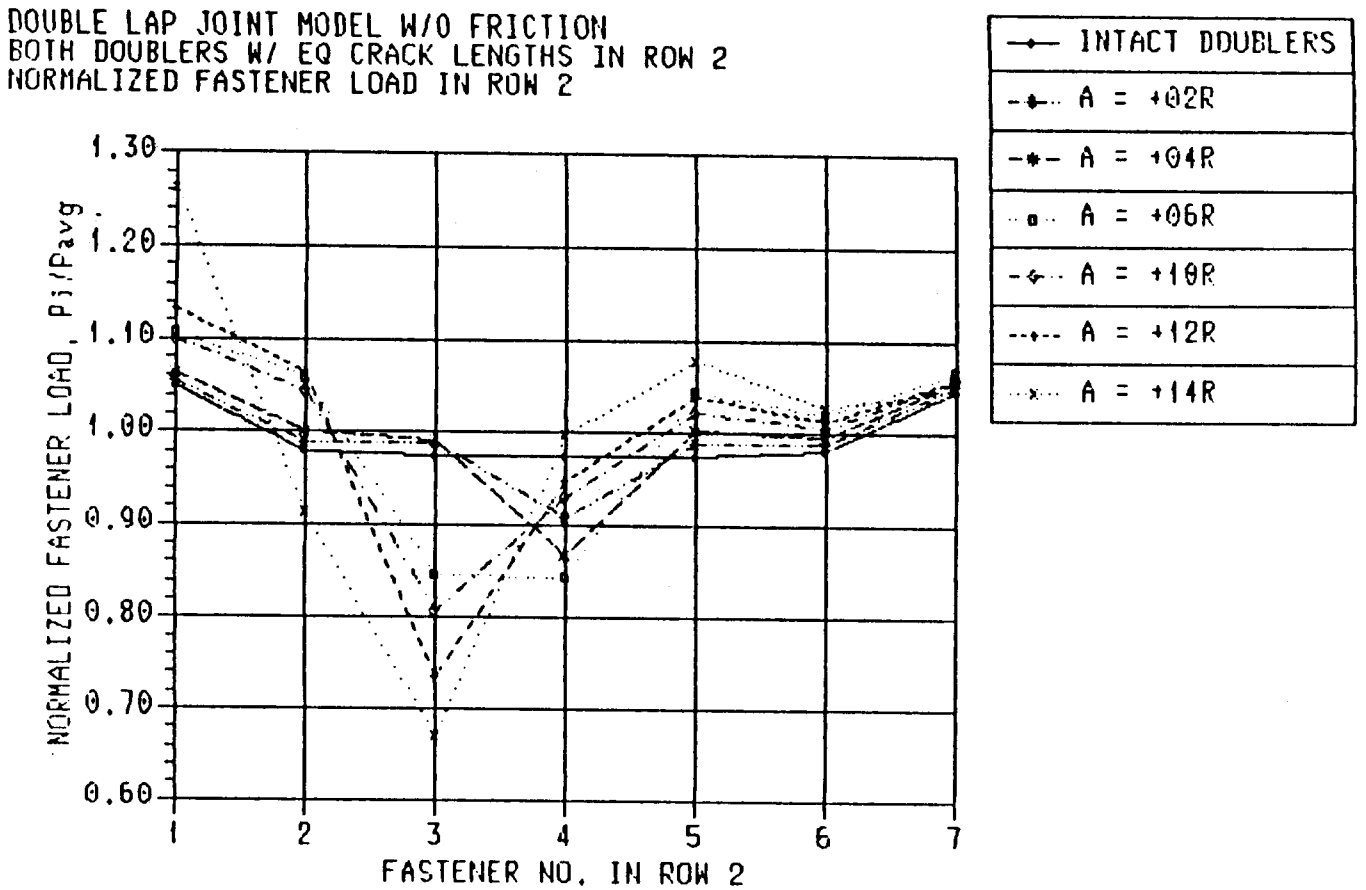

Figure 88. Fastener Load Distribution in Row 2
of Double-shear Lap-joint Specimen -- No Friction

TABLE 14. NORMALIZED FASTENER LOAD DISTRIBUTION OF DOUBLE-SHEAR LAP-JOINT SPECIMEN--WITH FRICTION

DOUBLE LAP JOINT MODEL W/ FRICTION
INTACT DOUBLERS, KX(2)=0.7277E6 (11.6% INCREASE)
NORMALIZED FASTENER LOADS, PI/PAVG, (PAVG = 1906.250 LBS.)

COL / ROW	1	2	3	4	5	6	7
1	1.0933	0.9634	0.9562	0.9581	0.9560	0.9674	1.0940
2	1.0840	0.9600	0.9523	(0.9518)	0.9519	0.9679	1.0846
3	-1.0891	-0.9733	-0.9596	-0.9580	-0.9598	-0.9738	-1.0889
4	-1.0878	-0.9665	-0.9620	-0.9651	-0.9620	-0.9663	-1.0877

DOUBLE LAP JOINT MODEL W/ FRICTION
BOTH DOUBLERS HAVING A CRACK LENGTH OF (+02R)
NORMALIZED FASTENER LOADS, PI/PAVG, (PAVG = 1906.250 LBS.)

COL / ROW	1	2	3	4	5	6	7
1	1.1062	0.9784	0.9551	0.9198	0.9638	0.9802	1.1037
2	1.0943	0.9740	0.9708	(0.8509)	0.9726	0.9795	1.0916
3	-1.0982	-0.9827	-0.9555	-0.9242	-0.9638	-0.9822	-1.0959
4	-1.0971	-0.9705	-0.9539	-0.9505	-0.9589	-0.9714	-1.0953

DOUBLE LAP JOINT MODEL W/ FRICTION
BOTH DOUBLERS HAVING A CRACK LENGTH OF (+04R)
NORMALIZED FASTENER LOADS, PI/PAVG, (PAVG = 1906.250 LBS.)

COL / ROW	1	2	3	4	5	6	7
1	1.1294	0.9969	0.9173	0.8506	0.9743	0.9970	1.1158
2	1.1116	0.9959	0.9772	(0.7844)	0.9962	0.9943	1.1001
3	-1.1144	-0.9973	-0.9367	-0.8823	-0.9731	-0.9941	-1.1048
4	-1.1127	-0.9752	-0.9380	-0.9298	-0.9572	-0.9792	-1.1052

DOUBLE LAP JOINT MODEL W/ FRICTION
BOTH DOUBLERS HAVING A CRACK LENGTH OF (+06R)
NORMALIZED FASTENER LOADS, PI/PAVG, (PAVG = 1906.250 LBS.)

COL / ROW	1	2	3	4	5	6	7
1	1.2166	1.0485	0.7495	0.7472	1.0243	1.0427	1.1421
2	1.1815	1.0871	0.7467	(0.7426)	1.0615	1.0326	1.1179
3	-1.1747	-1.0373	-0.8211	-0.8132	-1.0068	-1.0250	-1.1245
4	-1.1663	-0.9816	-0.8799	-0.8780	-0.9609	-1.0019	-1.1289

TABLE 14. NORMALIZED FASTENER LOAD DISTRIBUTION OF DOUBLE-SHEAR LAP-JOINT SPECIMEN -- WITH FRICTION (CONT'D)

DOUBLE LAP JOINT MODEL W/ FRICTION
BOTH DOUBLERS HAVING A CRACK LENGTH OF (+06R,-02R)
NORMALIZED FASTENER LOADS, PI/PAVG, (PAVG = 1906.250 LBS.)

COL / ROW	1	2	3	4	5	6	7
1	1.2591	1.0896	0.7291	0.6294	1.0381	1.0880	1.1769
2	1.2136	1.1323	0.7650	(0.4800)	1.1223	1.0737	1.1437
3	-1.2034	-1.0679	-0.8098	-0.7103	-1.0060	-1.0536	-1.1515
4	-1.1957	-0.9963	-0.8597	-0.8302	-0.9423	-1.0164	-1.1569

DOUBLE LAP JOINT MODEL W/ FRICTION
BOTH DOUBLERS HAVING A CRACK LENGTH OF (+10R,-04R)
NORMALIZED FASTENER LOADS, PI/PAVG, (PAVG = 1906.250 LBS.)

COL / ROW	1	2	3	4	5	6	7
1	1.4038	1.1772	0.5690	0.3942	1.0250	1.1781	1.2516
2	1.3303	1.2813	0.4753	(0.2777)	1.2179	1.1619	1.1977
3	-1.3038	-1.1226	-0.6815	-0.5586	-1.0131	-1.1195	-1.2030
4	-1.2839	-1.0078	-0.7826	-0.7371	-0.9204	-1.0534	-1.2126

DOUBLE LAP JOINT MODEL W/ FRICTION
BOTH DOUBLERS HAVING A CRACK LENGTH OF (+12R,-06R)
NORMALIZED FASTENER LOADS, PI/PAVG, (PAVG = 1906.250 LBS.)

COL / ROW	1	2	3	4	5	6	7
1	1.6739	1.2715	0.2773	0.0000	0.7714	1.3758	1.4745
2	1.5558	1.5192	0.2526	(0.1141)	0.9410	1.4197	1.3673
3	-1.4991	-1.2196	-0.5122	-0.2813	-0.8623	-1.2682	-1.3592
4	-1.4560	-1.0431	-0.6613	-0.5385	-0.8174	-1.1162	-1.3656

DOUBLE LAP JOINT MODEL W/ FRICTION
BOTH DOUBLERS HAVING A CRACK LENGTH OF (+14R,-06R)
NORMALIZED FASTENER LOADS, PI/PAVG, (PAVG = 1906.250 LBS.)

COL / ROW	1	2	3	4	5	6	7
1	2.0889	0.9896	0.0000	0.0000	0.8606	1.5109	1.5320
2	2.0053	1.1986	0.1110	(0.1034)	1.0626	1.5472	1.3983
3	-1.7924	-1.0807	-0.2318	-0.1994	-0.9274	-1.3620	-1.4045
4	-1.6570	-0.9785	-0.4806	-0.4470	-0.8370	-1.1784	-1.4233

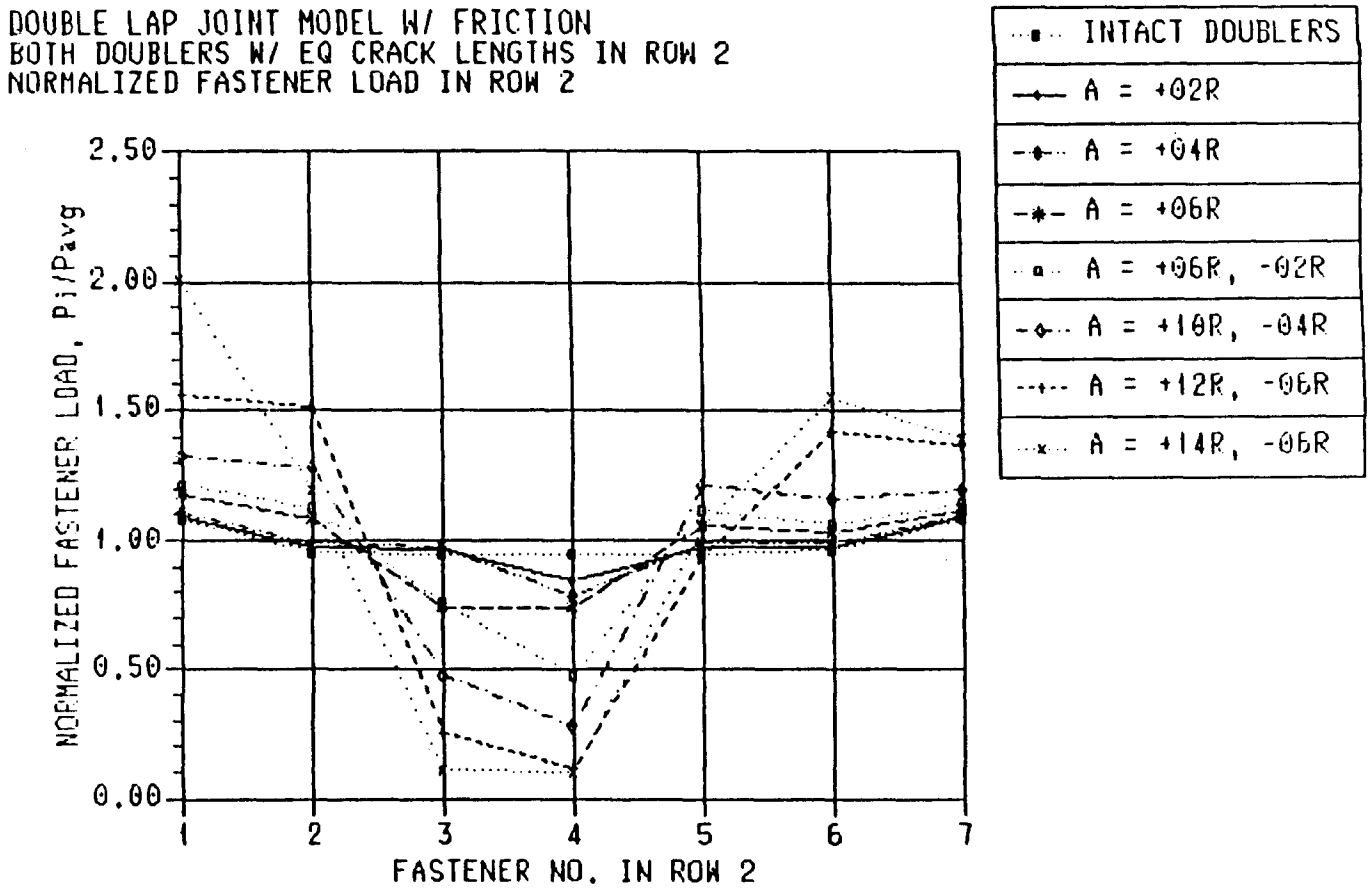

Figure 89. Fastener Load Distribution in Row 2
of Double-Shear Lap-joint Specimen -- with Friction

that observed in the single-shear lap-joint specimen. When the cracks become long enough, fastener Nos. 3 and 4 in rows 1 and 2 transfer very little of the applied load due to the local loss of stiffness. The slight load transfer in these fasteners was almost negated by the faying surface frictional forces. The normalized fastener loads for fastener Nos. 3 and 4 are curve-fitted into the following expressions.

$$\frac{P_4}{P_{AVG}} = 0.93654 - 0.034705 \frac{A_1}{R} \qquad \text{for } \frac{A_1}{R} \leqslant 6 \tag{95}$$

$$\frac{P_4}{P_{AVG}} = [0.7426 - 0.02815 (\frac{A_1}{R} - 8)] (1.0 + 0.1408 \frac{A_2}{R}), \quad \text{for } \frac{A_1}{R} \geqslant 8 \text{ and } \frac{A_2}{R} \leqslant 6 \tag{96}$$

$$\frac{P_3}{P_{AVG}} = [0.7467 - 0.1079 (\frac{A_1}{R} - 8)] (1.0 + 0.01888 \frac{A_2}{R}), \quad \text{for } \frac{A_1}{R} \geqslant 8 \text{ and } \frac{A_2}{R} \leqslant 6 \tag{97}$$

4.0 STRESS CONCENTRATION FACTORS

According to Equations (2) and (3), the stress concentration factors due to remote stress (K_{tg}) and fastener load (K_{tb}), are required to calculate stress severity factor, k, which is used in the crack initiation analysis. The k_{tg} and k_{tb} for the pertinent configurations are given in section 4.1. These configurations are applicable to all the members in a specimen assembly for all Task IV structural test specimens.

In view of the similarity between the stress intensity factor and the stress concentration factor, the compounded solution method is also adopted to obtain stress concentration factors. The correction factors to account for various structural boundaries are considered to be the same as those for stress intensity factors. The two-dimensional finite element analyses were performed to validate some of the stress concentration factors obtained by the compounded solution method.

4.1 The k_{tg} and k_{tb} for Pertinent Configurations

4.1.1 A Circular Hole

The k_{tg} for a circular hole, as shown in Figure 90, is given in Equation (98).

$$k_{tg\text{-}1} = 3.0 \cdot CR_{fwa(b)} \tag{98}$$

where $CR_{fwa(b)}$ is the finite width correction factor as given in Equations (66a) and (66b). Note that the "a" in Figure 31-a shall be replaced by "R" in Figure 90.

The case of the bearing stress concentration factor due to fastener load (k_{tb}), as shown in Figure 91, was investigated by performing several finite element analyses to obtain a realistic solution. A detailed description of the finite element analysis and discussion regarding to the current solution is given in Section 4.2. The results are summarized below. Equation (99) shows that for $E/D \gg 2$, k_{tb-1} equals 0.8349 for an infinite plate. This result is in contrast to the common belief that as the plate width approaches infinity, the value of k_{tb-1} approaches 1.0.

$$k_{tb\text{-}1} = 0.8349 + 1.6286\left(\frac{d}{w}\right) - 0.07077\left(\frac{d}{w}\right)^2 + 3.8666\left(\frac{d}{w}\right)^3, \qquad \frac{E}{D} >> 2 \tag{99}$$

$$k_{tb\text{-}1} = 1.2069 + 0.7599\left(\frac{d}{w}\right) - 1.4748\left(\frac{d}{w}\right)^2 + 7.1797\left(\frac{d}{w}\right)^3, \qquad \frac{E}{D} = 2 \tag{100}$$

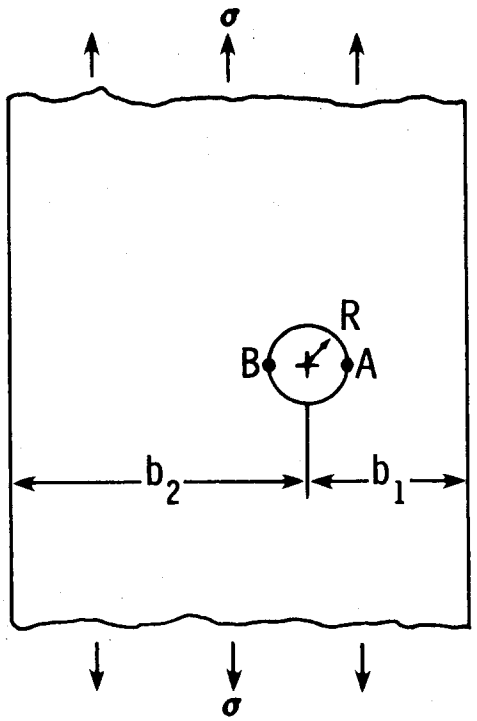

Figure 90. Hole in Finite Plate - Remote Stress

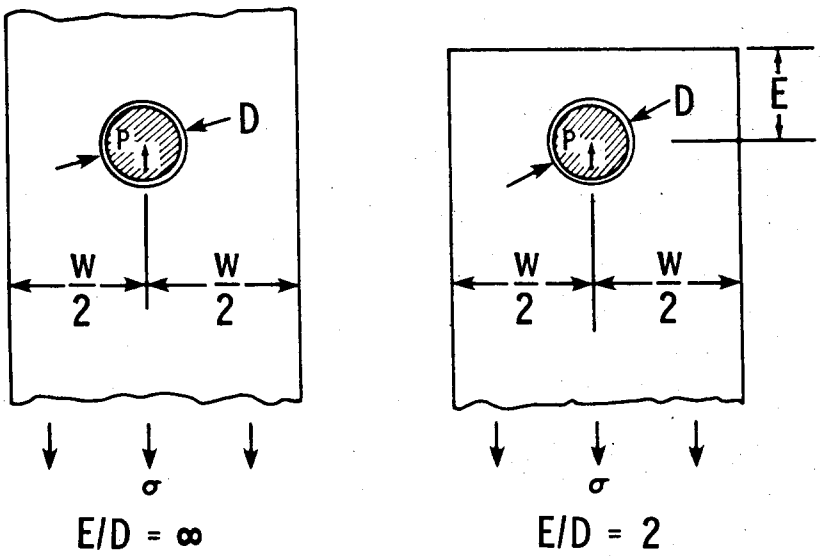

Figure 91. Hole in Finite Plate - Fastener Load

4.1.2 A Circular Hole With A Crack

The configuration shown in Figure 92 can be modeled as an ellipse.

$$k_{tg\text{-}2} = (1 + 2\sqrt{A/R}) \cdot CR_{shape} \cdot CR_{fwb} \tag{101}$$

$$CR_{shape} = 1 + \frac{1}{6}\left[\frac{2}{\pi} \operatorname{Sin}^{-1}\left(1 - \frac{R}{A}\right)\right]^3 \tag{102}$$

where CR_{fwb} is the finite width correction factor and is available from Equation (66) And (102) given by Brussat et al (Ref. 3). CR_{shape} is to account for the difference between an ellipse and a cracked hole.

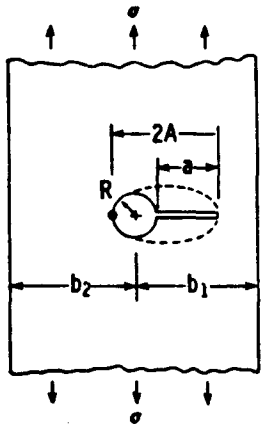

Figure 92. Cracked Fastener Hole in Finite Plate - Remote Stress

For the case of fastener load shown in Figure 93, the similarity shown in Figure 94 can be applied to obtain k_{tb} for Figure 93. The relationship among the configurations shown in Figure 94 is given in Equation (103). The desired k_{tb} is given in Equation (104).

$$\frac{(k_{tb})_A}{(k_{tb})_C} = \frac{K_B}{K_D} \tag{103}$$

$$k_{tb\text{-}2} = (k_{tb})_A = \left(\frac{K_B}{K_D}\right)(k_{tb})_C \tag{104}$$

where K_B and K_D are available from page 2.32 of Ref. 20, and $(k_{tb})_C$ is given in Equation (99) for $E/D \gg 2$ and Equation (100) for $E/D = 2$.

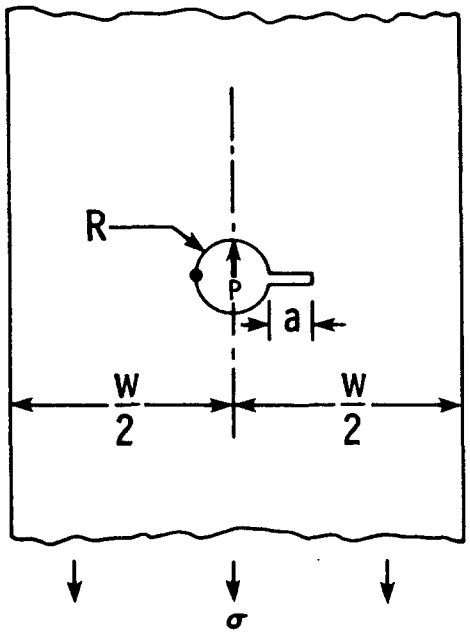

Figure 93. Cracked Fastener Hole in Finite Plate - Fastener Load

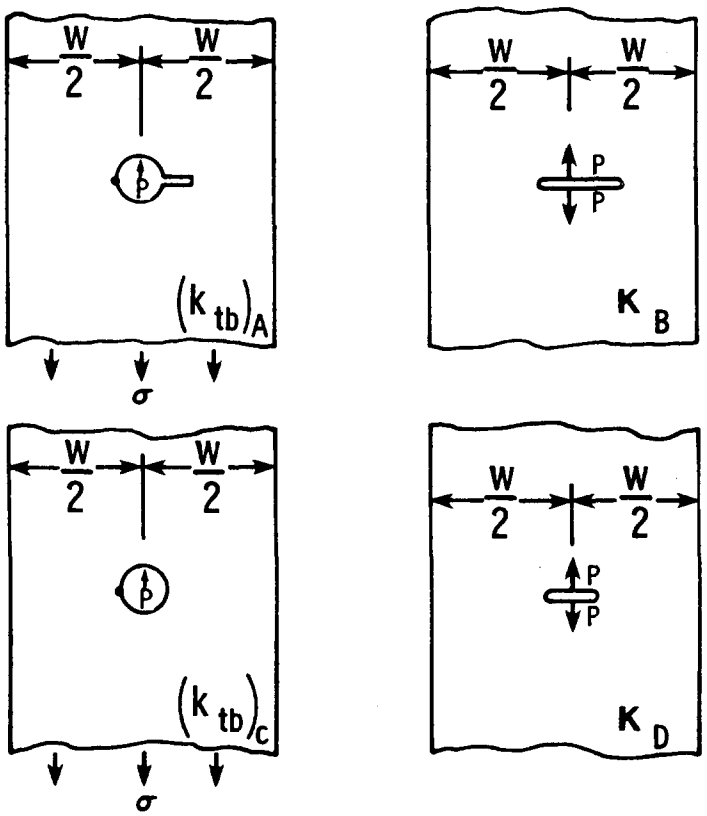

Figure 94. Illustration of Similarity for Figure 93

4.1.3 Two Holes Connected By A Slot

The k_{tg} for the problem of two holes connected by a slot under remote stress, as shown in Figure 95, was obtained by Brussat et al (Ref. 3) using the compounded solution method. This solution was verified to be accurate with the finite element analysis in this investigation. The k_{tg} is further modified herein to account for the eccentricity as shown in Figure 31-a.

$$k_{tg\text{-}3} = (1 + 2\sqrt{A/R}) \cdot (\sec \frac{\pi A}{W})^{\sqrt{R/4A}} \cdot CR_{fwa(b)} \tag{105}$$

where $CR_{fwa(b)}$ is available from Equations (66a) and (66b) for the finite width correction.

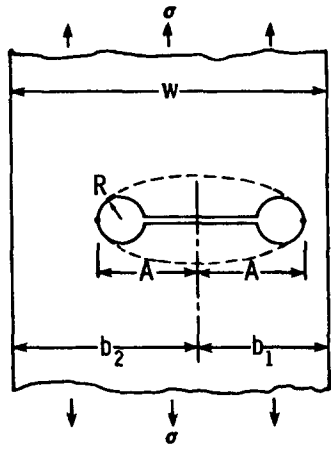

Figure 95. Two Holes Connected By A Slot - Remote Stress

For the case of fastener load shown in Figure 96, the similarity principle shown in Figure 97 is used to obtain k_{tb}.

$$\frac{(k_{tb})_A}{K_C} = \frac{(k_{tb})_B}{K_D} \tag{106}$$

$$k_{tb\text{-}3} = (k_{tb})_A = (\frac{K_C}{K_D})(k_{tb})_B \tag{107}$$

where K_C and K_D are available from Ref. 20, and $(k_{tb})_B$ is available from Equation (99) for $E/D \gg 2$ and Equation (100) for $E/D = 2$. Several finite element analyses (described in Section 4.2.2) were performed to validate Equation (107). The results from the compounded solution method are within 11.8% higher than that from the FEM as shown in Table 17. It needs to be mention that Equation (107) is for load P only. Superposition principle needs to be applied to obtain $k_{tb\text{-}3}$ due to both P_1 and P_2 shown in Figure 96.

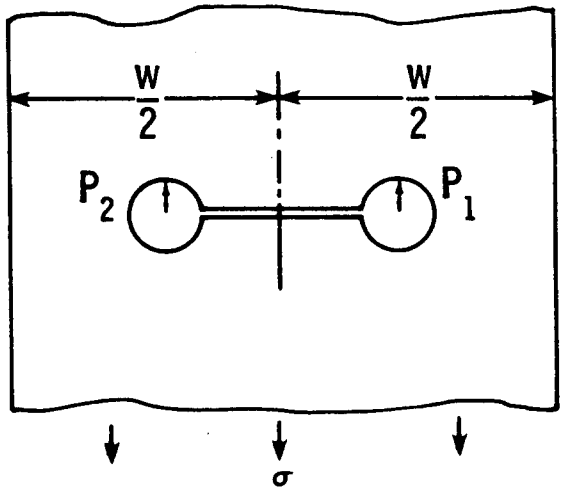

Figure 96. Two Holes Connected By A Slot - Fastener Loads

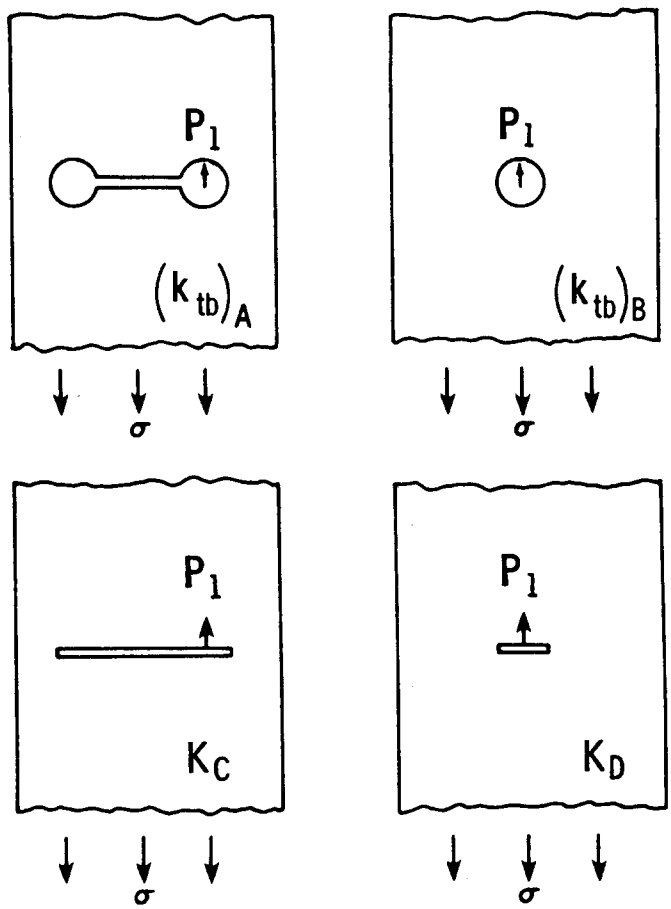

Figure 97. Illustration of Similarity for Figure 96

4.1.4 A Crack Emanating From An Internal Notch

The configuration for a crack emanating from an internal notch under remote stress, as shown in Figure 98, can be modeled as an ellipse. Equation (101) is applicable to this configuration.

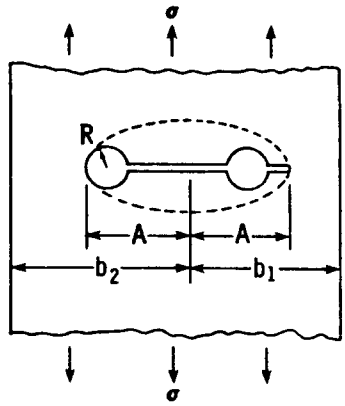

Figure 98. Crack Emanating From An Internal Notch - Remote Stress

For the case of fastener loads, as shown in Figure 99, the similarity illustrated in Figure 100 was used to obtain k_{tb}. In this case, Equation (107) is applicable.

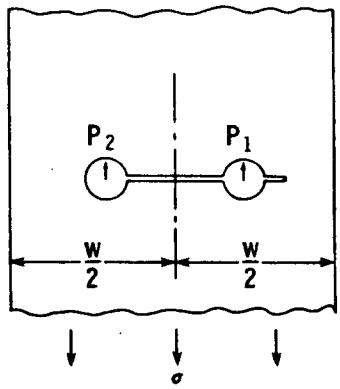

Figure 99. Crack Emanating From An Internal Notch - Fastener Loads

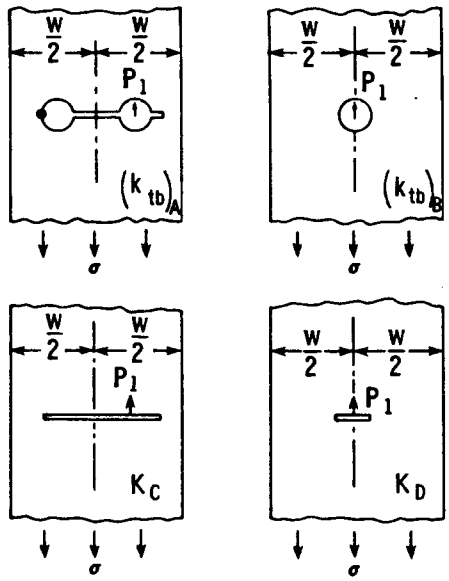

Figure 100. Illustration of Similarity for Figure 99

4.1.5. An Edge Notch

The k_{tg} for an edge notch in a semi-infinite plate is given on page 19.13 of Ref. 20. The solution is modified with the finite width correction factor to obtain k_{tg} for Figure 101.

$$k_{tg-4} = (1 + 2\sqrt{A/R}) \cdot \left[1 + 0.122 \left(\frac{1}{1 + c/a}\right)^{2.5}\right] \frac{CR_{fweg}}{CR_{sweg}} \tag{108}$$

where CR_{fweg} and CR_{sweg} are given in Equations (70) and (72), respectively.

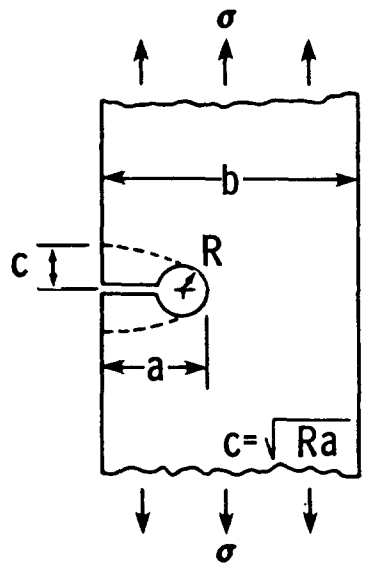

Figure 101. Edge Notch - Remote Stress

4.1.6 Fastener Tilting and Deflection

Barrois (Ref. 27) has used beam on elastic foundation theory and Timoshenko's beam theory to solve the stress concentration factor due to fastener tilting and deflection (K_{td}). He has given a system of simultaneous equations as a function of plate thickness, Young's moduli, fastener diameter and Poisson's ratio. The effect of shear force on beam deflection is considered in Timoshenko's beam theory, whereas it is not considered in conventional beam theory. Unless shear forces in short beams are considered, beam on elastic foundation theory will provide unconservative values of k_{td}. It is noted that shear forces have an insignificant effect on long beams.

The Barrois method was used to calculate k_{td} for various combinations of thicknesses in the lap-joints shown in Figure 102. The calculation was based on aluminum plates and steel fasteners. The calculated k_{td} are shown in Table 15 along with the data reported in Ref.3. In general, Barrois's method gives higher values of k_{td} than Ref. 3. This is expected as a consequence of Timoshenko's beam theory.

TABLE 15. COMPARISON OF k_{td}

Single-Shear					
		k_{td} for Plate 1		k_{td} for Plate 2	
t_2/t_1	t_1/d	Ref. 3	This Study	Ref. 3	This Study
1.0	0.50	1.05	1.15	1.05	1.15
1.0	0.60	1.09	1.24	1.09	1.24
1.0	0.75	1.21	1.44	1.21	1.44
1.0	1.00	1.50	1.98	1.50	1.98
0.75	1.00	1.43	1.88	1.23	1.49
0.53	1.00	1.35	1.77	1.06	1.21

Double-Shear					
		k_{td} for Plate 1		k_{td} for Plate 2	
$2t_2/t_1$	t_1/d	Ref. 3	This Study	Ref. 3	This Study
1.0	0.75	1.04	1.07	1.04	1.07
1.0	1.00	1.07	1.16	1.07	1.16

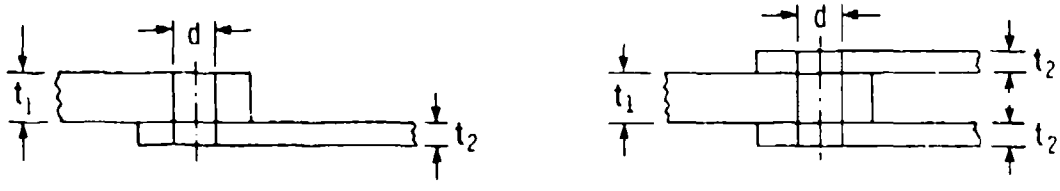

Figure 102. Single-shear and Double-shear Lap-joints

The Barrois method was used to calculate k_{td} for various combinations of thicknesses in the lap-joints shown in Figure 102. The calculation was based on aluminum plates and steel fasteners. The calculated k_{td} are shown in Table 15 along with the data reported in Ref.3. In general, Barrois's method gives higher values of k_{td} than Ref. 3. This is expected as a consequence of Timoshenko's beam theory.

TABLE 15. COMPARISON OF k_{td}

Single-Shear					
		k_{td} for Plate 1		k_{td} for Plate 2	
t_2/t_1	t_1/d	Ref. 3	This Study	Ref. 3	This Study
1.0	0.50	1.05	1.15	1.05	1.15
1.0	0.60	1.09	1.24	1.09	1.24
1.0	0.75	1.21	1.44	1.21	1.44
1.0	1.00	1.50	1.98	1.50	1.98
0.75	1.00	1.43	1.88	1.23	1.49
0.53	1.00	1.35	1.77	1.08	1.21

Double-Shear					
		k_{td} for Plate 1		k_{td} for Plate 2	
$2t_2/t_1$	t_1/d	Ref. 3	This Study	Ref. 3	This Study
1.0	0.75	1.04	1.07	1.04	1.07
1.0	1.00	1.07	1.16	1.07	1.16

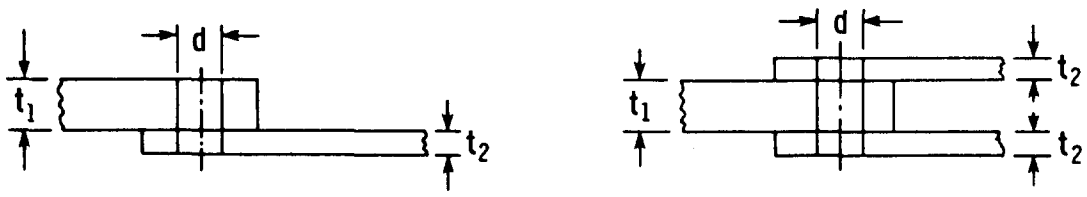

Figure 102. Single-shear and Double-shear Lap-joints

4.2 The Finite Element Analysis of A Loaded Hole

4.2.1 A Single Hole

The stress concentration factor, k_{tb}, due to fastener load, shown in Figure 91, was analyzed with the 2-D FEM. The 8-noded quadratic quadrilateral isoparametric element, QUAD8 in MSC/NASTRAN, was used in the analysis. The interface between the fastener and hole was realistically treated using an iteration procedure to determine the actual contact point. The "multiple point constraint" technique in MSC/NASTRAN was employed to simulate the interface. The load was applied to the center of the fastener.

Analyses were performed for two E/D ratios and various D/W ratios. Figures 103 and 104 show examples of the FEM models. The shaded region represents the fastener. There is no clearance between the hole and fastener. The results are shown in Table 16. In the table, k_{tb-max} is defined as the maximum principal stress divided by the average bearing pressure and k_{tb-90o} is defined as the principal stress at $\theta = 90^o$ divided by the average bearing pressure. The numerical results have been curve-fitted into two expressions as shown in Equations (99) and (100). Except for the case of D/W = 0.5, k_{tb-max} occurs at $\theta = 90^o$; thus, k_{tb-max} equals k_{tb-90o}. For D/W = 0.5, k_{tb-max} occurs at 95.625^o; k_{tb-max} is slightly larger than k_{tb-90o}. The E/D ratio has a great effect on the k_{tb} as indicated in Table 16. However, the effect of E/D diminishes when D/W is larger than 0.375.

Analyses were also performed to investigate the effect of loading on k_{tb}. Figure 105 shows the models used in the analysis. The hole in Figure 105-a and 105-b is subjected to a uniform internal pressure on a half circle to simulate the fastener load. The hole in Figure 105-c is subjected to a uniform internal pressure on the entire circle. The k_{tb} for each case is shown in Table 16. It is interesting to observe that (i) for Figures 105-a and 105-b, k_{tb-max} is much larger than k_{tb-90o}; (ii) for the same D/W ratios, the k_{tb-90o} for the uniform internal pressure case is much smaller than the k_{tb-90o} for actual fastener loading and; (iii) for actual fastener loading, the k_{tb-max} is the same as the k_{tb-90o}. For the case of Figure 105-c, the k_{tb} is 1.006 which is very close to the theoretical value 1.00.

The FEM result of k_{tb-90o} for Figures 105-a and 105-b can also be obtained by the superposition principle shown in Figure 106. For the case of an infinite plate, the reactive remote stress in Figure 106 approaches zero; accordingly, the k_{tb-90o} equals 0.5.

However, FEM results (Table 16) indicate that the k_{tb-90o} for actual fastener loading is 0.917 for the case of D/W = 0.05 which approaches an infinite plate. Therefore, the uniform internal pressure shown in Figure 106 is not appropriate to simulate the fastener loading for determining k_{tb} mainly because of the fastener-hole contact problem involved. The important point to be emphasized is that the prevailing concept of k_{tb-90o} being equal to 1.0 for an infinite plate is misleading.

TABLE 16. FEM RESULTS OF k_{tb} FOR A SINGLE HOLE

D/W	E/D	k_{tb-max}	θ_{max} (degree)	k_{tb-90o}	k_{tb-90o}(Ref. 27)
Actual Fastener - Hole Contact (Figures 103 and 104)					
0.050	32	0.917	90°	0.917	1.055
	2	1.244	90°	1.244	
0.125	32	1.044	90°	1.044	1.161
	2	1.285	90°	1.285	
0.167	32	1.123	90°	1.123	1.234
	2	1.333	90°	1.333	
0.250	32	1.299	90°	1.299	1.417
	2	1.417	90°	1.417	
0.375	32	1.639	90°	1.639	1.825
	2	1.662	90°	1.662	
0.500	32	2.130	95.625°	2.115	2.5
	2	2.131	95.625°	2.116	
Uniform Internal Pressure on Half-Circle (Figures 105-a and 105-b)					
0.050	32	0.942	95.625°	0.579	
0.167	32	1.133	95.625°	0.768	
Uniform Internal Pressure on Entire Circle (Figure 105-c)					
0.050	32	1.006	90°	1.006	

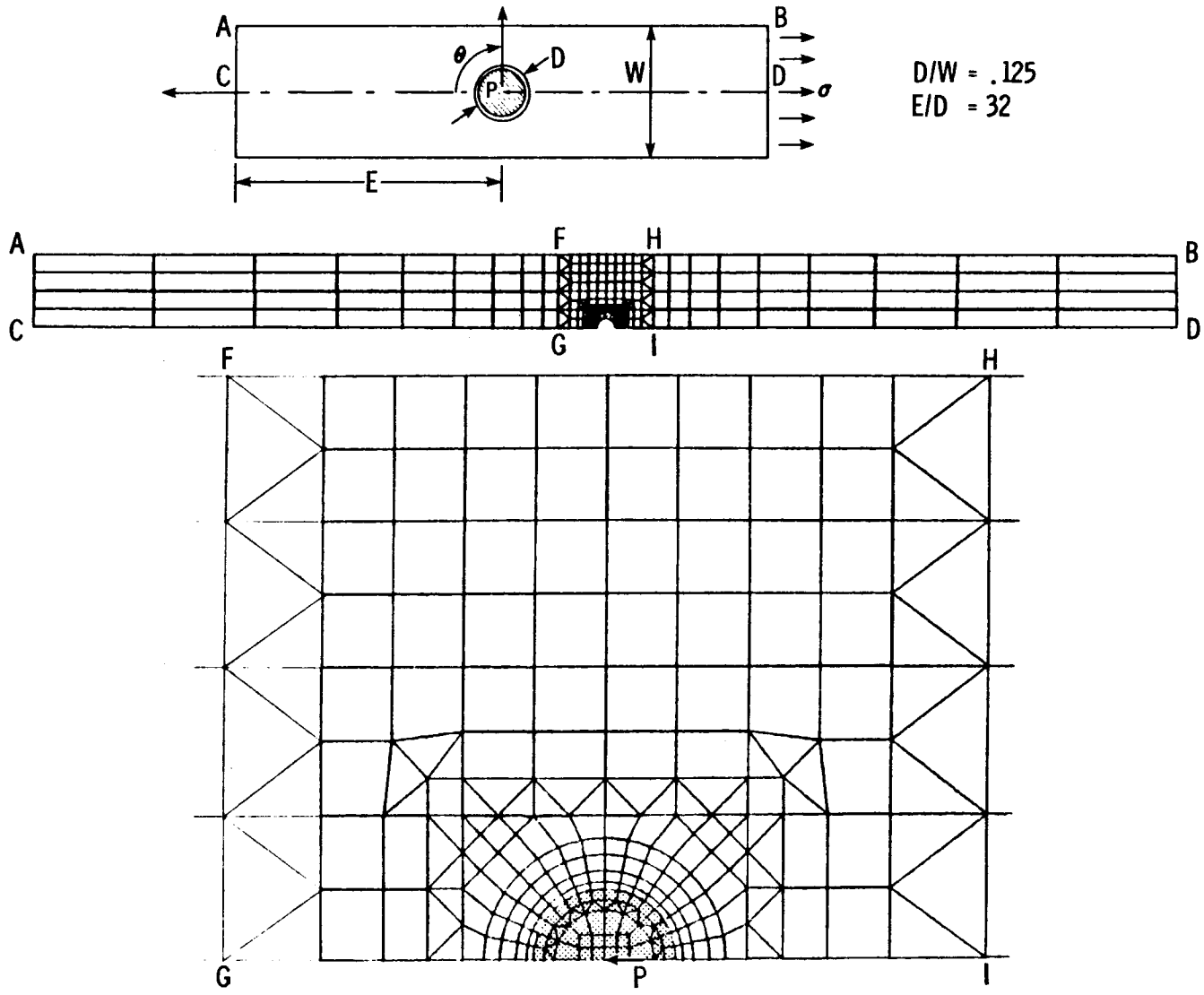

Figure 103. FEM Models For A Loaded Hole, E/D = 32

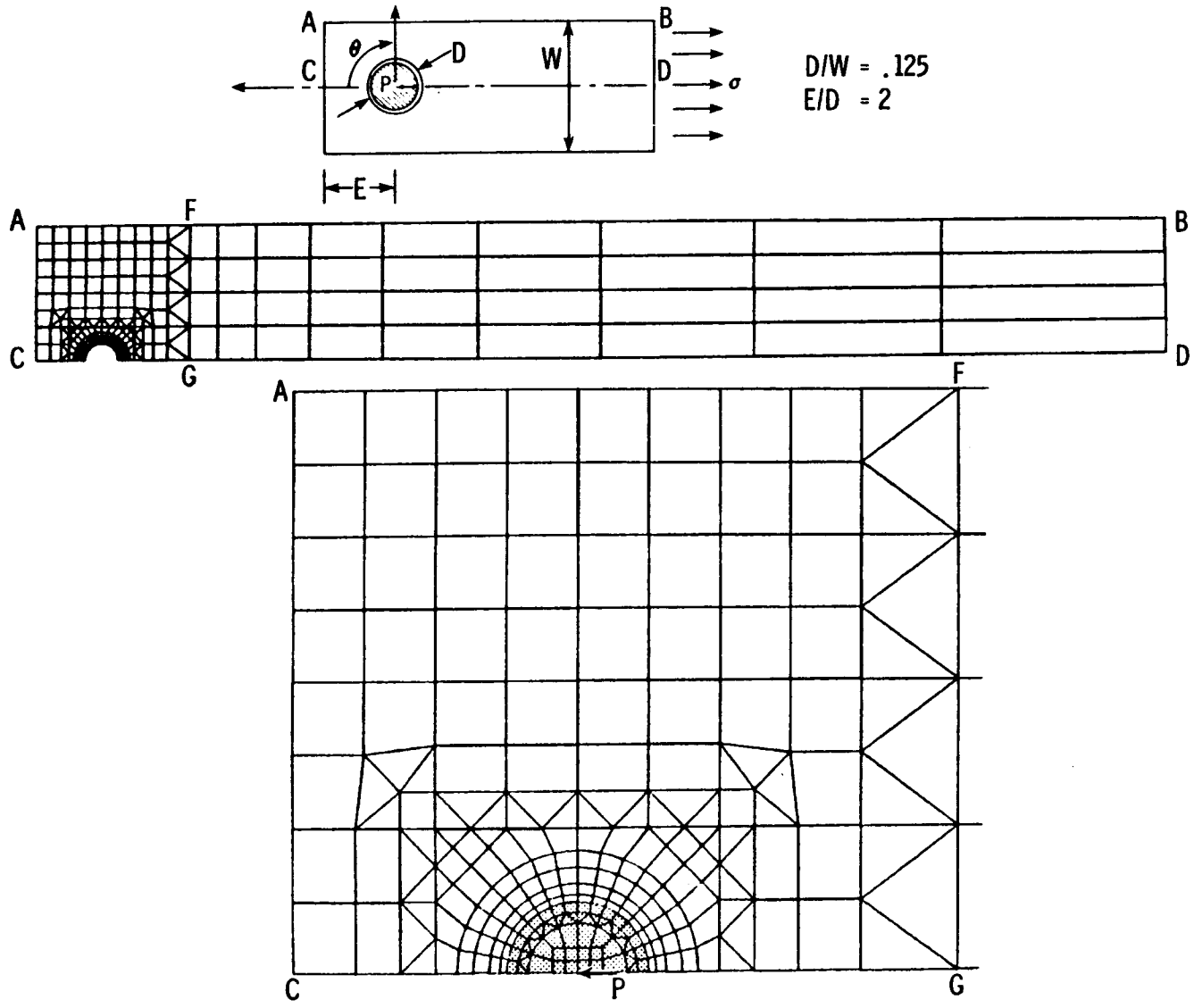

Figure 104. FEM Models For A Loaded Hole, E/D = 2

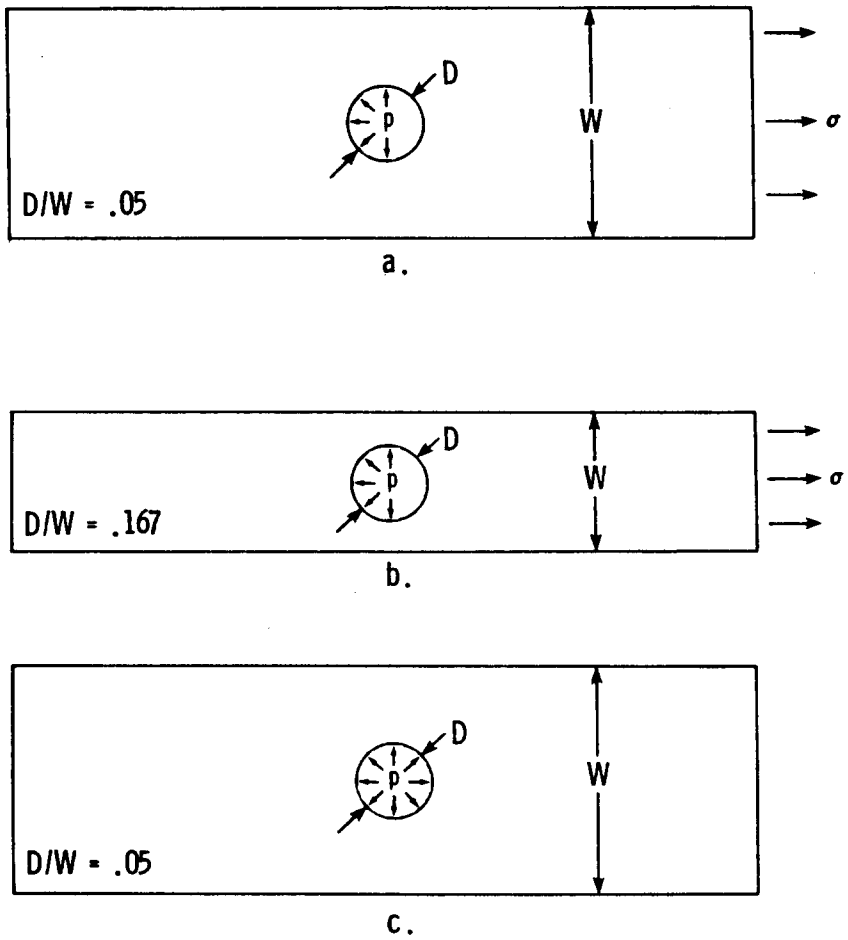

Figure 105. A Hole Subjected To Uniform Internal Pressure

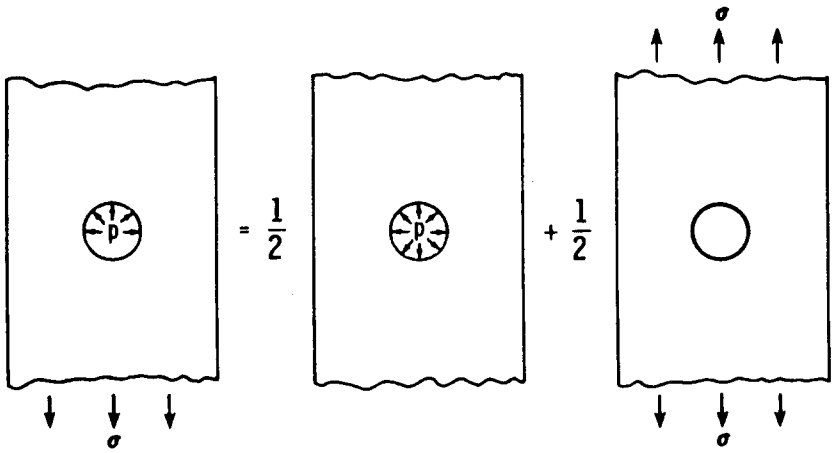

Figure 106. Illustration of Superposition For A Loaded Hole

4.2.2 Two Holes Connected By A Slot

The k_{tb} of two holes connected by a slot, as shown in Figure 107, was solved with the 2-D FEM. The fastener-hole interface was realistically treated as described in Section 4.2.1. Analyses were performed for five models having different 2A/W ratios. For each 2A/W ratio, two models with E/D ratio equal to 32 and 2 were analyzed. The results are shown in Table 17.

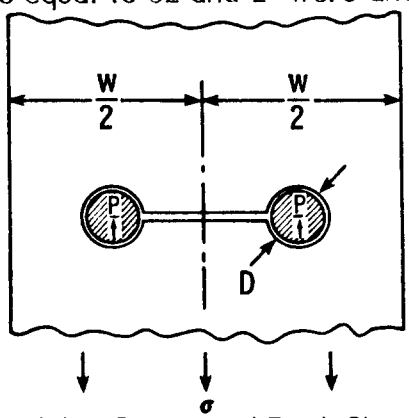

Figure 107. Two-Holes Connected By A Slot-Fastener Load

TABLE 17. FEM RESULTS OF k_{tb} FOR TWO HOLES CONNECTED BY A SLOT

2A/W	E/D	$k_{tb\text{-}max}$	θ_{max} (degree)	$k_{tb\text{-}90^o}$	Compounded Solution	Deviation (%)
0.050	32	1.242	84.375	1.232	1.324	6.6%
	2	3.222	78.75	2.684	-	-
0.125	32	1.3330	90.0	1.330	1.442	8.4%
	2	3.216	78.75	2.701	-	-
0.208	32	1.452	90.0	1.452	1.584	9.1%
	2	3.212	78.75	2.727	-	-
0.417	32	1.856	90.0	1.856	2.075	11.8%
	2	3.219	78.75	2.932	-	-
0.625	32	2.604	90.0	2.604	2.864	10.0%
	2	3.855	84.375	3.615	-	

The k_{tb} obtained with the compounded solution method which is described in Section 4.1.3 is also shown in Table 17. It can be seen that the agreement between the FEM results and the compounded solutions is within an accuracy of about 12%. Table 17 also indicates that the E/D ratio has a great effect on k_{tb}, but that the effect of D/W on k_{tb} is small for E/D = 2.

5.0 DAMGRO COMPUTER PROGRAM

A computer program "DAMGRO" (Damage Growth) has been developed based upon the analytical results described in Sections 2, 3, and 4. The computer program was written in terms of FORTRAN language. Using the DAMGRO, structural life can be predicted with any one of the following three methods, namely, (i) crack growth only, (ii) combined crack growth and initiation, or (iii) crack initiation only. Method (i) - crack growth only and method (ii) - combined crack growth and initiation will be validated later in Task VIII based upon Task IV structural test result. Improvements, if necessary, will then be made. Method (iii) is similar to the old fatigue analysis as adopted in the safe life approach; thus no experimental verification of this method is required in this contract. A user's manual will be developed after the completion of experimental validation of computer program.

The "DAMGRO" computer program contains 10 subroutines to calculate the stress intensity factors and six subroutines to calculate the stress concentration factors. The structural models corresponding to these sixteen subroutines are shown in Figures 108 through 123. The cracks in all of the models can be either a through-thickness crack or a corner crack. The load on each model can be either remote stress only or a combination of remote stress and fastener load.

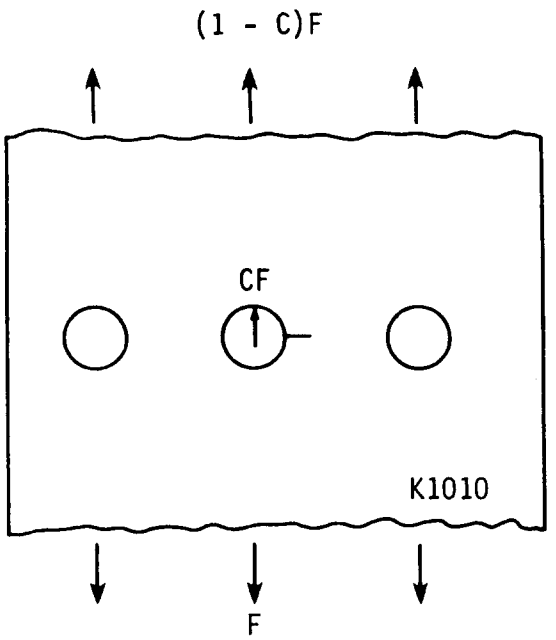

Figure 108. Subroutine K1010

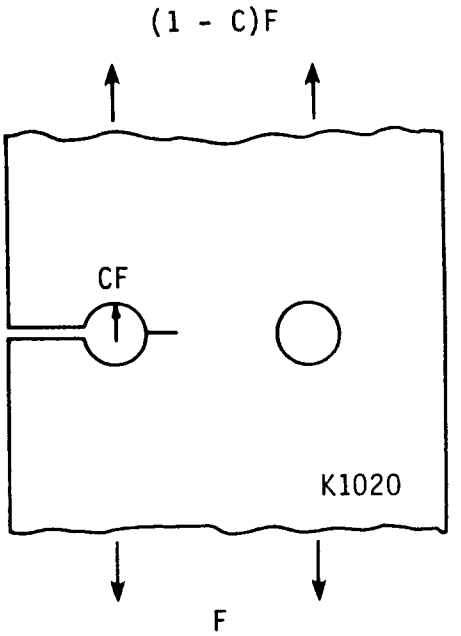

Figure 109. Subroutine K1020

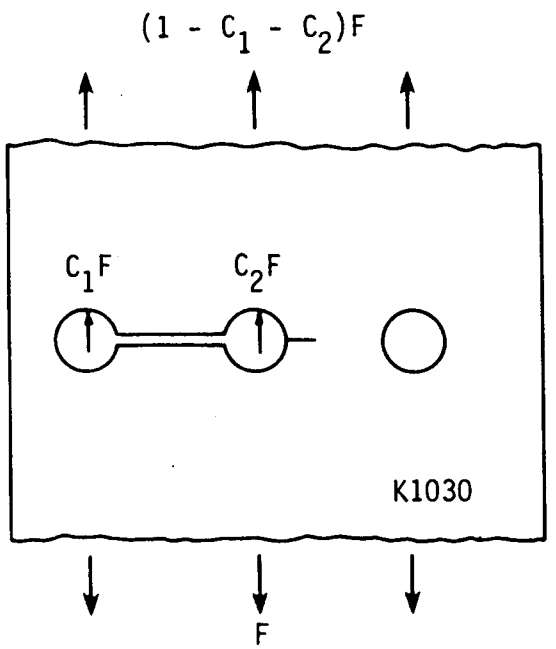

Figure 110. Subroutine K1030

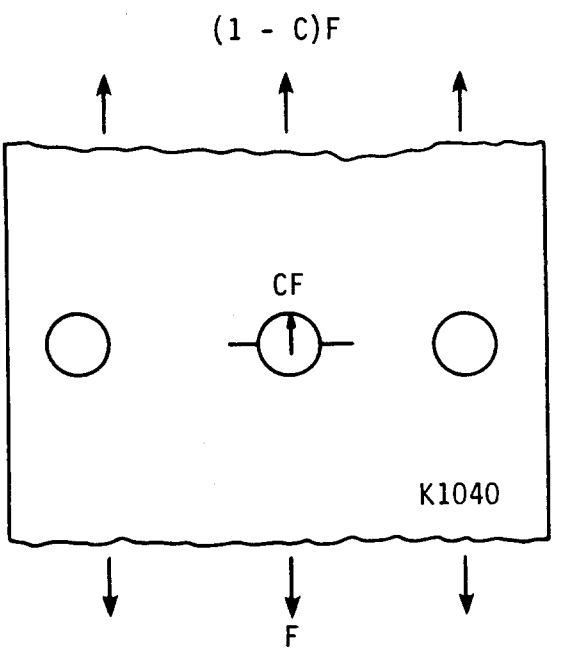

Figure 111. Subroutine K1040

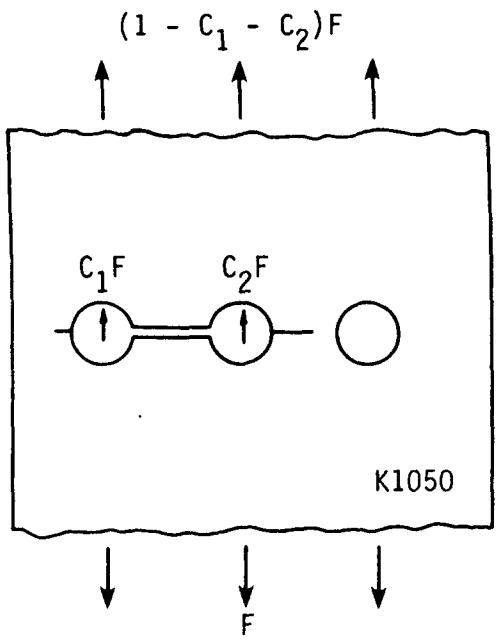

Figure 112. Subroutine K1050

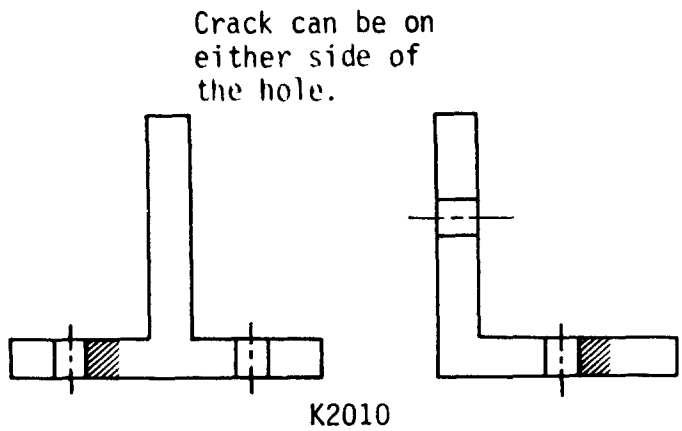

Figure 113. Subroutine K2010

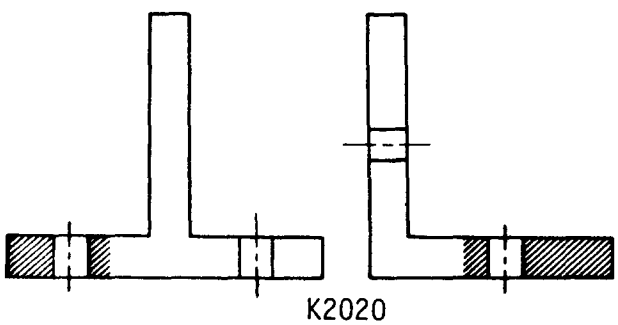

Figure 114. Subroutine K2020

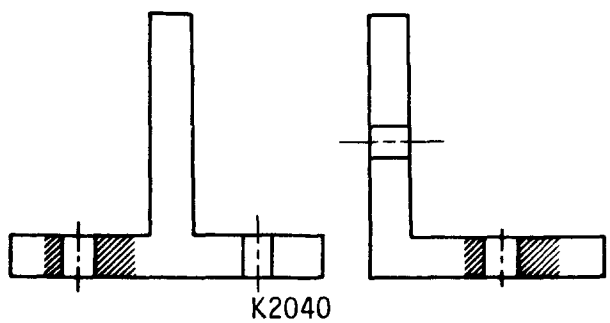

Figure 115. Subroutine K2040

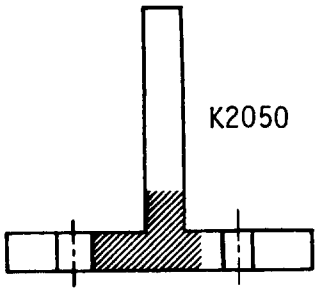

Figure 116. Subroutine K2050

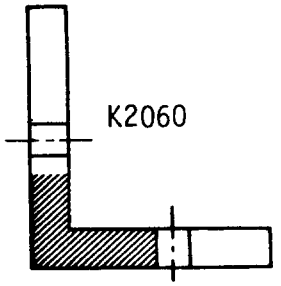

Figure 117. Subroutine K2060

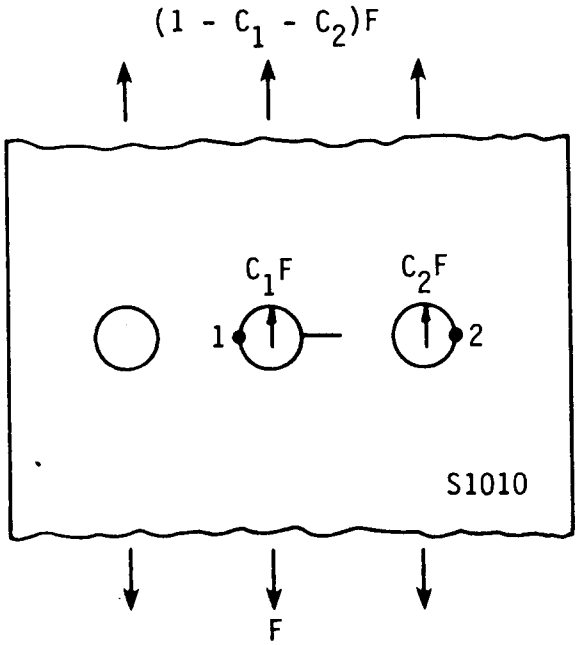

Figure 118. Subroutine S1010

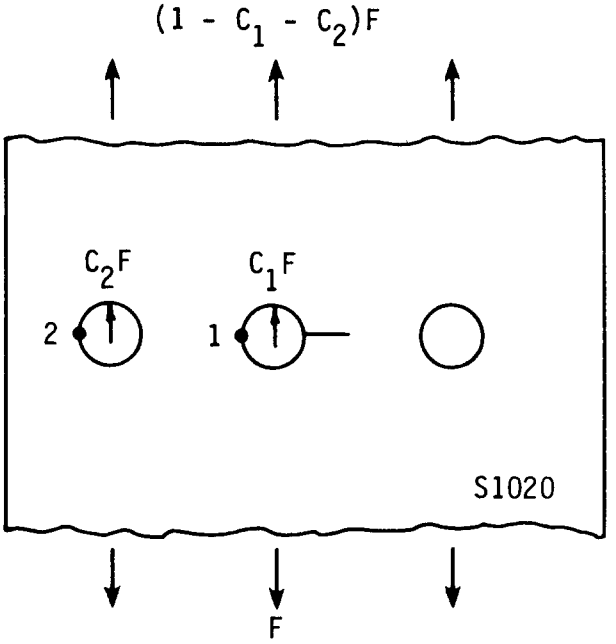

Figure 119. Subroutine S1020

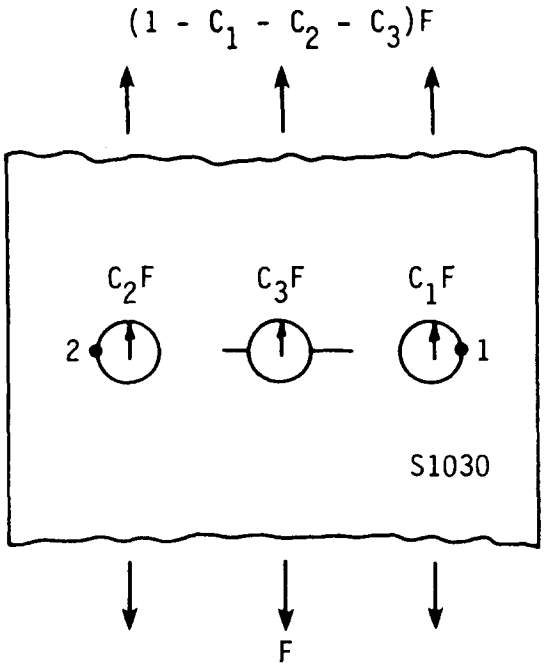

Figure 120. Subroutine S1030

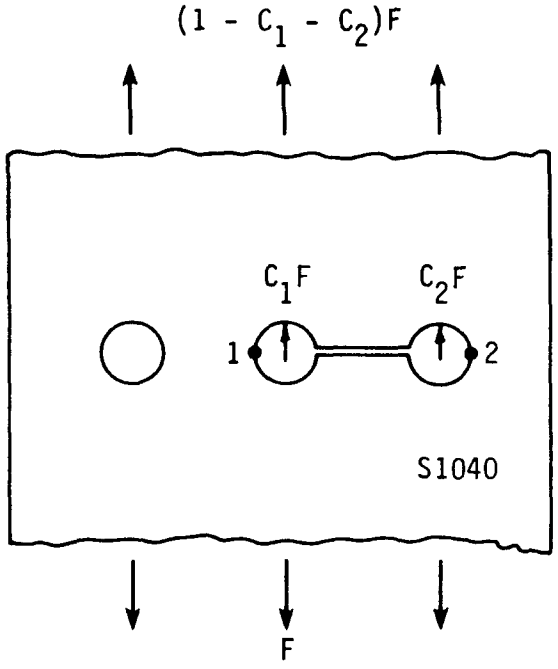

Figure 121. Subroutine S1040

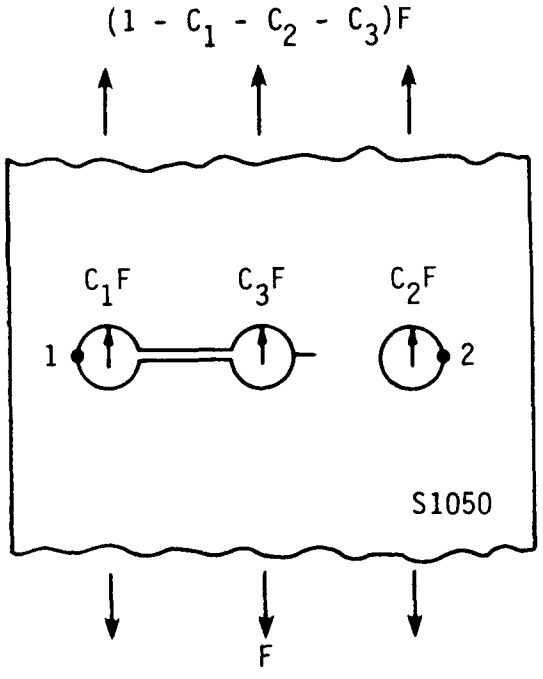

Figure 122. Subroutine S1050

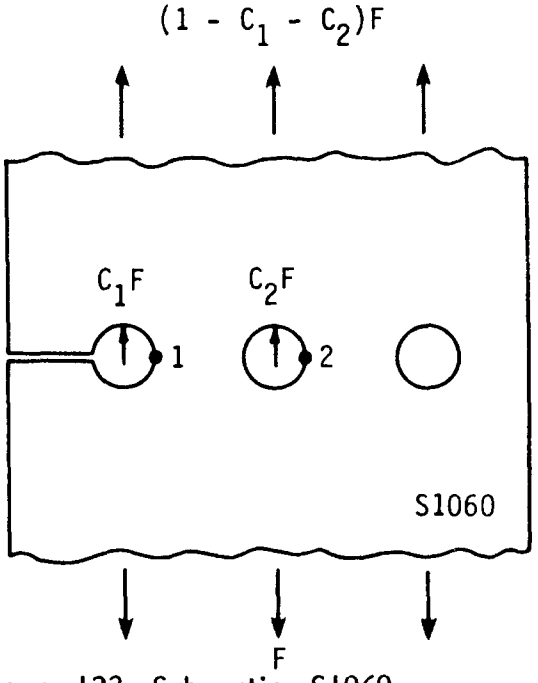

Figure 123. Subroutine S1060

6.0 CONCLUSIONS

1. Two damage tolerance analysis methods have been developed. The first method is based on the growth of one crack only. The second is based on the combination of crack initiation and growth. This latter method also deals with the simultaneous growth of two cracks emanating from the same hole or internal notch.

2. The strain energy density is proposed as the governing parameter for crack initiation analysis. The load interaction, stress ratio, and material size effect are considered in the analysis.

3. The stress intensity factors and stress concentration factors associated with simple configurations representative of airframe structures are integrated, improved, and simplified. Some of the factors are validated with or obtained from the two-dimensional and three-dimensional finite element method.

4. Based on the comparison with the results from the finite element analyses, it has been shown that the compounded solution method can give quite accurate stress intensity factors and stress concentration factors provided, appropriate modeling and accurate ancillary solutions are used.

5. The two-dimensional finite element method is an indispensable tool to analyze fastener load distributions of lap-joints as a function of crack length. The faying surfaces' frictional force can also be included in the analysis.

6. The computer program "DAMGRO" has been developed for structural life prediction. "DAMGRO" has three options to predict structural life: (i) crack growth only, (ii) combined crack growth and initiation, or (iii) crack initiation only.

REFERENCES

1. Anon, "Airplane Damage Tolerance Requirements," MIL-A-83444 (USAF), Aeronautical Systems Division, United States Air Force, July 1974.

2. Cartwright D. J. and Rooke D. P., "Approximate Stress Intensity Factors Compounded from Known Solutions, "Engrg. Fract. Mech., Vol. 6, No. 3, October 1974, pp. 563-571.

3. Brussat, T. R., Chiu, S. T. and Creager, M. "Flaw Growth in Complex Structure - Technical Discussion," AFFDL-TR-77-79, Vol. I, December 1977.

4. Brussat, T. R., Chiu, S. T. and Creager, M., "Flaw Growth in Complex Structure - Test Data," AFFDL-TR-77-79, Vol. II, December 1977.

5. Brussat, T. R., Chiu, S. T. and Creager, M., "Flaw Growth in Complex Structure - Summary, Assessments, Conclusion, "AFFDL-TR-77-79, Vol. III, December 1977.

6. Chang, J.B., Hiyama, R. M. and Szamossi, M., "Improved Methods for Predicting Spectrum Loading Effects, Volume I - Technical Summary," AFWAL-TR-81-3092, November 1981.

7. Willenborg, J., Engle, R. M. and Wood, H. A., "A Crack Growth Retardation Model," AFFDL-TM-71-1-FBR, 1971.

8. Gallagher, J. P., "A Generalized Development of Yield-Zone Models," AFFDL-TM-74-28, 1974.

9. Jarfahl, L. E. "Optimum Design of Joint, The Stress Severity Factor, "Fifth ICAF Symposium; Melbourne, Australia, May 1967, pp. 49-63.

10. Neuber, H. "Theory of Stress Concentration for Shear Strained Prismatical Bodies with Arbitrary Non-Linear Stress-Strain Law," J. Appl. Mech. Dec. 1961, pp. 544-550.

11. Wetzel, R. M., "Smooth Specimen Simulation of Fatigue Behavior of Notches," J. of Materials, JMLSA, Vol. 3, No. 3, Sept. 1968, pp. 646-657.

12. Crews, J. H. Jr. and Hardrath, H. F., "A Study of Cyclic Plastic Stress at a Notch Root," Experimental Mechanics, Vol. 6, No. 6, June, 1966, pp. 313-320.

13. Neuber, H. Theory of Notch Stresses: Principles for Exact Stress Calculation. J. W. Edwards (Ann Arbor, Mich.) 1946: (Kerebspan-nungslehre: Grundlagen fur genaue Spannungsrechung, Julius Springer (Berlin), 1937).

14. Kuhn, P. and Figge, I. E. "Unified Notch-Strength Analysis for Wrought Aluminum Alloys," NASA TN D-1259, May 1962.

15. Kuhn, P. and Hardrath, H. F. "An Engineering Method for Estimating Notch-Size Effect in Fatigue Tests on Steel," NACA TN 2805, 1952.

16. Bowie, O. L., "Analysis of an Infinite Plate Containing Radial Cracks Originating at the Boundaries of an Internal Circular Hole," J. Math. and Phys., Vol. 35, 1956, pp. 60-71.

17. Tweed, J. and Rooke, D. P., "The Distribution of Stress Near the Tip of a Radial Crack at the Edge of a Circular Hole," Int. J. Engrg. Sci., Vol 11, 1974, pp.1185-1195.

18. Tweed, J. and Rooke, D. P. "The Elastic Problem for an Infinite Solid Containing a Circular Hole with a Pair of Radial Cracks of Different Length," Int. J. Engrg. Sci., Vol. 14, 1976, pp. 925-933. Also: Rooke, D. P. and Tweed, J., "Open-mode Stress Intensity Factors for Two Unequal Cracks at a Hole," RAE Technical Report No. 79105, Farnborough, Hants, Great Britain, August 1979.

19. Newman, J. C. Jr. and Raju, I. S. "Stress Intensity Factor Equations for Cracks in Three-Dimensional Finite Bodies,"NASA Technical Memorandum 83200, August, 1981.

20. Tada, H., Paris, P. C. and Irwin, G. R. The Stress Analysis of Cracks Handbook, Del Research Corp., Hellertown, PA., 1973.

21. Schijve, J. "The Stress Intensity Factor of Small Cracks at Notches," Fatigue of Engineering Materials and Structures, Vo. 5, No. 1, 1982, pp. 77-90.

22. Isida, M. "Stress Intensity Factors for the Tension of an Eccentrically Cracked Strip," ASME Trans, J. Appl. Mech., Vol. 33, 1966, pp. 674-675.

23. Isida, M., "On the Determination of Stress Intensity Factors for Some Common Structural Problem," Engrg. Fract. Mech., Vol. 2, 1970, pp. 61-79.

24. Barsoum, R. S., "On the Use of Isoparametric Finite Elements in Linear Fracture Mechanics, "Inter. J. for Num. Meth. in Engrg., Vol. 10, 1976, pp. 25-37.

25. Sanders, J. L., "Effect of A Stringer on the Stress Concentration due to a Crack in a Thin Sheet," NASA Technical Report R-13, 1959.

26. Peery, D. J., Aircraft Structures, McGraw-Hill Book Co., New York, 1950.

27. Barrois, E., "Stresses and Displacements due to Load Transfer by Fasteners in Structural Assemblies," Engrg. Fract. Mech., Vol. 10, pp. 115-176, 1978.

28. Swift, T. and Wang, D. Y., "Damage Tolerant Design - Analysis Methods and Test Verification of Fuselage Structures," in AFFDL-TR-70-144, Proceedings of Air Force Conf. on Fatigue and Fracture of Aircraft Structures and Materials, December, 1969, pp. 653-6783.

29. Yen, S. W. and Smillie, D. G., "Computer Analysis of Fastener Load Distribution in A Multi-row Joint", Computer and Structures, Vol. 3, 1973, pp. 1293-1320, 1973.

30. Shah, R. C., "Stress Intensity Factors for Through and Part-through Cracks Originating at Fastener Holes," in ASTM STP 590, 1976, pp. 429-459.

U.S. GPO: 646-066